



**UNIVERSITÀ
DEGLI STUDI
DI PADOVA**

UNIVERSITÀ DEGLI STUDI DI PADOVA
Dipartimento di Ingegneria Industriale DII
Corso di Laurea Magistrale in Energy Engineering

Optimizing wind energy generation with dimpled wind turbine blades

Relatore:
Prof. Giorgio Pavesi

Studente:
Matteo Vendramini
n. 2052439

Anno Accademico 2022-23

*"A volte sono le persone che nessuno immagina
che possano fare certe cose, quelle che fanno cose
che nessuno può immaginare"*

The Imitation Game

Acknowledgments

I wish to express my sincerest gratitude to all the people who contributed to the completion of this thesis. First and foremost, I would like to thank my supervisor, Prof. Giorgio Pavesi, for his invaluable guidance and constant support throughout the writing of this work. Thanks to his valuable insights, I was able to develop a thesis that I am truly proud of.

A heartfelt thank you also goes to my family, my parents, and my sister. Thank you for being by my side at every moment, for believing in me, and for giving me the strength to overcome the challenges I encountered along the way.

A special thanks goes to my friends studying aerospace engineering. Your expertise and assistance during the thesis were truly invaluable. You were always available to help and share valuable ideas, and I am grateful for that. A special thought goes to my friends in energy engineering, as we share this degree in a special way. Thank you for all the laughs and the great moments we shared together during these years, thank you for sharing hours in the library studying, thank you for the coffee breaks together, for the aperitifs (both alcoholic and non). Your support and comfort made the days of studying much lighter. Thanks also to my mechanical engineering friends, study companions, but especially for study breaks outside Bernardi. A warm thanks to all the members of UniZEB, a project I became passionate about from the beginning and which gave me the opportunity to meet fantastic people. A heartfelt thank you also goes to my friends with whom I share a passion for the mountains. Our excursions were a precious outlet after the most intense study periods. I couldn't forget my roommates, who tolerated me with great patience and understanding, especially during the days of highest stress. You were the best family I could find.

Lastly, a special thank you goes to Tommaso Carmagnani and Francesco Albicini. Thank you for all the unforgettable moments we shared together, both within the university and, above all, outside of it. Your friendship has been a constant source of support.

To all these people, my heartfelt thanks. Without you, this thesis wouldn't have been the same. Your presence in my life made this journey unique.

Contents

List of Figures	vii
Symbols and acronyms	xi
Abstract	xiii
Riassunto	xv
Introduction	xvii
Theory and Literature review	1
Methodology	9
1 Boundary Layer	11
1.1 Prandtl's boundary layer concept	12
1.2 Boundary layer equations	12
1.3 Effects of Reynolds number on the performances	14
2 Aerodynamic devices	15
2.1 Aerodynamic devices	15
2.1.1 Triangular vortex generators	15
2.2 Three-dimensional rotational effect	17
2.3 Dimples	18
2.3.1 Circular dimples	18
3 Site analysis	21
3.1 Windiness	21
3.1.1 Weibull statistical distribution	22
3.1.2 Rayleigh distribution	24
3.1.3 Study case	24
3.1.4 Roughness	25

3.2	Velocities	27
4	Energy	29
4.1	Energy produced	29
4.1.1	Capacity factor	30
5	Turbulence model	31
5.1	Direct Normal Simulations - <i>DNS</i>	31
5.2	Large Eddy Simulations - <i>LES</i>	32
5.3	Reynolds Averaged Navier-Stokes - <i>RANS</i>	32
5.3.1	One-Equation Models	34
5.3.2	Two-Equations Models	35
5.3.2.1	$k - \epsilon$ models	36
5.3.2.2	$k - \omega$ models	37
5.3.2.3	$k - \omega$ <i>SST</i> model	37
5.4	Hybrid RANS-LES models	39
5.4.1	Detached Eddy Simulations - <i>DES</i>	39
5.5	Comparison between models	40
5.6	Turbulence models chosen	41
6	Baseline profile	43
6.1	Wing profile choice considerations	44
6.1.1	Airfoil profiles for small power WTs	46
7	Blade model	47
7.1	Design	47
7.1.1	MATLAB Software	47
7.1.2	Baseline blade	48
7.1.2.1	Tip losses	50
7.1.2.2	Wing profile	50
7.1.3	MATLAB software results	51
7.1.4	3D model	52
7.1.5	SolidEdge models	53
7.1.5.1	Blade	53
7.1.5.2	Hub	54
7.1.6	Control volume models	55
7.1.7	CFX setup	58

8	Dimpled section	61
8.1	Section	61
8.2	Dimple choice	61
8.2.1	Prior investigations	61
8.2.2	Present study	64
8.3	Ansys mesh	66
8.4	CFX setup	70
9	Results of simulations	73
9.1	Dimpled sections	73
9.2	Considerations	76
9.3	Spanwise	80
10	Dimpled blade model	81
10.1	Design	81
10.1.1	Small volume domain	82
10.1.2	Control volume mesh	82
10.2	CFX setup	83
	Results	85
	Conclusions	97
	Bibliography	101

List of Figures

1	Wind turbine components [29]	2
2	HAWTs and VAWTs	3
3	Passive stall power control	4
1.1	Boundary layer thickness [33]	11
1.2	Laminar and turbulent boundary layer [8]	11
1.3	Velocity profile along airfoil [33]	13
2.1	Triangular vortex generators, CoR (a) and CtR (b) [16]	16
2.2	Diagram of physical mechanism of VGs [19]	18
2.3	Comparison among CtR, CoR and dimples [37]	19
2.4	Inward and outward dimples [26]	20
3.1	Weibull probability density	23
3.2	$\ln(-\ln(1 - F(v)))$ vs $\ln v$	25
3.3	Wind speed profile as function of height	26
3.4	Cut-in and cut-out velocities effect on energy produced	27
3.5	Power profiles for different nominal velocities	28
5.1	Turbulence models in CFD, from DNS to RANS [18]	31
5.2	Size of Eddies	35
5.3	Energy density of the eddies. On the $x - axis$, there is the size of eddies decreasing from left to right	36
5.4	Turbulence models example: DNS, LES, RANS [24]	40
5.5	Energy distribution and scales in turbulence modeling [3]	41
6.1	Low lift and high lift profiles [2]	44
6.2	Forces acting on the airfoil [20]	44
7.1	Alxion 190STK3M electric generator [4]	49
7.2	Span variation of the tip loss factor	50

7.3	S1210 airfoil profile [2]	52
7.4	Characteristic parameters ¹ of S1210 profile [2]	52
7.5	Reference blade model	53
7.6	3D SolidEdge model	54
7.7	Hub	55
7.8	Control volume meshes	56
7.9	Control volumes	57
7.10	Pocket inside the big volume	57
7.11	CFX-setup	59
8.1	Dimples geometric configuration [11]	62
8.2	(a) Two-dimensional view of a dimpled blade; (b) Sketch of dimpled airfoil (cross-section A-A) [31]	63
8.3	Dimple specification sections obtained with Autodesk Inventor	65
8.3	Dimple specification sections obtained with Autodesk Inventor (continued)	66
8.4	Control volume dimensions	66
8.5	Mesh details	67
8.5	Mesh details (continued)	68
8.6	Prism layers [1]	69
8.7	Unstructured mesh and prism layers [1]	69
9.1	Lift coefficient vs AoA	75
9.2	Drag coefficient vs AoA	75
9.3	Lift/Drag coefficient vs AoA	76
9.4	Turbulence kinetic energy plots	77
9.5	Flow streamlines	78
9.6	y^+ plot	79
9.7	Vector plot of velocity near the wall	79
10.1	Small volume domain with dimpled blade	82
10.2	Control volume meshes	83
10.3	Power generated vs wind speed	86
10.4	Power generated vs λ	86
10.5	Power coefficient vs wind speed	87
10.6	Power coefficient vs λ	87
10.7	Power generated vs wind speed	89
10.8	Power generated vs λ	89
10.9	Power coefficient vs wind speed	90
10.10	Power coefficient vs λ	90

10.11 Power comparison vs wind speed	92
10.12 Power coefficient comparison vs wind speed	92
10.13 HAWT 3D model	95
10.14 Technical drawing of the 3D model of HAWT	96

Symbols and acronyms

λ - Tip speed ratio

μ_t - Eddy viscosity

C_D - Drag coefficient

C_F - Capacity factor

C_L - Lift coefficient

$C_{L,max}$ - Maximum lift coefficient

C_M - Pitching moment coefficient

C_T - Torque coefficient

C_p - Power coefficient

D_{hub} - Hub diameter

D_{tip} - Tip diameter

c_d - Drag coefficient

$c_{d,p}$ - Drag coefficient due to pressure field

$c_{d,v}$ - Drag coefficient due to viscous stresses

l_m - Mixing length

y^+ - Yplus

y_H - Height of first layer

AoA - Angle of attack

BL - Boundary layer

CFL - Courant number

CoR - Co-rotating orientation

CtR - Counter-rotating orientation

D - Diameter of the dimple

- DES** - Detached Eddy Simulation
- DNS** - Direct Normal Simulation
- G** - Geometric growth ratio
- HAWT** - Horizontal axis wind turbine
- IEA** - International Energy Agency
- IEC** - International Electrotechnical Commission
- LES** - Large Eddy Simulation
- LSB** - Laminar separation bubble
- LV** - Large volume
- N** - Number of layers
- NACA** - National Advisory Committee for Aeronautics
- NASA** - National Aeronautics and Space Administration
- RANS** - Reynolds Averaged Navier-Stokes
- Re** - Reynolds number
- SST** - Shear Stress Transport
- SV** - Small volume
- TDRE** - Three-dimensional rotational effect
- TSR** - Tip speed ratio
- VAWT** - Vertical axis wind turbine
- VG** - Vortex generator
- WT** - Wind turbine
- c** - Chord length of the airfoil
- d** - Length scale

Abstract

In this study the effect of dimpled surface blade on the performance of an horizontal axis wind turbine, HAWT, is numerically investigated.

The goal is to compare the energy produced along the year with a dimpled surface on the suction side of the turbine and the smooth airfoil. The suction side of the wind turbine has been modified using spherical dimples. The governing continuity and momentum equations are solved using hybrid RANS-LES solution, DES turbulence model in particular, to evaluate the best dimple geometry, coupled with an Unsteady RANS model - *Shear Stress Transport* - $\gamma_{\theta,Re,t}$ - for the evaluation of power produced by the HAWT.

Different kind of dimples have been tested, varying the diameter and location along the chord of the blade. The findings indicate that the optimal position occurs when the dimples are located at 30% of the chord length, spanning radially between 15% and 45%.

The conducted simulations provide evidence that incorporating the dimpled design, in comparison to the nominal profile, results in a 4.36% increase in the energy generated. This translates to a rise from 2811 *kWh/y* to 2939 *kWh/y*, consequently elevating the capacity factor from 21.39% to 22.37%.

Riassunto

L'obiettivo di questo studio è migliorare l'efficienza e la produzione energetica delle turbine eoliche domestiche, valutando il problema della separazione dello strato limite. Metodi precedenti, come generatori di vortici triangolari o turbolatori, hanno mostrato limitazioni a causa dell'effetto rotazionale tridimensionale indotto dalla turbina stessa. Pertanto, in questo studio è stata proposta l'implementazione di fossette assial simmetriche per affrontare questa problematica.

Poiché ogni turbina eolica ha una configurazione unica e attributi variabili come la forma del profilo alare, la velocità di rotazione e i diametri del mozzo e della punta, non esiste una configurazione universale per le fossette. Pertanto, è necessario condurre un'analisi specifica per ogni caso di studio individuale.

La scelta del sito di installazione è fondamentale in quanto influisce direttamente sul profilo di base della pala. Successivamente, la geometria delle fossette viene ottimizzata esplorando diverse configurazioni e testandole attraverso simulazioni CFD.

Una volta individuata la migliore geometria, è stata creata la geometria della pala modificata utilizzando un software CAD. Successivamente, le due configurazioni, quella di base e quella con fossette, sono state confrontate in termini di potenza e produzione energetica.

I risultati hanno evidenziato che la posizione ottimale per le fossette si trova al 30% della lunghezza della corda, con un posizionamento radiale tra il 15% e il 45% del raggio totale della pala. L'adozione delle fossette sulla superficie della pala ha portato a un aumento dell'energia generata del 4,36%, corrispondente a un incremento da 2811 *kWh/anno* a 2939 *kWh/anno*. Inoltre, il fattore di capacità è aumentato dal 21,39% al 22,37%.

Introduction

Renewable energy plant installations have experienced continuous growth in recent decades, and wind energy has played a crucial role in this trend. Innovative construction techniques have enabled wind turbines to increase in size, leading to optimized electricity production. In the late 1990s, wind turbine diameters began to grow larger to harness more kinetic energy from the wind. However, these plants may not meet the requirements of isolated users who are not connected to the electricity grid, necessitating the development of small wind turbines.

Small wind turbines are used for small-scale electricity production, typically generating between $500\text{ W} - 10\text{ kW}$. They are smaller than wind turbines located in wind farms, with diameters ranging from 1 m to 4 m . While extensive research has been conducted on their location, windiness, placement, and materials, the aerodynamic design of wind blades remains an open issue due to their diverse application domains.

Small wind turbines often have passive yaw systems and are not equipped with variable speed generators to contain costs. Since the rotation speed is constant, a possible method to control the power produced is through the variable pitch system, where the blade is rotated on its longitudinal axis to reduce the angle of attack when wind intensity increases. The basic control system called Danish control is used to limit power and it's based on the detach of the boundary layer when wind intensity increases.

For low power production wind turbines, no control system is usually used to limit costs, even if the system's efficiency is not the best. Boundary layer separation leads to stall conditions, which create many aerodynamic forces on the blade that can lead to non stationary forces on the blade, in particular huge thrust forces that create a significant bending moment on the blade. This aspect highlights the importance of controlling the separation of the boundary layer to control stall, the lift generated by the airfoil, and the angle of attack.

Various strategies are employed to achieve this goal, such as implementing grooves on blades, considering slots on the leading edge of blades, installing trailing edge flaps, or incorporating riblets or vortex generators on the blades' surface.

Theory and Literature Review

Theory

History of Wind Energy The utilization of wind energy has a vast and enduring history that spans thousands of years. Throughout ancient civilizations such as Babylonian and Egyptian societies, humans began harnessing the power of wind to fulfill their energy requirements. Sails and windmills were employed during these times for activities like water pumping and grain grinding, which played a vital role in supporting agricultural communities.

During the Middle Ages, wind energy continued to be extensively utilized in Europe. Windmills became a common sight in rural areas and were used for various purposes, including milling grains, producing oil, and processing textiles. These vertical windmills, known as "tower mills," featured wooden or cloth blades and represented an early form of industrial application for wind energy.

As the industrial era emerged in the 19th century, wind energy experienced significant transformations. The introduction of metal blades revolutionized windmill technology, enhancing efficiency and durability. Windmills were then employed to power industrial machinery like sawmills, foundries, and paper mills. Wind energy played a crucial role in the process of industrialization during this period.

In the 20th century, the focus shifted towards using wind energy for electricity generation. In 1888, Charles F. Brush, a Scottish inventor, constructed the first wind turbine for producing electricity in Cleveland, United States. However, it was not until the 1970s, driven by the 1973 oil crisis and growing environmental awareness, that wind energy began to gain momentum as an alternative to conventional energy sources.

In the 21st century, wind energy has witnessed remarkable global growth. Advancements in turbine technology, increased efficiency, and cost reductions have made wind energy a competitive source of power. Countries like China, the United States, Germany, and India have made substantial investments in wind energy, establishing large-scale onshore and offshore wind farms.

Wind energy is derived from the kinetic energy of moving air masses, commonly referred to as wind. The wind is generated by the uneven heating of the Earth's surface by the sun, causing air to move from areas of high pressure to areas of low pressure. To convert wind energy into electricity, the kinetic energy of the wind is captured using wind turbines and transformed into mechanical power, which is then converted into electrical power.

Components of a Wind Turbine A wind turbine is the primary device employed to capture and convert wind energy into electricity. It consists of several essential components, including the tower, rotor, nacelle, and blades (Fig. 1). The tower provides structural support and elevates the turbine to an optimal height for capturing stronger winds. The rotor, comprising the hub and blades, captures the wind and converts its kinetic energy into rotational motion. The nacelle houses the key components of the turbine, such as the gearbox, generator, and control systems.

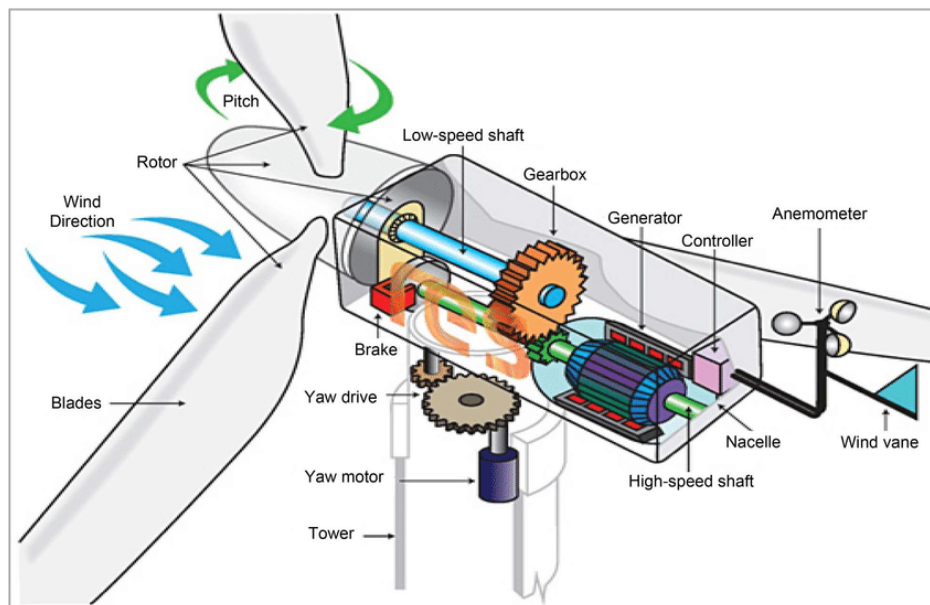
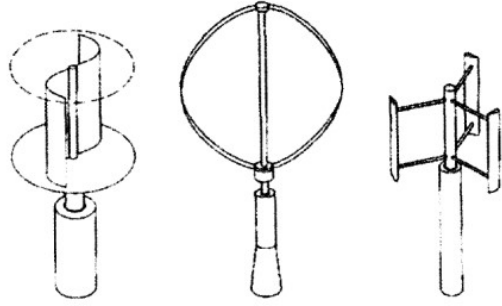


Figure 1: Wind turbine components [29]

There are two main types of wind turbines: horizontal-axis wind turbines (HAWTs, Fig. 2a) and vertical-axis wind turbines (VAWTs, Fig. 2b). HAWTs have their rotor shaft and blades aligned horizontally, making them the most common type of wind turbine. They are efficient at higher wind speeds and are primarily used in large-scale onshore and offshore wind farms. VAWTs, on the other hand, have their rotor shaft and blades arranged vertically, offering the advantage of capturing wind from any direction.



(a) HAWT [27]



(b) VAWTs [17]

Figure 2: HAWTs and VAWTs

Wind turbines can be installed either on land (onshore) or in bodies of water such as lakes or oceans (offshore). Onshore wind farms are more prevalent and typically consist of clusters of wind turbines erected in areas with favorable wind conditions. Offshore wind farms, although more challenging to construct and maintain, benefit from stronger and more consistent winds, resulting in higher energy production potential. Offshore wind energy has garnered significant attention and investment in recent years due to technological advancements and decreasing costs.

To ensure safe and efficient operation, the power output of a wind turbine needs to be controlled. Various power control methods are employed to regulate the turbine's rotational speed and power generation. Pitch control, which adjusts the angle of the blades, is commonly used to control power output by modifying the aerodynamic forces acting on the rotor. Variable speed control allows the turbine to adjust its rotational speed to optimize energy capture under different wind conditions. Additionally, power electronics and control systems monitor and regulate the turbine's performance, ensuring stable and reliable operation. These power control methods are typically employed in high-power wind turbines, while they are less common in small-scale applications due to cost considerations. Large-scale installations can amortize the costs of the control system more easily as they produce higher energy, resulting in a shorter payback period for the investment.

Active pitch control systems adjust the pitch angle of the blades to control the aerodynamic forces acting on the rotor. By varying the angle of attack, the active pitch control system can optimize power production and maintain the turbine within safe operating limits. Sensors and control algorithms continuously monitor wind conditions and adjust the blade pitch accordingly.

Passive stall control systems rely on the aerodynamic properties of the turbine blades to regulate power output. When the wind speed exceeds a certain threshold,

the blades automatically stall, reducing their lift and power production. This passive mechanism allows the turbine to self-regulate its power output without the need for complex active control systems.

Understanding passive stall control requires grasping the concepts of aerodynamic stall and angle of attack. Aerodynamic stall occurs when the angle of attack exceeds a critical value, causing the airflow over the blade to separate and reducing lift. This stall phenomenon is characterized by turbulence, increased drag, and decreased power generation. The angle of attack refers to the angle between the chord line of the blade and the oncoming wind. By adjusting the angle of attack, the aerodynamic forces acting on the blade can be controlled, influencing power production.

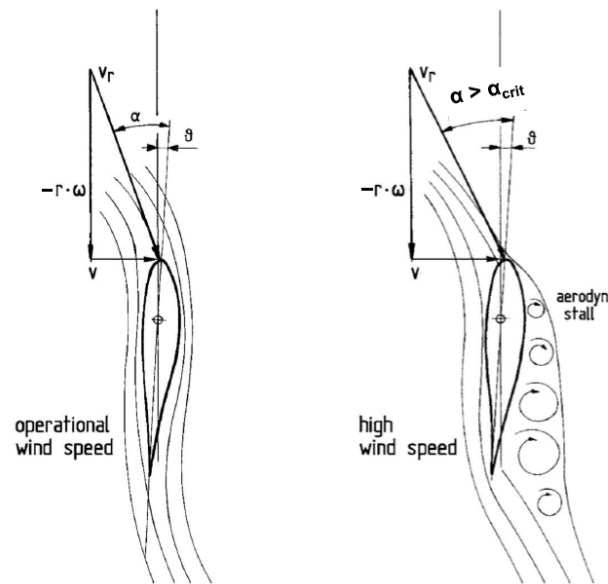


Figure 3: Passive stall power control

Passive stall control offers several advantages in wind turbine operation. Firstly, it is a simpler and more cost-effective method compared to active pitch control since it does not require complex pitch adjustment mechanisms. Secondly, passive stall control allows for better self-regulation of power output in varying wind conditions, resulting in improved efficiency and reliability. Additionally, the absence of active control components reduces maintenance requirements and potential points of failure.

However, passive stall control also has considerations and limitations. The turbine's performance relies on its aerodynamic design and the specific stall characteristics of the blades. Fine-tuning of the blade shape and angle of attack is necessary to ensure optimal performance across a range of wind speeds. Additionally, passive stall control may result in a slight reduction in overall energy capture compared to active pitch control systems in certain wind conditions.

Literature Review

The performance of the wind turbine is strongly influenced by the design of the blades. Specifically, passively stalled wind turbines require careful blade design to maximize efficiency. To increase the efficiency of passively stalled wind turbines, numerous methods have been studied and tested. In particular, the use of vortex generators and small surface dimples has shown to energize the boundary layer, inducing turbulence, and thus delaying stall.

Taking a look at the book "Gli impianti motori eolici" edited by Battisti L. [6], the primary factor that leads to a delay of the boundary layer can be attributed to its associated energy. When the energy contained within the boundary layer is sufficiently high to generate a turbulent boundary layer, it becomes more capable of handling adverse pressure gradients, which are typical for airfoils.

After conducting some research on the web, a few methods of increasing energy within the boundary layer have been discovered. Specifically, certain aerodynamic devices such as VGs (vortex generators), Gurney flaps, and dimples have been observed to enhance the energy contained in the boundary layer by inducing a swirling motion in the fluid. The book [6] provides an initial approach by mentioning that aerodynamic devices are usually installed in the section near the root of the blade.

Subsequently, various methods have been analyzed to gain a better understanding of the advantages and disadvantages associated with each solution.

It became immediately apparent that Gurney flaps do not have a significant impact on delaying the stall of the airfoil. Instead, their primary function is to enhance lift force, albeit with a minor increase in drag.

Regarding vortex generators (VGs), a comprehensive review conducted by Zhao et al. titled "Researches on vortex generators applied to wind turbines: A review" [40], analyzed the behavior of VGs when applied to wind turbines. The researchers conducted simulations using traditional triangular-shaped VGs and discovered that optimizing geometric parameters such as profile, height, position, VG array configuration, and row layout can greatly enhance the performance of airfoils and wind turbines.

In general, micro VGs outperform conventional large-size devices, and the recommended position is typically 20%-30% of the chord length. Furthermore, CtR VGs exhibit superior performance in terms of boundary layer suppression compared to CoR VGs. Additionally, numerous studies have investigated the effectiveness of VGs in controlling separated flow on airfoils. Research has demonstrated that VGs can effectively delay the stall angle, increase $C_{L,max}$ (maximum lift coefficient), and improve the lift-

to-drag ratio L/D .

However, a study conducted by Zhu et al. [19] highlighted issues related to rotational effects resulting from the use of vortex generators. Specifically, the introduction of vortex generators can lead to increased rotational forces on the blades, which may adversely affect the overall performance of the wind turbine. Therefore, careful consideration of rotational effects is necessary when employing vortex generators in blade design. This problem has been highlighted in the research conducted by Zhao et al. [40]. In these researches, the researchers emphasizing how the TDRE is more important in the section close to the root of the blade; this is due to the fact that the radius of curvature is lower compared to the section close to the tip of the blade and this means that the fluid streams are more bended rather than in the section close to the tip;

To tackle this challenge, numerous studies propose the use of an axially asymmetric structure to mitigate undesired rotational effects. By incorporating a blade design that minimizes rotational forces, an axially asymmetric structure enables improved overall system efficiency.

In a simulation conducted by D'Alessandro V. et al. [11], the impact of dimples on the reduction of the laminar separation bubble (LSB) extension and boundary layer development was investigated. The study demonstrated that the application of dimples results in a reduction of the LSB extension when placed before or inside the LSB region.

Conversely, if the dimples are positioned after the bubble, they affect the development of the reattached turbulent boundary layer. In all the cases examined, a decrease in the pressure drag coefficient ($c_{d,p}$) was observed, leading to an increase in the viscous drag coefficient ($c_{d,v}$). This observation was justified through a boundary layer analysis.

However, the primary effect of reducing the pressure drag prevails over the secondary effect of the increased viscous drag, resulting in an overall increase in the drag coefficient (c_d) for two out of the three cases considered in the study. Conversely, the lift coefficient exhibits contrasting behavior due to the dimpling technique. Therefore, the application of dimples on the airfoil investigated in this study can be considered critical, as its effect strongly depends on the angle of attack.

Sedighi et al. [31] carried out a simulation on 2020, which has been published in *Energy* journal; in this research, *Aerodynamic performance enhancement of horizontal axis wind turbines by dimples on blades: Numerical investigation* the effect of dimpled surface blade on the performance of V47-660 kW horizontal axis wind turbine has been numerically investigated, in particular the effect of radius, location, and quantity of

dimples on the aerodynamic performance of the wind turbine including torque and power generation, flow separation, and thrust load have been studied to find an appropriate case. Then the effect of blade pitch angle and wind speed is also examined on the best-dimpled blades. The results show that dimples could be effective in increasing the torque and power generation if they are designed appropriately. Obtained results reveal that for the best situation, dimples could improve the generating torque by around 16.08%.

A similar study was conducted by Saravanan R. [21] on a symmetrical airfoil, specifically the NACA 0018. The research findings revealed significant variations in the drag coefficient of the dimpled wing, attributable to different dimple geometries.

The results indicated that increasing the dimple depth ratio or surface roughness on the dimpled wing can shift the transition to a lower Reynolds number and reduce the drag coefficient in the transcritical regime. Additionally, a positive linear correlation was established between relative roughness and drag coefficient. The implementation of dimples on the NACA 0018 airfoil demonstrated greater effectiveness in modifying various aspects of the flow structure, leading to varied lift and drag forces.

When the flow encounters a dimple on the airfoil's surface, a small separation bubble forms within the cavities. This bubble formation results in accelerated flow between the dimples, causing a transition in the boundary layer from laminar to turbulent. This transition delays the separation of flow from the airfoil, resulting in a substantial reduction in drag force.

A comparative analysis between airfoils with and without dimples, while maintaining a constant inlet velocity (i.e., constant Reynolds number), shows that the coefficient of drag is significantly lower for the dimpled airfoil. This reduction in drag is attributed to the generation of separation bubbles inside the inward dimples and the delay of flow separation through the instability of the shear layer. By introducing dimples, turbulence is created to prolong the occurrence of flow separation, thereby increasing the stall angle.

The main issue related to this research is the fact that a symmetrical airfoil has been used; in fact in domestic application wind turbines, high lift coefficient profiles are usually used (see Chap. 6).

The latest study evaluated was conducted by Mukundan A. [25], focusing on the changes in the aerodynamic characteristics of an airfoil through the application of surface modifications in the form of dimples. The study involved a comparative analysis of modified airfoil models, which exhibited variations in lift and drag at different angles of attack (AoA). Various types and shapes of dimples were considered for the surface

modifications.

The results obtained from the study demonstrated that the presence of dimples increased the stall angle of the airfoil. When the flow encounters a dimple on the airfoil's surface, it leads to the formation of a small separation bubble within the cavities. This bubble formation accelerates the flow between the dimples on the airfoil's surface, causing the boundary layer to transition from laminar to turbulent. As a result, there is a delay in the separation of flow from the airfoil, leading to a significant reduction in drag force.

These findings highlight the positive impact of dimples in altering the aerodynamic performance of the airfoil. By introducing dimples, the flow separation is delayed, resulting in a more favorable stall angle and a substantial reduction in drag force.

Despite the efforts invested in blade design research for wind turbines, there is a lack of specific studies regarding the optimal positions and geometries of blades for domestic-scale wind turbines. The common aspects among all these researches is the size of the wind turbine, when a wind turbine has been considered, or the shape of the airfoil. In fact no one domestic application has been considered, and this is the segment where stall controlled wind turbine are usually used. In fact, for greater powers, control systems like active pitch control are used to guarantee the best power production with a greater range of wind.

Domestic wind turbines differ from their industrial-scale counterparts in terms of size, power, and space requirements, necessitating a tailored analysis for this particular application. Therefore, this study aims to fill this research gap by focusing on finding the best position and geometry for blades in domestic-scale wind turbines. The objective is to maximize wind efficiency and delay stall through optimized blade design.

Methodology

The study employs a numerical simulation approach utilizing aerodynamic models. Advanced simulation software like Ansys Workbench and Ansys ICEM CFX will be utilized to conduct detailed analyses of different positions and geometries for the blades of domestic wind turbines. Various parameters will be considered, including angle of attack, the placement of dimples and their geometry.

Through an iterative process, different configurations will be evaluated, and optimal solutions for a certain blade design in domestic wind turbines will be identified. The dimpled blade will be compared to the baseline blade and the energy produced by the two turbines, keeping constant the external parameters as wind intensity, direction and frequency.

The study's results will be presented and discussed in detail. The effects of different blade configurations on the overall performance of domestic wind turbines will be analyzed. The achieved efficiency levels and stall delay obtained through the optimization of blade design will be evaluated. The best positions and geometries for the reference blades will be identified, providing guidance for future design developments.

Boundary Layer

When a solid body interacts with a fluid in motion, two distinct fluid dynamic regions are generated, one with negligible friction effects and another where these effects are relevant. The latter region is in contact with the solid body and is known as the **boundary layer**. Within this region, the fluid's velocity varies from 0 at the portion in contact with the body to a defined value equal to the undisturbed velocity of the fluid. As could be seen in the Fig. 1.1, the line that divide the boundary layer from the region where the friction effects become negligible defines the thickness of the boundary layer, and it's generally defined for a section where the velocity of the fluid in the boundary layer reaches the 99% of the value of undisturbed velocity [23].

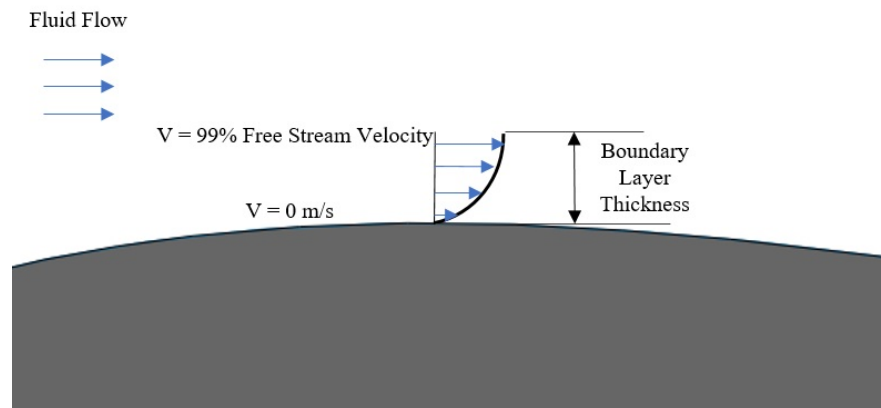


Figure 1.1: Boundary layer thickness [33]

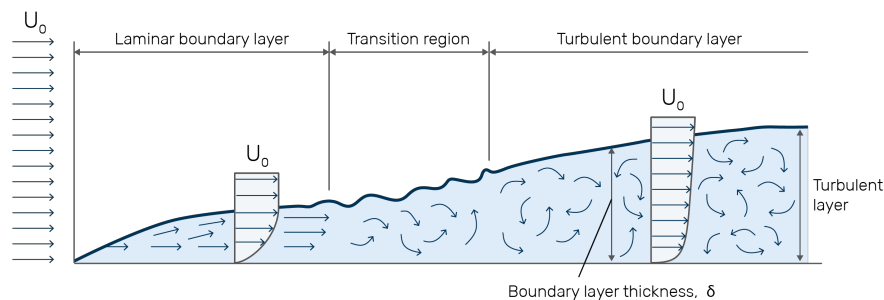


Figure 1.2: Laminar and turbulent boundary layer [8]

1.1 Prandtl's boundary layer concept

Ludwig Prandtl, a German fluid dynamicist, first proposed the concept of the aerodynamic boundary layer in 1904. This theory simplifies the equations of fluid flow by dividing the flow into two areas: one inside the boundary layer, governed by viscosity and responsible for the majority of drag, and one outside the boundary layer, where viscosity can be ignored. By significantly simplifying the full Navier-Stokes equations, it is possible to obtain a closed-form solution for the flow in both areas.

At high Reynolds numbers, typical of full-sized aircraft, it is desirable to have a laminar boundary layer. This results in a lower skin friction due to the characteristic velocity profile of laminar flow. However, the boundary layer inevitably thickens and becomes less stable as the flow develops along the body, and eventually becomes turbulent, the process known as boundary layer transition.

At lower Reynolds numbers, such as those seen with model aircraft, it is relatively easy to maintain laminar flow. This gives low skin friction, which is desirable. However, the same velocity profile which gives the laminar boundary layer its low skin friction also causes it to be badly affected by adverse pressure gradients. As the pressure begins to recover over the rear part of the wing chord, a laminar boundary layer will tend to separate from the surface.

1.2 Boundary layer equations

One of the most significant advancements in fluid dynamics was the derivation of the boundary layer equations. These equations simplify the well-known governing Navier-Stokes equations of viscous fluid flow considerably by employing an order of magnitude analysis within the boundary layer.

The fluid motion within the boundary layer can take on either a *laminar* or *turbulent* form, each characterized by distinct levels of frictional forces (as depicted in Fig. 1.2). Both laminar and turbulent boundary layers are subject to the influence of pressure gradients along the direction of flow, with a favorable pressure gradient arising when the pressure decreases along the flow path and an inverse pressure gradient arising when the pressure increases along the flow path. In accordance with the principle of energy conservation, the velocity of the fluid increases under a favorable pressure gradient and decreases under an inverse pressure gradient.

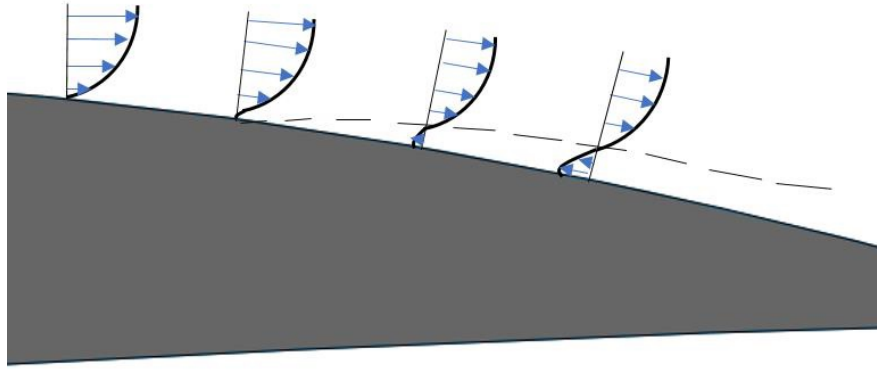


Figure 1.3: Velocity profile along airfoil [33]

Considering two sections A and B:

$$p_A - p_B = -\frac{1}{2}\rho (W_A^2 - W_B^2) \quad (1.1)$$

If the pressure increases between A and B ($p_A < p_B$) the velocity decreases ($W_A > W_B$) and vice versa. Frictional forces within the boundary layer cause a reduction in the kinetic energy of the fluid, and an adverse pressure gradient can cause the flow to reverse direction close to the surface of the body. At low Reynolds numbers, the laminar boundary layer is more likely to separate from the surface, while at higher Reynolds numbers it tends to destabilize and become turbulent.

When considering the angle of attack, the velocity of the fluid on the suction side of the airfoil increases rapidly near the leading edge. On the other hand, fluid velocity on the pressure side tends to decrease. On the suction side, there are many inverse pressure gradients which have varying intensities; these intensities grow on the suction side as the angle of attack increases and vice versa on the pressure side. Considering the response of the boundary layer to the inverse pressure gradients, separation and stall are promoted on the suction side of the airfoil as the grow of the angle of attack. Consequentially, since the laminar boundary layer is relatively weak and it cannot support large inverse pressure gradients, the transition to the turbulent flow must occurs before reaching zones with too large inverse pressure gradients, otherwise the separation and stall occur.

In summary, an airfoil produces lift as long as the boundary layer can manage the pressure distributions established during fluid motion.

1.3 Effects of Reynolds number on the performances

Reynolds number could be referred to the chord length of the blade with the following expression:

$$Re = \frac{\rho c W_{\infty}}{\mu} \quad (1.2)$$

where μ is the dynamic viscosity of the air, c is the chord length of the blade, ρ is the density of the air which depends on the temperature of the air itself and W_{∞} is the undisturbed velocity upstream. Considering the wind turbines, Reynolds number could varies within a range of one up to many million [6]. As mentioned before, with high Reynolds numbers the laminar boundary layer is less stable and the transition to the turbulent one may happen before; on the other hand, turbulent boundary layer is really energetic and it's able to support high inverse pressure gradient before the separation happens.

It is commonly understood that when momentum of momentum is transferred from the external fluid to the boundary layer, the momentum of momentum of the boundary layer increases, allowing it to resist adverse pressure gradients and delay separation.

Aerodynamic devices

2.1 Aerodynamic devices

One way to enhance mixing in the boundary layer is through the use of aerodynamic devices, which can increase turbulence or create swirling structures that help to mix the fluid. The ultimate effect of these devices is to energize the boundary layer. Some examples of these aerodynamic devices include:

- Vortex generators, small devices that generate vortices in the flow to energize the boundary layer and delay separation;
- Gurney flaps, small vertical extensions on the trailing edge of a wing that create a pressure difference to energize the boundary layer and improve lift;
- Dimples, small circular or elliptical depressions on the surface that creates vortices that energize the boundary layer;
- Turbulators, strips of material placed on the surface of the wing to create small disturbances in the boundary layer, promoting mixing and delaying separation;
- Boundary layer suction: a method to actively remove air from the boundary layer, reducing the thickness of the boundary layer and delaying separation.

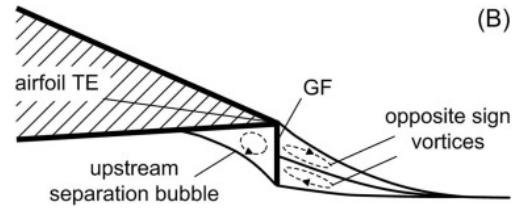
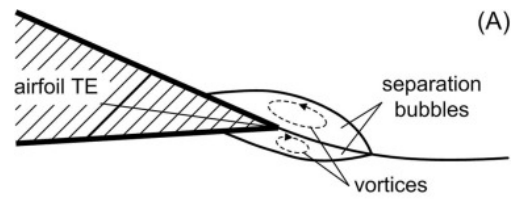
By increasing the lift coefficient generated by the airfoil, these devices can reduce the chord length required to generate the same amount of lift. This reduction can be as much as 10-50%, which can decrease the mass of the blade, particularly in the section near the hub. These devices are typically found on stall-controlled wind turbines and are positioned between 20% and 30% of the chord length in the sections nearest to the blade root, according to Battisti L. [6].

2.1.1 Triangular vortex generators

Vortex generators are typically triangular elements that generates vortex; the main advantage of this solution is the simplicity with which they could be installed on the



(a) Vortex generators on WT blade [10]



(b) Gurney flap [34]

blade: they are generally glued on the surface once the blade is finished. The disadvantages of this solution are mainly the fact that the blade, and also the airfoil geometry, are not design considering the presence of these aerodynamic devices in the design step: thus, the performances in the real world could be different from the ones assumed during the design process.

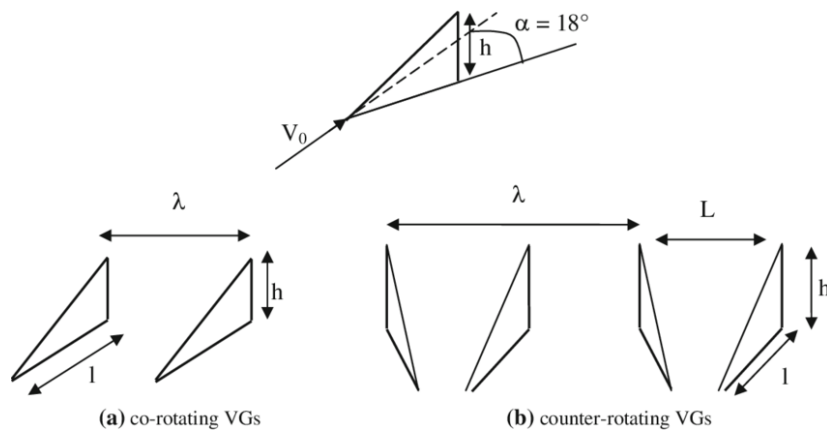
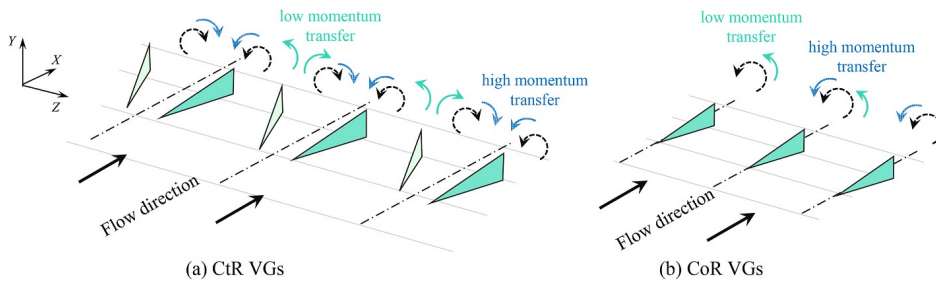


Figure 2.1: Triangular vortex generators, CoR (a) and CtR (b) [16]

2.2 Three-dimensional rotational effect

In recent times, there has been increased interest in how the three-dimensional rotating effect of wind turbine blades affects the behavior of vortex generators (VGs). Researchers such as Zhu et al. [41] have shown that there is a significant difference in the flow fields of blades with VGs due to rotational effects, and that the three-dimensional rotating effect has a considerable impact on delaying flow separation for the inner part of the blade. Jiang et al. [28] conducted experiments with 30 pairs of VGs on each blade to investigate the interaction between the turbulent dynamic rotational effect (TDRE) and VGs on wind turbine aerodynamics under different wind velocities. The studies mentioned above reveal that the TDRE plays a role in the behavior of VGs due to its ability to suppress the size of detached eddies. VGs can be oriented in two ways, namely the counter-rotating (CtR) and co-rotating (CoR) orientations. Several studies suggest that CtR VGs are more effective than CoR VGs at preventing airflow separation.

According to Zhu et al. [41], the TDRE rotational effect of the blade generates a spanwise velocity on the blade surface, which is more prominent near the inner part of the blade and diminishes towards the blade tip. As a result, the stall occurs primarily at the root part of the blade where VGs are placed. In summary, it is impossible for the upstream airflow to flow across the CtR VGs mounted on the wind turbine blade with the same inflow angle. In another study, Jiang et al. [19] investigated the effect of VG orientation, considering the 3D rotational effect. They concluded that the rotational effect of a wind turbine blade produces a spanwise velocity component on the airfoil surface.

The effectiveness of CtR VGs compared to CoR VGs in traditional studies on VGs assumes that the incoming airflow is normal to the array of VGs, regardless of whether it is on a flat plane, airfoil or wind turbine blade. However, under abnormal inflow conditions, the relative effectiveness of these two VG orientations may differ.

Other important results they achieved are:

1. When the inflow is inclined, a pair of CtR VGs generates a pair of asymmetric vortices behind them (Fig. 2.2). As the inflow is more inclined, a pair of CtR VGs sheds two vortices with the same rolling direction but different strength. At this time, the action of CtR VGs has become much closer to that of CoR VGs, but their performance is much lower than that of CoR VGs.
2. The effect of CoR VGs is more effective due to their inflow angles, which are all

large enough under the TDRE.

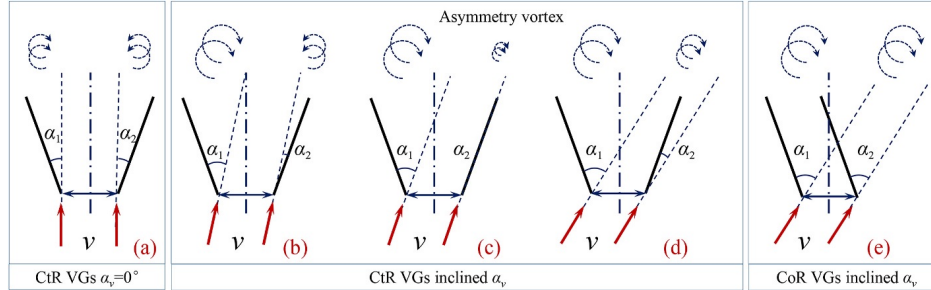


Figure 2.2: Diagram of physical mechanism of VGs [19]

2.3 Dimples

Dimples are small depressions on the surface which are usually permanent like in case of a golf ball. The presence of dimples increases the amounts of energy and linear momentum that are available to those particles of fluid that move in a tiny region near the surface of the ball called the boundary layer as shown in. Among other results in introducing dimples, it indicates two relevant things, namely:

1. The changes in velocity noted earlier increase both the kinetic energy and the linear momentum of the whole flow within the boundary layer;
2. Turbulent flow has more kinetic energy and more linear momentum than laminar flow. When bumping is vigorous enough, its net result is that the bulk flow of air in the boundary layer becomes turbulent.

2.3.1 Circular dimples

The symmetrical geometry of circular dimples allows them to behave consistently without being affected by the three-dimensional rotational effect. However, variations in dimple geometry such as diameter, thickness, position along the chord length, and density along the spanwise of the blade can still affect their performance. Additionally, dimples can be positioned either inward or outward with respect to the plain airfoil.

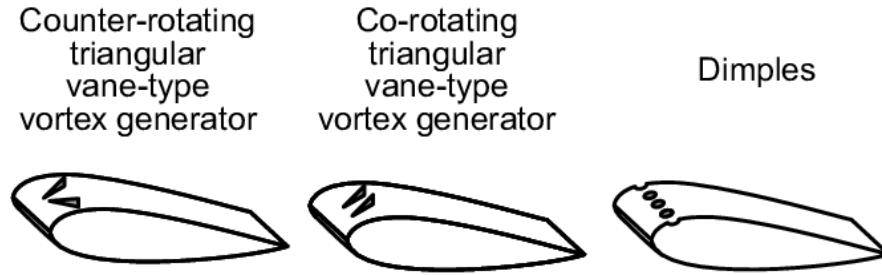


Figure 2.3: Comparison among CtR, CoR and dimples [37]

In their study, Fikade et al. [14] aimed to investigate the impact of different dimple geometries, particularly focusing on inward and outward positioning. The results of their analysis indicate that when the airfoil is at a null angle of attack, the configuration with outward dimples generates a higher drag force but does not produce additional lift. This trend is also observed at higher angles of attack, suggesting that the outward dimple configuration may not be the most efficient choice.

In contrast to the outward dimple configuration, the inward dimple configuration was also tested under similar conditions and was found to generate greater lift than the baseline airfoil, while the increase in drag was not significant. Additionally, this configuration was found to delay the detachment of the boundary layer, leading to a delayed stall.

To address the issue of boundary layer separation on the pressure side of the airfoil, the researchers explored another solution of placing inward dimples on both sides of the airfoil. They used the S830 airfoil profile and observed that the boundary layer separation can occur on the pressure side of the airfoil at negative angles of attack. To address this, they placed 1 *cm* diameter inward dimples on the pressure side and 0.5 *cm* inward dimples on the suction side.

The first set of dimples was placed at 80% of the chord length while the second set was placed at 50%. The outcomes of this approach showed promise in terms of its effectiveness in delaying flow separation, but its implementation could be potentially costly for small wind turbines like the one being analyzed.

Another test was made by Uddin et al. [26] considering a NACA-4415 profile with a chord length of 210 mm. The result they achieved are similar to the ones reported by Fikade [14] and, in particular:

- There is no flow separation for both model (regular and dimpled) at zero attack angle.

- As the attack angle increased from 0° to 12° , flow separation occur at plain surface model.
- As the attack angle increased from 12° to 14° clear flow separation appeared on the upper surface.
- At angle of attack 12° flow remain attached with the upper surface in case of dimpled surface.
- At 16° angle of attack the flow is separated from the upper surface in case of dimpled surface.

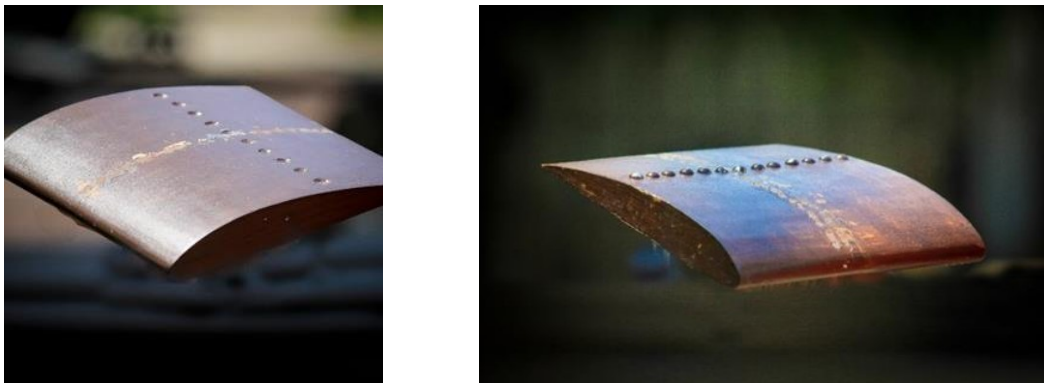


Figure 2.4: Inward and outward dimples [26]

The study found that both inward and outward dimpled airfoils generate more lift than a plain airfoil configuration at corresponding angles of attack. Furthermore, both inward and outward dimpled models exhibit a uniform increase in lift across all angles of attack considered in the study. Additionally, both inward and outward dimpled airfoils show a decrease in drag compared to the plain airfoil model. Among the outward and inward dimpled airfoil models, the outward configuration exhibits the least amount of drag. Finally, the angle of stall also increased in the case of the dimpled airfoil.

Site analysis

It is crucial to conduct a thorough site analysis to assess the feasibility of wind turbine installation. One of the key considerations in this preliminary analysis is the wind intensity at the proposed installation site. Insufficient wind intensity may result in the inability to generate the required power. Additionally, the frequency of a certain wind speed is also an important factor to consider. If the wind is too gusty, discontinuous, or lacks stability, it may not be possible to produce the necessary energy, resulting in a longer pay-back time.

Therefore, a precise site analysis is necessary to determine whether the project is feasible.

3.1 Windiness

When the windiness of a site is analysed, it's desirable to describe the wind by statistical methods; this approach is used to simplify the analysis because the wind intensity and its direction are continuously changing.

The initial step is to collect data regarding the speed, the frequency and the direction of the wind. In general, the data are collected making an average between 10 minutes timesteps, to overcome the problems of turbulence. Once the data are collected, the first relevant value that must be determined is the *average speed* (Eq. 3.1):

$$\bar{v} = \frac{1}{\Delta\tau_{tot}} \sum_i v_i \Delta\tau_i \quad (3.1)$$

If the probability of having a certain wind speed is desired, it's sufficient to divide the timestep in which there is this intensity by the total time, as following (Eq. 3.2):

$$p(v_i) = \frac{\Delta\tau_i}{\Delta\tau_{tot}} \quad (3.2)$$

3.1.1 Weibull statistical distribution

The temporal distribution of the wind speed for a certain site is usually described using the *Weibull statistical distribution*, from the name of the Swedish mathematician Waloddi Weibull. It is based on two parameters, named respectively:

- **s** *scale parameter*
- **k** *shape parameter*

The expression used to define the probability density function according to Weibull is the eq. 3.3:

$$D\langle v \rangle = \frac{k}{s} \left(\frac{v}{s} \right)^{k-1} \cdot e \left[- \left(\frac{v}{s} \right)^k \right] \quad (3.3)$$

Weibull distribution is generally assumed to be adequate to represent 10 minutes timestep wind velocities.

Another important function that is relevant is the *Cumulative distribution function* (Eq. 3.4):

$$\prod_0^v = \int_0^v D\langle v \rangle \cdot dv = \left| -e \left[- \left(\frac{v}{s} \right)^k \right] \right|_0^v = 1 - e \left[- \left(\frac{v}{s} \right)^k \right] \quad (3.4)$$

Knowing the importance of the Weibull distribution, the average wind speed could be write using the shape and scale parameters:

$$\bar{v} = \frac{1}{\Delta\tau} \int_{\Delta\tau} v \cdot d\tau \quad (3.5a)$$

$$\bar{v} = \int_0^\infty v \cdot D\langle v \rangle \cdot dv \quad (3.5b)$$

$$\bar{v} = s \cdot \Gamma \left\langle 1 + \frac{1}{k} \right\rangle \quad (3.5c)$$

Where the gamma function is defined as:

$$\Gamma\langle x \rangle = \int_0^\infty y^{x-1} \cdot e^{-y} dy \quad (3.6)$$

Once the average velocity is defined, is useful to define also the variance in order to understand better the shape of the distribution function; the variance is obtained by the eq. 3.7:

$$\sigma = \sqrt{\frac{1}{n-1} \sum_{i=1}^n (v_i - \bar{v})^2} \quad (3.7)$$

Where n is the number of velocities and \bar{v} is the average velocity. This parameter of variance could be written in dimensionless form, with reference to the average velocity, such as in Eq. 3.8:

$$\sigma_R = \frac{\sigma^2}{\bar{v}^2} = \sqrt{\frac{\Gamma\left\langle 1 + \frac{2}{k} \right\rangle}{\Gamma^2\left\langle 1 + \frac{1}{k} \right\rangle} - 1} \quad (3.8)$$

This is function only of shape factor parameter k and from theory is assumed that the value of the shape factor k is indicative of the variability of the wind speed around the average value: high values of k (3 or higher) indicate a site where the wind speed varies little around the average annual value, while low values of k (such as 1) indicate wind of high variability.

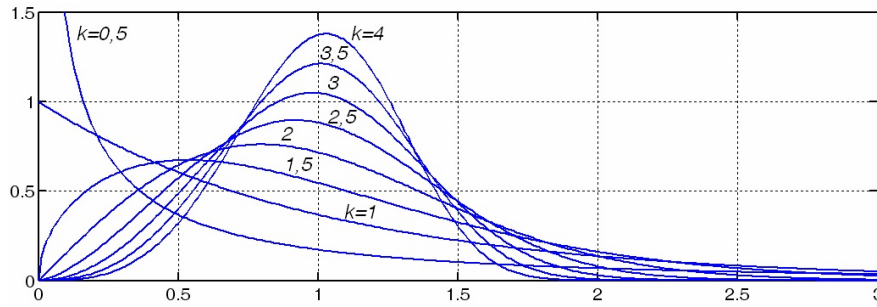


Figure 3.1: Weibull probability density

The last parameter that is useful to describe the site where the wind turbine could be installed, is the fluctuation coefficient, which is defined in the equation 3.9:

$$k_f = \frac{\bar{v}_3}{\bar{v}} = \frac{\Gamma^{1/3}\left\langle 1 + \frac{3}{k} \right\rangle}{\Gamma\left\langle 1 + \frac{3}{k} \right\rangle} \quad (3.9)$$

where, \bar{v}_3 is the *mean cubic speed* defined in eq. 3.10:

$$\bar{v}_3 = \sqrt[3]{\frac{1}{\Delta\tau} \int_{\Delta\tau} v^3 d\tau} \quad (3.10a)$$

$$\bar{v}_3 = s \cdot \Gamma^{\frac{1}{3}}\left\langle 1 + \frac{3}{k} \right\rangle \quad (3.10b)$$

It represents the ratio between the mean cubic speed, which is the wind speed corre-

sponding to the maximum theoretical energy extraction, and the average wind speed of the site analysed.

3.1.2 Rayleigh distribution

When the shape factor is 2 ($k = 2$) the Weibull distribution is referred to as the Rayleigh distribution, a situation which is very often taken as a reference to define the generic performance of a wind turbine (without referring to a particular application site). In this case, the characteristic parameters of the statistical distribution can be written as:

$$\Gamma\left\langle 1 + \frac{1}{k} \right\rangle = \frac{\bar{v}}{s} = \frac{\sqrt{\pi}}{2}$$

$$D\langle v \rangle = \frac{\pi}{2} \left(\frac{v}{\bar{v}} \right) \cdot \exp \left[-\frac{\pi}{4} \left(\frac{v}{\bar{v}} \right)^2 \right]$$

$$\prod_0^v \langle v \rangle = 1 - \exp \left[-\frac{\pi}{4} \left(\frac{v}{\bar{v}} \right)^2 \right]$$

3.1.3 Study case

In the present study the windiness of the site has been characterized by evaluating the scale and shape parameters of the Weibull distribution that describes the site. In particular:

1. The probability of having a certain wind speed has been evaluated;
2. The cumulative probability has been evaluated;
3. The mean velocity \bar{v} has been calculated as the mean velocity among all the listed ones;
4. The standard deviation between the mean velocity and the referred velocity has been evaluated for all the listed velocities;
5. The $(\ln(-\ln(1 - F(v))))$ has been plotted versus $(\ln v)$, where the $F(v)$ is the cumulative probability. For this plot, velocities between 4 and 14 m/s have been considered (Fig. 3.2);
6. A trendline has been created to linearize the curve generated with the plot;
7. The angular coefficient of the trendline has been considered to be the **k** *shape parameter*;
8. Using MATLAB, the gamma function $\Gamma\left\langle 1 + \frac{1}{k} \right\rangle$ has been evaluated;

9. Scale parameter s has been evaluated as $\frac{\bar{v}}{\Gamma\left(1+\frac{1}{k}\right)}$;
10. Weibull distribution has been plotted.

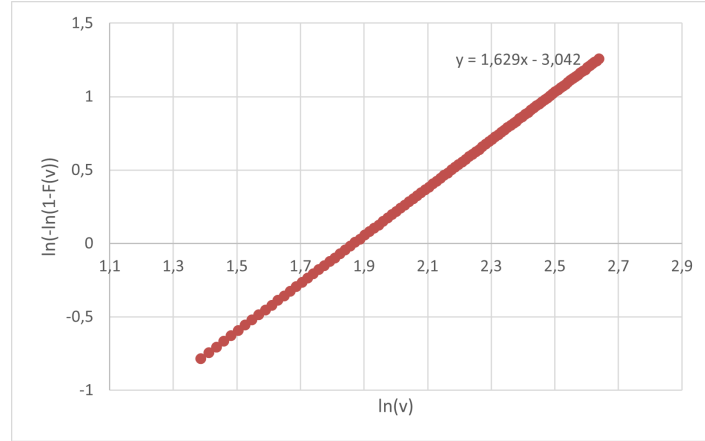


Figure 3.2: $\ln(-\ln(1 - F(v)))$ vs $\ln v$

In particular, for this site:

k	1.629
s	6.278 m/s

Table 3.1: Shape and scale parameters

3.1.4 Roughness

The wind speed values obtained from measurements in a given site are generally evaluated at a fixed height above the ground, and are commonly averaged in the short term: the IEA and IEC standards establish an average period of 10 min. The wind speed values considered previously refer to this situation: they therefore mediate instantaneous speed fluctuations (turbulence) and short-term fluctuations (gusts); these data are considered suitable for evaluating the annual energy generation of a wind generator. A model generally used in the wind industry to evaluate the variation of wind speed with altitude is the *logarithmic Prandtl model*, which is based on the general theory of the dynamic boundary layer:

$$v_z = v_0 \frac{\ln(z/m)}{\ln(z_0/m)} \quad (3.11)$$

with m roughness coefficients that depends on the class of ground. Typical values are reported in the Table 3.2:

CLASS	m [m]	DESCRIPTION
0	0.0002	Still water surface
0.5	0.0024	Wide open territories with smooth surface (e.g. airports)
1	0.03	Open agricultural areas without fences and hedges and with lots of buildings radio; gently sloping hills
1.5	0.055	Agricultural areas with few houses and 8 m height fences, medium distance 1250 m
2	0.1	Agricultural areas with few houses and 8 m height fences, medium distance 500 m
2.5	0.2	Agricultural areas with many houses and shrubs or 8 m height fences, medium distance 250 m
3	0.4	Villages, small towns agricultural areas with many hedges and shrubs
3.5	0.8	Big cities with many tall buildings
4	1.6	Metropolis with tall buildings and skyscrapers

Table 3.2: Roughness coefficients m

Typical path of wind velocity regarding height from the ground is represented in Fig. 3.3

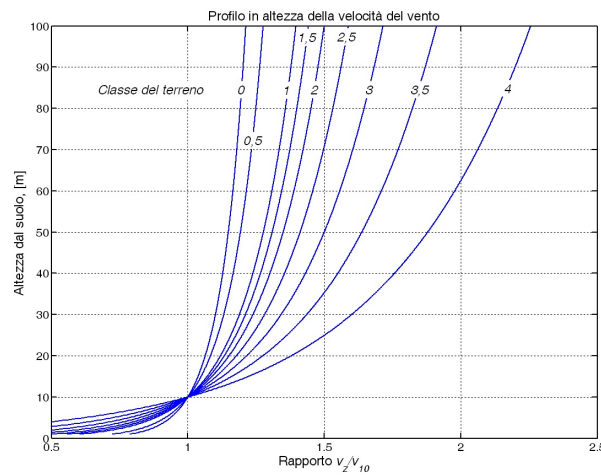


Figure 3.3: Wind speed profile as function of height

3.2 Velocities

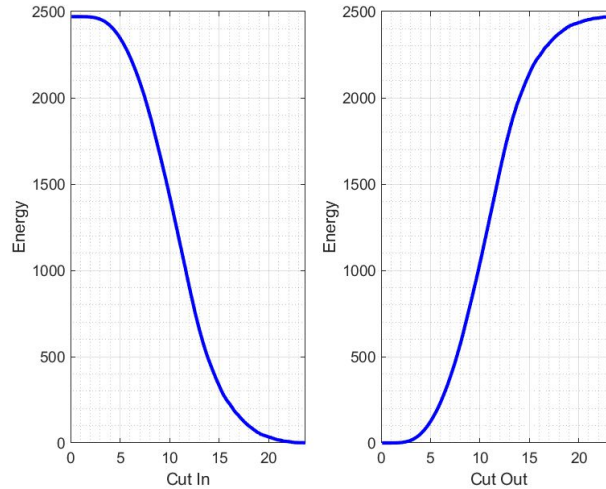


Figure 3.4: Cut-in and cut-out velocities effect on energy produced

Cut-in velocity

The **cut-in** velocity is the minimum velocity at which the wind turbine starts to generate electrical power. Generally, this velocity is within the range of $3 - 6\text{ m/s}$ because the wind with this velocity has enough kinetic energy to put in motion the turbine.

To set up the proper cut-in velocity is sufficient, after checking possible structural problems, to evaluate the curve of energy produced along the year varying the cut-in velocity (Fig. 3.4a): for cut-in velocity *below* $4 - 5\text{ m/s}$ there's no increasing in energy production, thus isn't necessary to design the blade geometry to exploit the energy of the wind in this range of velocity.

Cut-out velocity

The **cut-out** velocity is the maximum velocity at which the turbine ends to produce electrical power. This is not a limit introduced by structural limits but it's a safety limit, to be sure that the forces acting on the blade don't influence the neither the structure nor the energy produced. In fact, considering the graph in Fig. 3.4b, once the cut-out velocity *above* $15 - 20\text{ m/s}$ the energy produced along the year doesn't rise too enough to justify the design optimization for this range of velocity.

Summing up the considerations, it is better to focus within a certain range of velocity to design a blade geometry that has an higher efficiency in this range, rather than optimize a blade for a larger range but with a lower efficiency.

Nominal velocity

The **nominal** velocity is the velocity for which the wind turbine produces, in theoretical conditions, the nominal power; in real conditions the velocity at which there is nominal power production could be slightly different (in term of tents of m/s due to the losses and the turbulence). When the wind turbine is equipped with control system to regulate the power produced, the nominal power is fixed around the value that guarantees the maximum energy production along the year; considering Fig. 3.5, the choice of the nominal velocity is really important because if it's assumed to be too high, a great amount of energy would be dissipated: in fact, the area between the dotted line and the solid one represent the energy not exploited. But, on the other hand, if the nominal velocity is set to be lower we may have a lower efficiency of the turbine at higher wind velocity and also the control system must be regulated for a larger range of wind velocity.

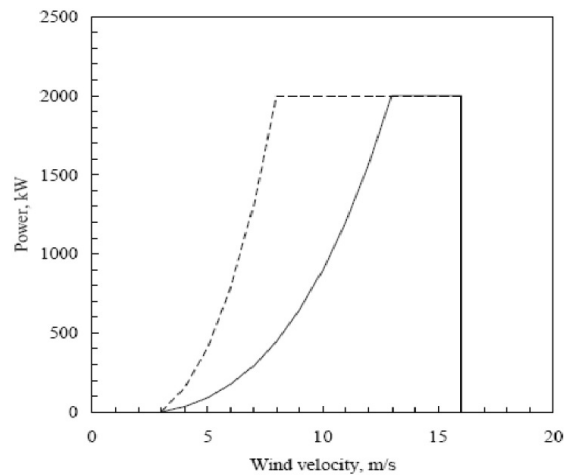


Figure 3.5: Power profiles for different nominal velocities

Energy

4.1 Energy produced

Once the power produced by the blades at each velocity is known, it is possible to estimate the energy captured. The energy can be calculated using the following equation:

$$E = 8760 \cdot \int_{v_{\text{cut-in}}}^{v_{\text{cut-out}}} P_v \cdot f(v) dv \quad (4.1)$$

This equation represents the integral over the course of a year, from the cut-in wind velocity ($v_{\text{cut-in}}$) to the cut-out wind velocity ($v_{\text{cut-out}}$), of the power produced at each wind velocity (P_v) multiplied by the probability density function of the wind speed ($f(v)$). In other words, it calculates the energy as the product of power and the likelihood of encountering a certain wind speed.

Alternatively, the entire range of wind speeds can be divided into smaller intervals, and the probability of obtaining the mean velocity within each interval can be evaluated. Then, the energy can be estimated using the following equations:

$$E = \sum 8760 \cdot \Delta v \cdot DP \quad (4.2a)$$

$$E = \Delta v \cdot 8760 \cdot \sum DP \quad (4.2b)$$

In these equations, Δv represents the width of each velocity interval, and DP represents the probability of obtaining the mean velocity within that interval multiplied by the power produced by the WT with that wind speed. The energy is calculated by summing up the product of the interval width, the number of hours in a year (8760), and the DP for each interval, or equivalently, by multiplying the interval width, the number of hours in a year (8760), and the sum of all the DPs.

In the case study, a wind speed difference (Δv) of 2 m/s was utilized for wind speeds ranging from 4 to 10 m/s . For wind speeds between 10 and 14 m/s , a wind speed difference of 1 m/s was employed.

4.1.1 Capacity factor

Once the energy produced by the two configurations, the **capacity factor** could be estimated. It's the ratio between the energy produced along the year and the product between nominal power and 8760. It represents the ratio between the energy effectively produced and the energy that WT could generate if it operates all the year at constant nominal power. It is defined with the Eq. 4.3

$$C_F = \frac{E}{T \cdot P_R} \quad (4.3)$$

Where E is the energy produced in [$kWh/year$], T is time in [h] and P_R is the nominal power in [kW].

There are several factors to be considered when determining the capacity factor of a power plant. Gathering information from various online sources, it becomes clear that estimating the average capacity factor relies heavily on aspects such as the plant's nominal power, the specific location of installation, and the technology employed. Making a rough estimation, the C_F varies between 20% and 40% (1752 h/y - 3504 h/y) for a wind power plant located in Italy; moreover the higher percentage is reached in large power plant, with a magnitude order of MW . Thus is estimated a C_F value of around 20% for the on-shore micro eolic plant such as the one in the study.

Turbulence model

Turbulent flows exhibit a vast array of swirling structures at varying scales in both time and space. These structures interact with each other and transfer energy. The larger structures contain the majority of the kinetic energy for the flow. As these structures are fragmented into smaller ones, the energy is passed down to progressively smaller scales. This process of energy transfer from large to small scales is known as the *direct energy cascade*, and it continues until the kinetic energy is converted to thermal energy by viscous dissipation. The *Kolmogorov length scale*, from the mathematician Andrey Kolmogorov, marks the scale at which this conversion occurs.

Modelling turbulence is one of the most crucial aspects of CFD modelling, and accurately capturing turbulence is essential for obtaining reliable CFD results. There are many possibilities in turbulence modelling as shown in Fig. 5.1.

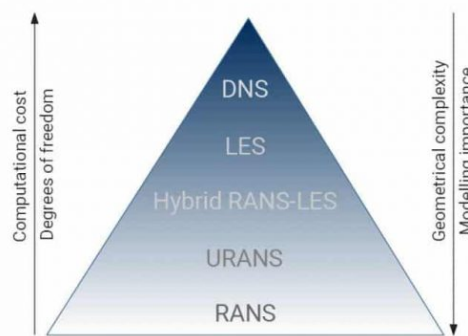


Figure 5.1: Turbulence models in CFD, from DNS to RANS [18]

5.1 Direct Normal Simulations - *DNS*

The first one is to solve directly the governing equations of fluid flows, the **Navier-Stokes equations**, without the use of any modelling assumption. This approach is called **Direct Normal Simulation** or DNS and it requires to solve the extensive

range of temporal and spatial scales of a turbulent flow, from very large to very small, down to the Kolmogorov length scale. It can be estimated that the mesh resolution and time steps required to correctly solve the complexity of the fluid structures scales approximately with the cube of Reynolds number. For practical reasons this approach could be used only for small parts that must be analysed and its approach is virtually impossible for engineering applications.

5.2 Large Eddy Simulations - *LES*

In LES, the smallest scales of turbulence are spatially filtered out while the largest, most energy containing scales are resolved directly. Due to the nature of turbulence, at a very small scale, the flow structures tend to be similar to each other even in different applications. This allows the use of simpler turbulence models that tend to be more universal and can be applied to several applications with a reduced requirement of model tuning. LES modelling offers increased range of applicability and increased fidelity of the solution but all of this comes with an increased computational cost due to the time step requirements, as the flow can not be considered steady anymore, and increased mesh resolution required to capture more details of the flow.

5.3 Reynolds Averaged Navier-Stokes - *RANS*

Another possibility is the use of **RANS models**, which is the acronym of **Reynolds Average Navier-Stokes** equations. If the Reynolds number is large, the flow around the body will be turbulent, and if a snapshot of the flow is taken, it would seem that the initially organised and ordered flow would develop a dynamic chaotic motion with a large range of vortex. Zooming in on a region downstream of the body, it would continue to see more and more intricate and small structures that vary in space and time. If the experiment is repeated with the same conditions several times, each time a different evolution of the flow could be seen. Nonetheless, by superimposing diverse solutions and computing an ensemble average, coherent structures in both space and time may be discerned. In the absence of temporal variations or periodicity in the flow, the results may also be averaged over time to augment the sampling of the mean.

RANS equations are very similar to the original equations but contains some additional terms in the momentum equations called Reynolds stress terms that are unknown and need to be modelled. RANS modelling is the most common and widespread ap-

proach in industrial applications but they have some limitations due to the modelling assumptions used to derive the mathematical formulation of the model. For certain applications, it might be required to use more detailed approaches that instead of modelling all of the turbulence scales, try to resolve the most energy containing structures of the flow.

The technique used to derive the RANS equations is called Reynolds decomposition. Reynolds averaging and Reynolds decomposition do not refer directly to a manipulation of the Reynolds number, but rather to an application of time averaging to the Navier-Stokes equations. Time averaging is often used to reduce complex systems of differential equations into simpler forms by partially or fully eliminating the time variable. In this case, the RANS equations use a solution that is split into a time-independent mean flow velocity and time-varying fluctuations about the mean, or:

$$u(x, t) = \bar{u}(x) + u'(x, t) \quad (5.1)$$

where \bar{u} is the average velocity and u' is the fluctuating velocity. As suggested by Sidik C., Azwadi N. et al. [9], the time-average of the fluctuating component is zero ($\overline{u'} = 0$) and the average value is expressed as:

$$\bar{u}(x) = \lim_{\Delta t \rightarrow \infty} \frac{1}{\Delta t} \int_{t_1}^{t_1 + \Delta t} u(x, t) dt \quad (5.2)$$

Considering the basic continuity 5.3 equation and Navier-Stokes ones 5.4, where ρ is the density, p is the pressure:

$$\frac{\partial \rho}{\partial t} + \frac{\partial}{\partial x_i}(\rho u_i) = 0 \quad (5.3)$$

$$\frac{\partial}{\partial t}(\rho u_i) + \frac{\partial}{\partial x_j}(\rho u_i u_j) = -\frac{\partial p}{\partial x_i} + \frac{\partial}{\partial x_j} \left(\rho \mu \frac{\partial u_i}{\partial x_j} \right) \quad (5.4)$$

and combining them with 5.2, the Reynolds Averaged Navier Stokes equation obtained is 5.5:

$$\frac{\partial \bar{\rho} u_i}{\partial t} + \frac{\partial}{\partial x_j}(\bar{\rho} u_i u_j) = -\frac{\partial \bar{p}}{\partial x_i} + \mu \frac{\partial^2 \bar{u}_i}{\partial x_j \partial x_j} - \frac{\partial}{\partial x_j} \left(\overline{\rho u'_i u'_j} \right) \quad (5.5)$$

which is similar to 5.3 except for the additional term $\overline{u'_i u'_j}$, which is called *Reynolds stress* [9] and it is expressed as:

$$\overline{u'_j u'_i} = \begin{bmatrix} \overline{u'^2} & \overline{u'v'} & \overline{u'w'} \\ \overline{v'u'} & \overline{v'^2} & \overline{v'w'} \\ \overline{w'u'} & \overline{v'w'} & \overline{w'^2} \end{bmatrix}$$

The elements on the diagonal are representative of the *normal stress* while the other elements constitutes the *shear stress* to which is subjected the fluid. This is known as **closure problem** and to solve it, modelling the Reynolds stresses in terms of mean flow quantities is needed.

The first attempt to solve this problem was proposed by Boussinesq [39] in 1877 and it was based on the analogy with kinematic viscosity in Newton's law for the laminar flow. According to Bussinesq the relation that can be written between stresses and mean strain rate could be expressed by the 5.6

$$\tau_{ij} = \rho \overline{u'_i u'_j} = \frac{2}{3} \rho k \delta_{ij} - \mu \left(\frac{\partial \overline{u}_i}{\partial x_j} + \frac{\partial \overline{u}_j}{\partial x_i} \right) \quad (5.6)$$

where the turbulence kinetic energy k is expressed as:

$$k = \frac{1}{2} \overline{u'_i u'_i} = \frac{1}{2} (\overline{u'^2} + \overline{v'^2} + \overline{w'^2}) \quad (5.7)$$

where k is expressed as the turbulence kinetic energy, μ_t is denoted as the turbulent viscosity and δ_{ij} is the Kronecker delta. The Eddy Turbulent Viscosity μ_t must be calculated to close the problem.

5.3.1 One-Equation Models

This kind of model use a mixing length (l_m) approach to calculate the Eddy viscosity μ_t :

$$\mu_t = \rho k^{1/2} l_m \quad \text{or} \quad \mu_t = \rho l_m^2 \left| \frac{\partial U}{\partial y} \right| \quad (5.8)$$

One equation turbulence models solve one turbulent transport equation, usually the turbulent kinetic energy. The original one-equation model is Prandtl's one-equation model. The Prandtl's mixing length hypothesis supposes that:

$$l_m = ky \quad k = 0.41 \quad (5.9)$$

With y which is the distance from the boundary wall, as shown in Fig. 5.2.



Figure 5.2: Size of Eddies

Since the mixing length is specified algebraically, it's not easy to solve in this form and thus a **transport equation** wants to be solved instead.

Instead of 5.10, solve for 5.11

$$\mu_t = \rho k^{1/2} l_m \quad (5.10)$$

$$\mu_t = C_\mu \frac{\rho k^2}{\epsilon} \quad (5.11)$$

Noting that, from 5.12 mixing length and turbulent transportation ratio ϵ are directly connected.

$$l_m = \frac{C_\mu k^{3/2}}{\epsilon} \quad (5.12)$$

Transport Equation for k The transport equation for k is the following:

$$\frac{\partial(\rho k)}{\partial t} + \nabla \cdot (\rho \mathbf{U} k) = \nabla \cdot \left[\left(\mu + \frac{\mu_t}{\sigma_k} \right) \nabla k \right] + P_k - \rho \epsilon \quad (5.13)$$

Where the first part represents the time dependency, the second factor the **convection** factor, while the first terms on the right side of the = is related to **diffusion** and the last terms are referred to sources and sinks. Other common one-equation models are:

- Baldwin-Barth model [5];
- Spalart-Allmaras model [32];
- Rahman-Agarwal-Siikonen model;
- Wray-Agarwal Turbulence model;
- Shuai-Agarwal Turbulence model.

5.3.2 Two-Equations Models

Generally, the purposed of the two-equation models are to derive two transport equations for two turbulence properties, the turbulence kinetic energy k and one of any others from these turbulence properties which are either the dissipation rate of turbulence kinetic energy ϵ or the specific dissipation rate ω . The two most used models are the $k - \epsilon$ and the $k - \omega$.

5.3.2.1 $k - \epsilon$ models

The $k - \epsilon$ model is one of the most common turbulence models, but it may not be suitable for scenarios with significant adverse pressure gradients [39]. It is a two equation model, that means, it includes two extra transport equations to represent the turbulent properties of the flow. This allows a two equation model to account for history effects like convection and diffusion of turbulent energy.

The first transported variable is turbulent kinetic energy, k . It is the variable that determines the energy in the turbulence. The transport equation used to determine k is the same of 5.13. The second transported variable in this case is the turbulent dissipation rate, ϵ . It is the rate that turbulent kinetic energy is converted into thermal energy by viscosity (Fig. 5.3). It is the variable that determines the scale of the turbulence.

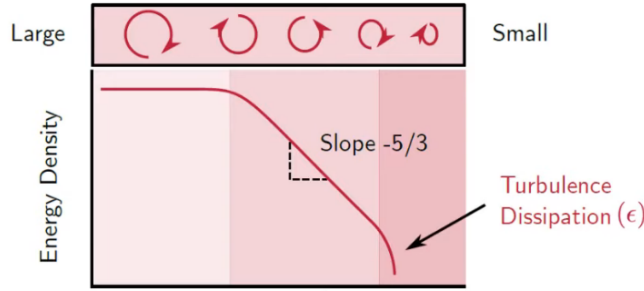


Figure 5.3: Energy density of the eddies. On the $x - axis$, there is the size of eddies decreasing from left to right

Transport equation for ϵ The transport equation to determine the turbulent transportation ratio is:

$$\frac{\partial(\rho\epsilon)}{\partial t} + \nabla \cdot (\rho\mathbf{U}\epsilon) = \nabla \cdot \left[\left(\mu + \frac{\mu_t}{\sigma_\epsilon} \right) \nabla \epsilon \right] + C_1 \frac{\epsilon}{k} (P_k + C_3 P_b) - C_2 \rho \frac{\epsilon^2}{k} + S_\epsilon \quad (5.14)$$

Where the first part represents the time dependency, the second factor the **convection** factor, while the first terms on the right side of the $=$ is related to **diffusion** and the last terms are referred to sources and sinks and the model coefficients C_1 , C_2 and C_3 vary between models; Once the transport equations for k and ϵ are solved, μ_t can be computed as:

$$\mu_t = C_\mu \frac{\rho k^2}{\epsilon} \quad (5.15)$$

This model's primary **constraint** is its inability to make precise predictions for boundary layers with adverse pressure gradients.

5.3.2.2 $k - \omega$ models

The $k - \omega$ model is one of the most common turbulence models [39]; it is a two equation model, that means, it includes two extra transport equations to represent the turbulent properties of the flow. This allows a two equation model to account for history effects like convection and diffusion of turbulent energy. It has been developed to overcome the limits of the $k - \epsilon$ model.

The first transported variable is turbulent kinetic energy, k . It is the variable that determines the scale of the turbulence. The second transported variable in this case is the **specific dissipation rate**, $\omega = \frac{\epsilon}{C_{\mu}k}$. It is the variable that determines the scale of the turbulence.

Transport equation for k The transport equation used to solve k is the same of 5.13:

$$\frac{\partial(\rho k)}{\partial t} + \nabla \cdot (\rho \mathbf{U}k) = \nabla \cdot \left[\left(\mu + \frac{\mu_t}{\sigma_k} \right) \nabla k \right] + P_k - \rho \epsilon \quad (5.16)$$

Transport equation for ω The transport equation used to compute ω is the following:

$$\frac{\partial(\rho \omega)}{\partial t} + \nabla \cdot (\rho \mathbf{U}\omega) = \nabla \cdot \left[\left(\mu + \frac{\mu_t}{\sigma_k} \right) \nabla \omega \right] + \frac{\gamma}{\nu_t} P_k + P_b - \beta \rho \omega^2 \quad (5.17)$$

This model has different empirical coefficients compared to the $k - \epsilon$ one. The main advantage of this models compared to $k - \epsilon$ is that this don't need damping functions to understand the behaviour of the vortex in the zone close to the boundary wall; these functions aren't very accurate in the presence of adverse pressure gradients, like in airfoils. These models are favored over their predecessors due to their superior precision in these particular regions.

The main **weakness** of this model is the dependant of the free stream turbulence conditions. A possible solution could be the one to blend the $k - \omega$ model in the zone close to the boundary wall and the $k - \epsilon$ model in the zone away from it. This is the base of $k - \omega$ *SST* model.

5.3.2.3 $k - \omega$ *SST* model

As improvement of $k - \omega$ model, the $k - \omega$ *SST* model has been developed. It combines the $k - \omega$ model with the $k - \epsilon$ one to take the best from each model and combining them together reach a more precise evaluation of the CFD problem.

The standard $k - \epsilon$ model is characterised by the following equations:

$$\frac{\partial(\rho k)}{\partial t} + \nabla \cdot (\rho \mathbf{U}k) = \nabla \cdot \left[\left(\mu + \frac{\mu_t}{\sigma_k} \right) \nabla k \right] + P_k - \rho \epsilon \quad (5.18)$$

$$\frac{\partial(\rho \omega)}{\partial t} + \nabla \cdot (\rho \mathbf{U}\omega) = \nabla \cdot \left[\left(\mu + \frac{\mu_t}{\sigma_k} \right) \nabla \omega \right] + C_1 \frac{\epsilon}{k} (P_k + C_3 P_b) - C_2 \rho \frac{\epsilon^2}{k} \quad (5.19)$$

but, remembering that $\epsilon = C_\mu k \omega$ and substituting this equation in the 5.19 one, the dissipation equation becomes:

$$\frac{\partial(\rho \epsilon)}{\partial t} + \nabla \cdot (\rho \mathbf{U}\epsilon) = \nabla \cdot \left[\left(\mu + \frac{\mu_t}{\sigma_\epsilon} \right) \nabla \omega \right] + \frac{\gamma}{\nu_t} P_k - \beta \rho \omega^2 + 2 \frac{\rho \gamma \omega^2}{\omega} \nabla k : \nabla \omega \quad (5.20)$$

Comparing this with the expression obtained from the transport equation for ω in the $k - \omega$ model:

$$\frac{\partial(\rho \omega)}{\partial t} + \nabla \cdot (\rho \mathbf{U}\omega) = \nabla \cdot \left[\left(\mu + \frac{\mu_t}{\sigma_k} \right) \nabla \omega \right] + \frac{\gamma}{\nu_t} P_k - \beta \rho \omega^2 \quad (5.21)$$

These equations are the same, with the exception of the additional term, that exists in the $k - \epsilon$ model but not in the $k - \omega$ one¹:

$$2 \frac{\rho \gamma \omega^2}{\omega} \nabla k : \nabla \omega$$

By multiplying this additional term by $(1 - F_1)$, it is possible to blend between the k-omega and the k-epsilon models:

$$2(1 - F_1) \frac{\rho \gamma \omega^2}{\omega} \nabla k : \nabla \omega$$

If $F_1 = 0$, the model is $k - \epsilon$

If $F_1 = 1$, the model is $k - \omega$

Note that every cell in the mesh will have different value of F_1 , thus if it will be equal to 0, the problem in that cell will be solved using $k - \epsilon$ model, and with $k - \omega$ if F_1 will be equal to 1. In general terms, close to the wall $F_1 = 1$ and far away it is close to 0.

In *SST* model, a **viscosity limiter** is also introduced:

$$\mu_t = \frac{\rho k}{\omega} \quad \mu_t = \frac{a_1 \rho k}{\max(a_1 \omega, SF_2)} \quad (5.22)$$

This limiter is used to limit the viscosity of the fluid in the sections close to the bound-

¹The term $\nabla k : \nabla \omega$ could be seen as $\nabla k : \nabla \omega = \frac{\partial k}{\partial x_j} \frac{\partial \omega}{\partial x_j} = \frac{\partial k}{\partial x} \frac{\partial \omega}{\partial x} + \frac{\partial k}{\partial y} \frac{\partial \omega}{\partial y} + \frac{\partial k}{\partial z} \frac{\partial \omega}{\partial z}$

ary wall, when the shear is high.

F_2 is large when the distance from the wall is low.

Hence, the advantages of this model are:

- the $k-\omega$ *SST* model gives better agreement with experiments of mildly separated flows;
- it is best for aerodynamic simulations where the separation of the boundary layer is important and relevant.

5.4 Hybrid RANS-LES models

There is a family of turbulence models where the benefits of LES modelling are being exploited while retaining the efficiency of RANS models where LES would be too expensive. These go under the name of hybrid RANS-LES models. The majority of the mesh resolution tends to be in proximity of surfaces and bodies of interest as in LES the flow needs to be fully resolved near the wall. The cost of LES can therefore be greatly reduced if the constraints of the increased resolution near the wall can be relaxed. One of the most common hybrid approaches uses LES modelling away from the walls and RANS modelling near the wall. This approach is called **Detached Eddy Simulation** - *DES*.

5.4.1 Detached Eddy Simulations - *DES*

Detached eddy simulation (DES) is a modification of a Reynolds-averaged Navier–Stokes equations (RANS) model in which the model switches to a subgrid scale formulation in regions fine enough for large eddy simulation (LES) calculations [38].

The Detached Eddy Simulation approach (DES) was proposed by Spalart et al. in 1997. The original DES proposed combines the RANS and LES in a non-zonal manner. DES is based on the Spalart - Allmaras one equation turbulence model [13]. Length scale, d , is generally taken as the shortest distance at any point to the closest wall in RANS mode. In DES, it is replaced with the minimum between the distance to the wall and a length proportional to the local grid spacing. It is represented mathematically as:

$$d_{DES} = \min(d, C_{DES}\Delta) \quad (5.23)$$

Where C_{DES} is a constant taken equal to 0.65 as suggested by many studies; Δ is the local grid spacing. For structured grids, it is the maximum grid spacing over all three

directions. For unstructured grids, it is generally taken as the maximum edge length connecting the centroids of the adjacent cells.

5.5 Comparison between models

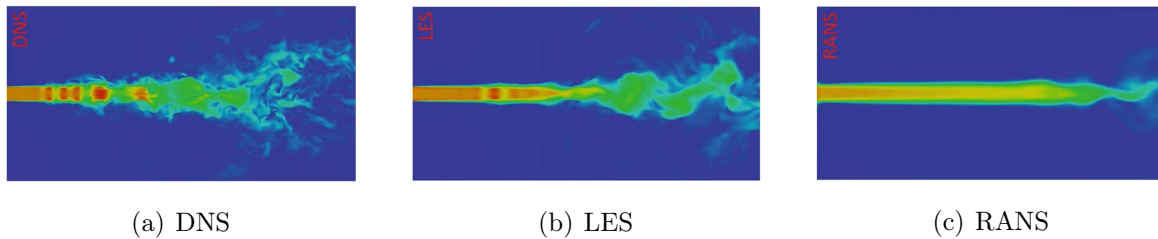


Figure 5.4: Turbulence models example: DNS, LES, RANS [24]

The main differences among the models are:

DNS

- Solving the full unsteady Navier-Stokes equations;
- Resolves the whole spectrum of scales;
- No modeling is required;
- Computational cost is prohibitive for most applications.

LES

- Large eddies are resolved but the eddies smaller than the grid filter are modeled;
- Much less expensive than DNS;
- Sub-grid scale modeling is required.

RANS

- All turbulent length scales are modeled in RANS,
- Least computationally expensive technique;
- Widely used in industrial applications;
- Large number of closure terms to model;
- Lowest accuracy.

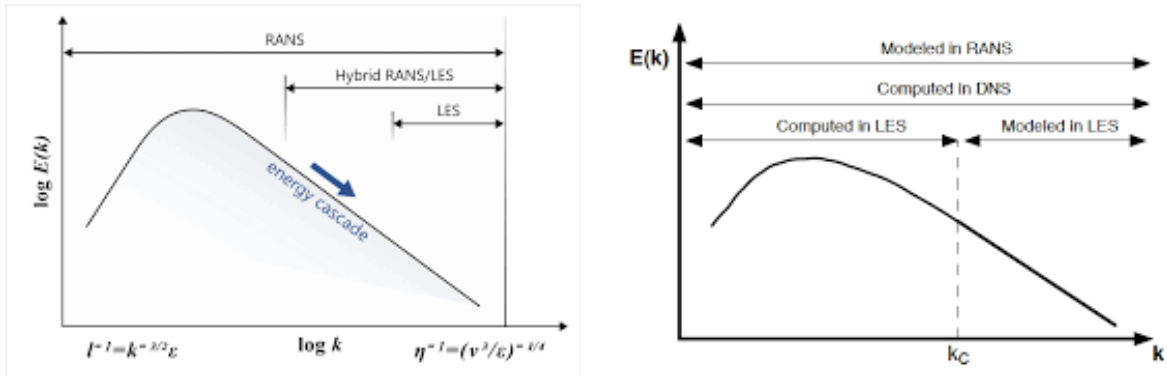


Figure 5.5: Energy distribution and scales in turbulence modeling [3]

From the Fig. 5.5 could be seen the turbulence models and their respective energy spectrum range: for example, RANS models rely on their transport equations to model the entire wave number range, while LES needs a subgrid model to model behaviors of eddies in the dissipative range, but explicitly resolves the large eddies.

5.6 Turbulence models chosen

Once the possible turbulence models have been analysed and pros and cons have been evaluated, the turbulence models could be chosen. For the investigation of the best simple characteristic and position, a Detached Eddy Simulation turbulence model has been chosen; the reasons of this choice were:

- In order to attain high accuracy, the usage of a DES model may yield a greater degree of precision as compared to a RANS model;
- The control volume isn't too large to require a huge amount of computational work;

For the simulations of baseline blade and modified blade geometries, a RANS turbulence model has been chosen; in particular, a Shear Stress Transport, with $\gamma - Re_{\theta,t}$ option for turbulence has been taken in consideration. The reasons were:

- A DES simulation requires too much time in computational terms;
- The two meshes exceed the maximum amount of memory available to carry out the simulation;
- A smaller accuracy is required in these steps of the analysis.

Baseline profile

The performance characteristics that are desired for the wind turbine airfoils depend on the kind of power control used: passive stall, active stall, variable pitch and variable rotational speed. For this reason, during the ages, engineers wanted to find dedicated profiles to optimize the fluid dynamics of the airfoil. The big goals chased were [6]:

1. High C_L/C_D , especially higher than 100-120 and a high $C_{L,max}$;
2. Progressive transition to the stall, trying to avoid the abruptly passage to avoid stress on the structure;
3. Less sensitivity to the fouling: NACA and NASA profiles suffers a lot of this problem because the roughness of the airfoil increases in particular close to the leading edge. This aspect is relevant in the stall controlled turbines;
4. Less noise production.

The conditions for the maximum fluid dynamic efficiency of the profile could be obtained from the equation 6.1:

$$\frac{N_p c}{2\pi r} C_L = \sigma C_L = f(\lambda) \quad (6.1)$$

where: N_p is the number of blades, c is the chord length, r is the radius of the blade, C_L is the lift coefficient, σ is the solidity, λ is the Tip speed ratio. It could be easily seen that exist infinite number of geometries that satisfy the variables for each section of the blade and in particular around the product $c \cdot C_L$. Considering this product, two different philosophies were developed during the years: *low lift profiles* and *high lift profiles* which, of course, generate long chord and short chord profiles.

Some examples of *low lift profiles* are SERI S8XX profiles (S801-S823) (Fig. 6.1a) developed during 80's and 90's [35] [36]. The main advantage of this kind of solution is the containment of the forces acting on the structure in the case of stall controlled wind turbines due to the reduced angle of attack's range of work; in this case, when the turbine operates in off design conditions, the forces acting on the blade, and thus

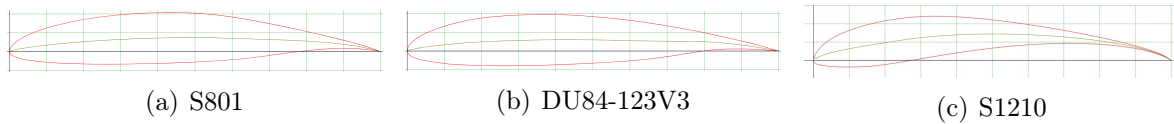


Figure 6.1: Low lift and high lift profiles [2]

on the structure, are contained within relatively small values. This aspect was in contradiction with the theory of airfoil blade: in fact, in the aeronautic sector the goal is to obtain the maximum lift in conditions far enough from the stall conditions to have a safety margin which is necessary to avoid critical issues on the aircraft's handling.

The aim of incorporating *high lift profiles* was to enhance the aerodynamic effectiveness of the blade sections near the hub, specifically in the area referred to as the **root**. In the event of a low lift coefficient in this region, it would be necessary to utilize long chords and significant twist angles, which would entail high expenses and transportation challenges, rendering the project unfeasible. The implementation of high lift profiles assists in reducing the chord length, resulting in streamlined blades with reduced solidity at the root section. Some examples of these profiles are:

- FFA W-XXX - FOI [7], designed by FFA;
- DU XXX-W-XXX [30], designed by Delft University (Fig. 6.1b);
- RISØ A1-XXX, B and P [12] [15], designed by Risø.

6.1 Wing profile choice considerations

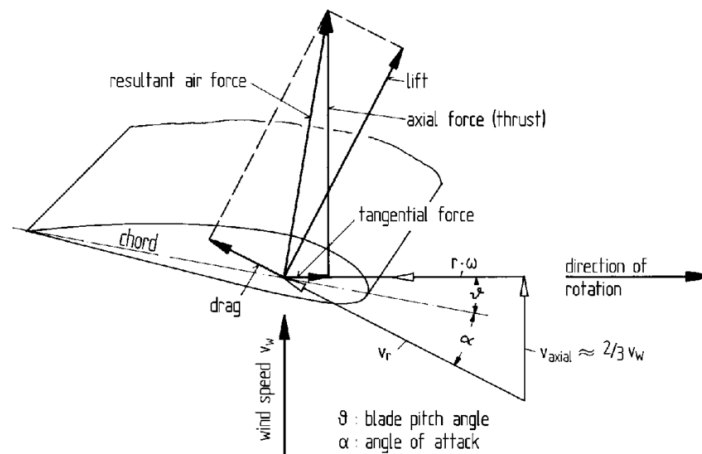


Figure 6.2: Forces acting on the airfoil [20]

Thrust and torque are governed by the terms $c \cdot C_L$ and C_L/C_D ; high values of $c \cdot C_L$ maximize the torque produced and thus the power but at the same time they increase the bending moment. An high value of the efficiency ratio C_L/C_D increases the thrust reducing the torque.

POSITION	PARAMETER	PASSIVE STALL
TIP	high design C_L/C_D	•••
	high off-design C_L/C_D	•••
	slow transition to the stall close to the leading edge	•••
	small fouling sensitivity	•••
	low noise	•••
	Structural resistance	••

POSITION	PARAMETER	PASSIVE STALL
ROOT	high design C_L/C_D	•••
	high off-design C_L/C_D	•
	slow transition to the stall close to the leading edge	•••
	small fouling sensitivity	•
	low noise	○
	Structural resistance	•••

Table 6.1: Characteristics and performances of profiles along the blade.

Legend: importance of the design parameters: ○ null, • little, •• medium, ••• high [6]

Tip section

In the case of stall controlled wind turbines, a high lift coefficient value is good because it helps to reduce chord length and to have lower thrust in strong wind conditions. Airfoil profiles with high value of lift coefficient tend to have a abrupt transition during stall conditions and low lift value in deep stall conditions: this could be really dangerous considering the dynamic stress on the blade.

Root section

In the sections close to the hub, the thickness of the blade is generally higher than the one at the tip. Reduced chord lengths help to limit the weight and to overcome transportation problems; they also reduce the stress on the bearings and on the shaft too. To obtain high lift coefficient in the stall controlled wind turbines, vortex generators are used to increase it up to 1.9 – 2.0, up to 50% of the blade radius. High lift coefficients in the sections close to the hub are important to produce enough torque with low wind speed.

6.1.1 Airfoil profiles for small power WTs

Wind turbines with limited nominal power and small hub diameter typically use high lift profiles due to their ability to maintain a smaller chord length near the hub. This selection helps to mitigate the issue of airfoil wrapping around the hub, which can occur when the wrapping angle exceeds 120° . The overlapping of blade profiles in the root section can result from excessive wrapping, which poses a potential problem.

Blade model

After conducting an analysis of the site where the wind turbine is intended to be installed and evaluating the characteristic wind speeds, it becomes possible to proceed with the design of the blade model.

7.1 Design

7.1.1 MATLAB Software

Prof. PhD Pavesi G. provided us with the MATLAB software to establish the baseline profile of the blade. Essentially, the software uses wind data to assess the wind conditions at the site being analyzed. It then calculates the energy output over the course of the year, allowing us to select the desired cut-in and cut-out velocities to focus better the design for a specific wind speed range. The software also determines the undisturbed velocity and the velocity that results in the highest energy extraction. The blade profile is then evaluated using another component of the software. To carry out this analysis, the necessary inputs include:

- external diameter of the blade, named D_{tip} ;
- hub diameter, D_{hub} ;
- number of blades;
- the chord distribution could be chosen among different models;
- tip losses and hub losses could be chosen among different models;
- the wing profile, or airfoil;

Then, the set-up to generate the output must be done, and the necessary inputs for this section are the following:

- number of sections;
- distribution of the sections, *linear*, *cosine*, *bicosine*;

- maximum iteration number;
- convergence tolerance;

Once all the parameters are set-up, the MATLAB software designs the blade profile.

7.1.2 Baseline blade

The baseline profile in analysis was carried out considering the wind data of **Pianosa**, a small island in the Tuscan Archipelago in the Tyrrhenian Sea, Italy; it's located close to Elba, looking South.

Considering its wind data, the **cut-in** and **cut-out** velocities were fixed respectively at 4 m/s and 14 m/s to guarantee the best possible power coefficient in the wind speed range under our attention. Under these constraints the undisturbed velocity and the nominal one suggested by the software were:

$$\text{Undisturbed velocity, } U_{\infty} = 9.59\text{ m/s} \quad \text{Nominal velocity, } U_{nom} = 10.09\text{ m/s}$$

With these kind of wind turbines, the undisturbed velocity and nominal wind velocity should be revised and changed a little bit; the reason is that, this WTs reach the nominal value of power produced for a wind speed close to the cut-out velocity because then they're stopped when cut-out is reached.

Thus, in this study, the values of **undisturbed** and **nominal** velocity were assumed to be:

$$\text{Undisturbed velocity, } U_{\infty} = 11.00\text{ m/s} \quad \text{Nominal velocity, } U_{nom} = 13.00\text{ m/s}$$

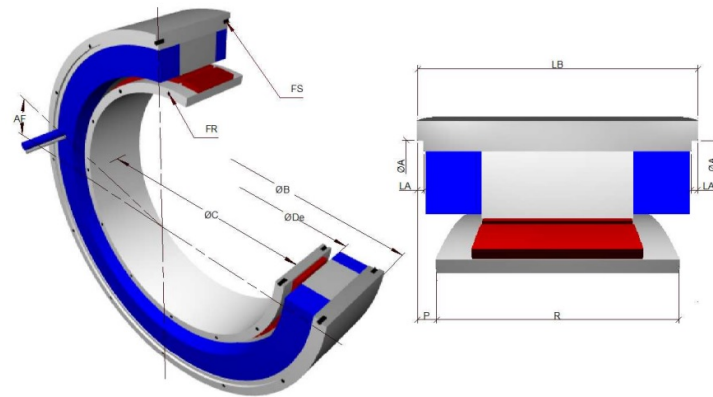
This assumptions also help to increase a little bit the theoretical value of power coefficient of the wind turbine under examination.

Once the nominal and undisturbed velocities have been chosen, the design of the blade has started; first of all, the power of the wind turbine has been fixed, at a value of **1.5 kW**, then the external diameter, D_{tip} , has been fixed at **2.2 m**.

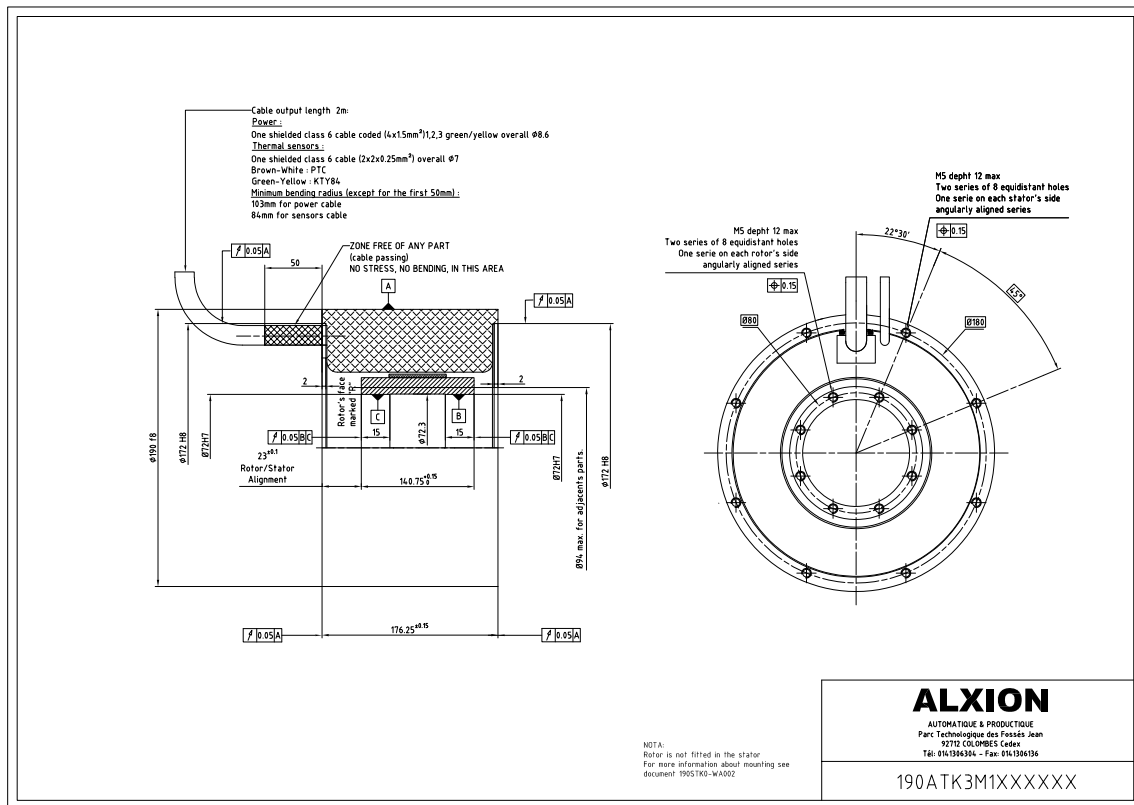
For what concerns the hub diameter the geometrical constraint that limits the diameter, is the external dimension of the electrical generator that must be placed inside the nacelle. To carry out a feasible solution, many products from different companies have been compared, to find the best optimum solution for this goal.

The electric generator chosen was the **ALXION 190STK3M** (Fig. 7.1a, Fig. 7.1b).

ALTERNATORS 190 STK



(a)



(b) Technical drawing

Figure 7.1: Alxion 190STK3M electric generator [4]

The characteristic dimensions of this generator were found in the technical paper sheets provided by the company [4], in particular the **external diameter** of the electric generator is equal to 190 mm. Thus the diameter of the hub was set to 200 mm, just to be sure that the electric generator fits in with no issues.

The **chord distribution** used was the one suggested by Maalawi, the **tip losses**

correction are referred to the model suggested by **Sant**.

7.1.2.1 Tip losses

Neglecting the losses that arise at the blade tip is not possible; they are a consequence of the pressure differential between the upper and lower surfaces of the aerofoil. In general, air particles tend to migrate from regions of high pressure to regions of low pressure. This principle applies to the blade tip and leads to the formation of a vortex that ultimately disperses into the wake. The creation of this vortex at the tip results in reduced power output of the blade due to the accompanying losses.

The angle relative to the wind, number of blades, and position of the blade all affect the correction factor. As the circulation of flow varies from root to tip, the tip-loss correction factor allows us to understand the reduction in forces along the blade. Fig. 7.2 depicts the tip loss factor for a radial blade, illustrating how the correction factor varies from 0 to 1 along the blade. Specifically, a constant factor of 1 is maintained from the blade's root to around 85% of its radius.

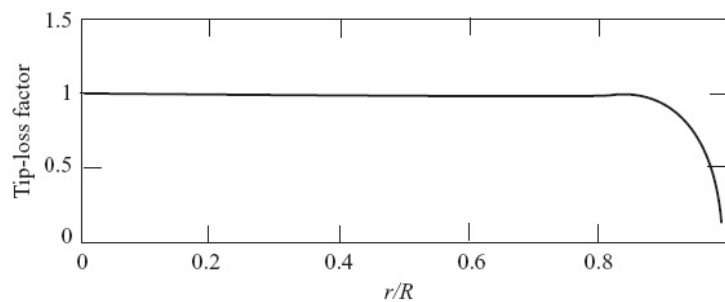


Figure 7.2: Span variation of the tip loss factor

7.1.2.2 Wing profile

Once these parameters were set-up the starting approach to determine the best baseline profile could be conducted. Many different wing profile have been tested:

- E423
- E471
- S1210
- S1223
- S801
- S822
- S823
- SG6043

All these profiles have been tested at different rotational velocity, starting from 450 rpm and decreasing it by 25 rpm step until the maximum value of power produced in a zone enclosed between 70% and 90% of the radius was reached. The value of 450 rpm correspond to a tip-speed ratio of $\lambda = 4.71$ while 250 rpm correspond to a tip-speed

ratio of $\lambda = 2.62$.

Once these parameters were defined, all the simulations have been carried out and then the results have been analysed.

7.1.3 MATLAB software results

These kind of profiles usually work better for a tip speed ratio value around $2.5 \div 4.2$; to find the best value of *lambda*, multiple simulations were conducted at various rotational speeds and their findings are presented herein. The **tip speed ratio** (*TSR*) is defined as:

$$\lambda = \frac{\omega \cdot R}{u_{und}} \quad (7.1)$$

where R is the radius of the blade and u_{und} is the undisturbed velocity of the wind.

The output files contained plots that depicted the torque generated in each section. By multiplying the torque by the rotational speed, it was possible to calculate the power produced in each section.

As known from the theory it's better to optimize the aerodynamic behaviour of the profiles in the sections included between the 70% and the 90% of the blade radius, because the sections close to the hub must be more structural optimized.

In the plots obtained a general trend could be seen:

- as the rotational speed decreases, the power produced by the sections close to the tip slightly increases;
- as the rotational speed decreased, the power produced by the sections close to the root slightly decreases;
- once the rotational speed decreases below a certain value, the power generated by all the sections of the blade falls down abruptly.

The value of rotational speed that optimize the power produced in the sections previously mentioned, has been taken as **nominal rotational speed**.

To expedite the computations required for this initial assessment, it may be prudent to utilize between 7 to 10 sections, while for the final geometry is suggested to use at least 30 sections to obtain a more accurate blade profile.

Once the wind speeds, rotational speed, airfoil profile, chord distribution, tip losses and diameters have been precisely evaluated, the final and more accurate blade model could be built up.

7.1.4 3D model

Analysing all the solutions and comparing the best data obtained among themselves, the best profile has the following characteristics:

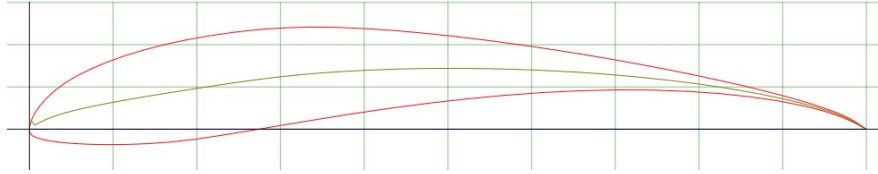


Figure 7.3: S1210 airfoil profile [2]

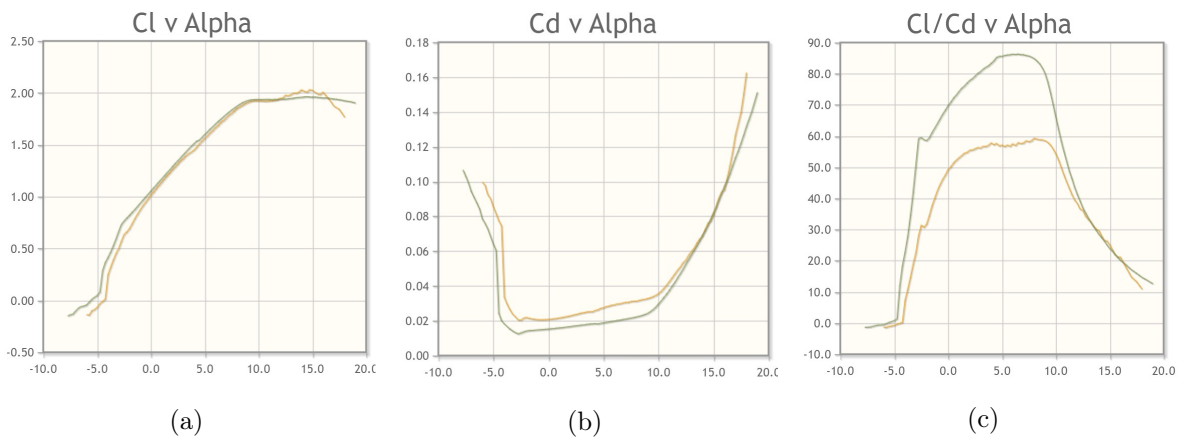


Figure 7.4: Characteristic parameters¹ of S1210 profile [2]

REFERENCE BLADE	
Airfoil profile	S1210
Nominal rpm	325 rpm
λ	3.40
Cut-in velocity	4 m/s
Cut-out velocity	14 m/s
Undisturbed velocity	11 m/s
Nominal velocity	13 m/s
Tip diameter	2.20 m
Hub diameter	0.20 m
Nominal power	1.5 kW

Table 7.1: Reference blade design characteristics

¹The coefficients evaluated at $Re = 200000$ were plotted in green; The coefficient evaluated at $Re = 150000$ were plotted in yellow.

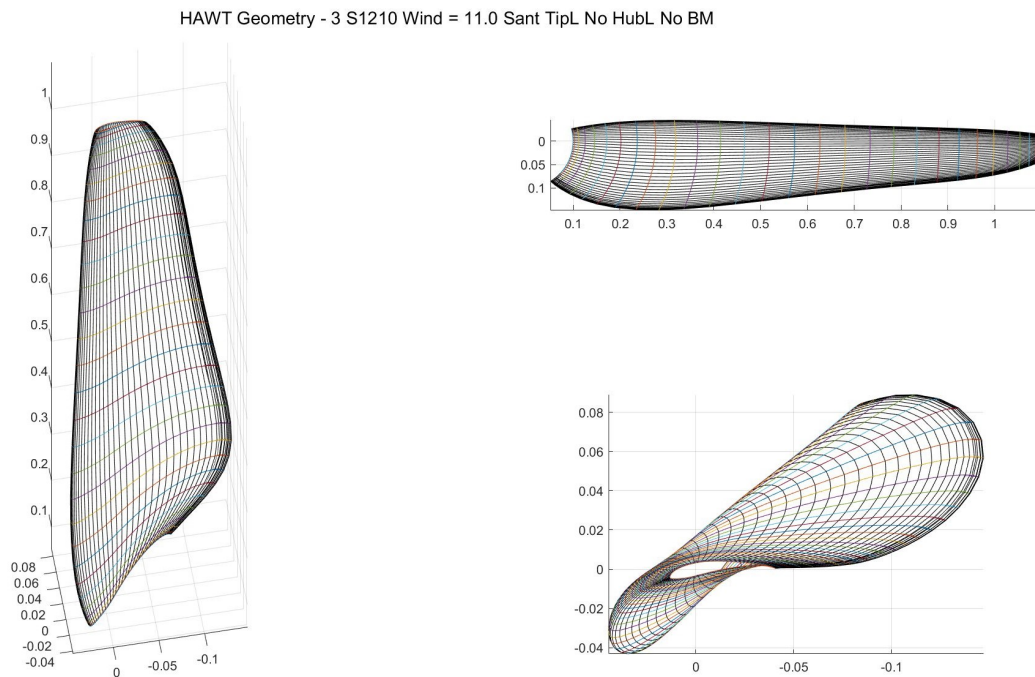


Figure 7.5: Reference blade model

7.1.5 SolidEdge models

7.1.5.1 Blade

After conducting the simulation, an output in the form of a SolidEdge file is generated. This file comprises all the assessed sections, including the leading and trailing edges. It's sufficient to create a surface that links all the profiles, being sure that leading and trailing edge profiles are used as constraints to force the shape of this surface.

By linking the newly created surface with the top and bottom surfaces², it becomes possible to obtain the solid component of the blade, as illustrated in the accompanying figures.

²Top and bottom surfaces are created in the same way as main surface but using only the tip and root profiles.

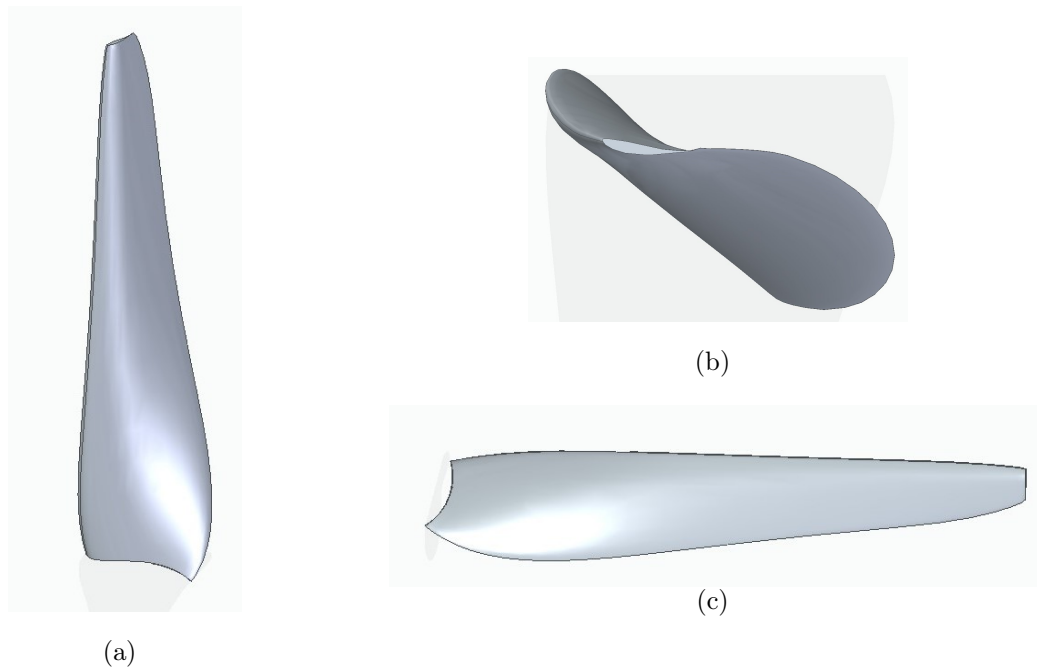


Figure 7.6: 3D SolidEdge model

7.1.5.2 Hub

The hub (Fig. 7.7) has been modelled considering a cylinder with the diameter equal to the hub diameter of the blade, coupled with two ellipsis one in the front and one at the back. The presence of the ellipsis is to avoid flat surfaces in direct contact with the free stream of air (the ellipse in the *front*) and to reduce the losses due to sharp edges (the one at the *back*).

The dimensions of the ellipsis are reported in Table 7.2:

UPSTREAM ELLIPSE		DOWNSTREAM ELLIPSE	
Major axis diameter	260 mm	Major axis diameter	300 mm
Minor axis	200 mm	Minor axis	200 mm

Table 7.2: Characteristic dimensions of the hub ellipsis

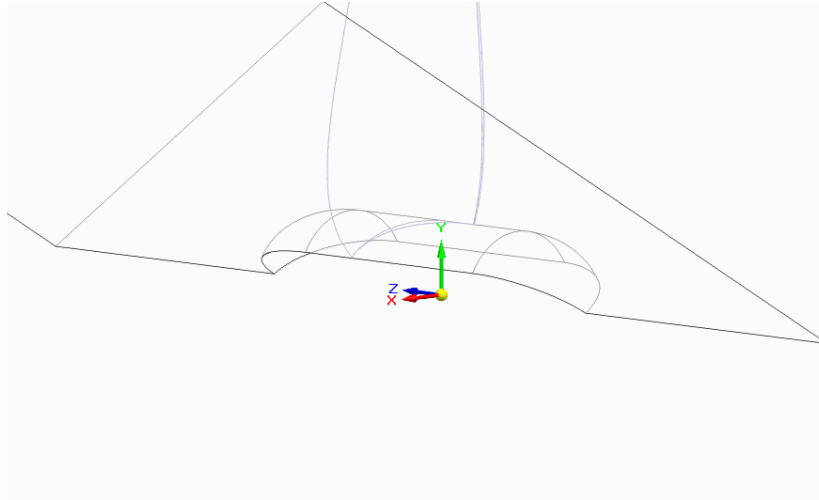


Figure 7.7: Hub

7.1.6 Control volume models

To analyse the behaviour of the blade, two different control volumes have been created: the first one has smaller dimensions and it's formed by an **unstructured mesh**³; the second one is larger and it contains all the air volume and it has been discretized by a **structured mesh**.

The main advantages with these configurations are the better precision in the zone close to the blade and the easier computational requirement needed by the structured mesh for the large volume. The dimensions of the two control volumes are related to the external diameter of the blade; thus, in these cases the control volumes have the following dimensions:

SMALL VOLUME		BIG VOLUME	
External radius	1.65 m	External radius	16.5 m
Depth ⁴	1.50 m	Depth ⁵ (upstream)	16.5 m
		Depth ⁵ (downstream)	33.0 m

Table 7.3: Control volumes dimensions

Here have been reported the schematic draw of the volumes (Fig. 7.9) and the mesh related (Fig. 7.8):

³The unstructured mesh is formed by tetrahedra displaced in a casual way, with no geometrical disposition. More details available in section 8.3.

⁴The extrusion of this volume is **symmetrical**, thus the volume is extruded 0.75 m to the upstream and 0.75 m downstream.

⁵The extrusion of this volume **isn't symmetrical**, because the effects downstream stand for much longer compared to the effects upstream; thus a longer control volume is needed.

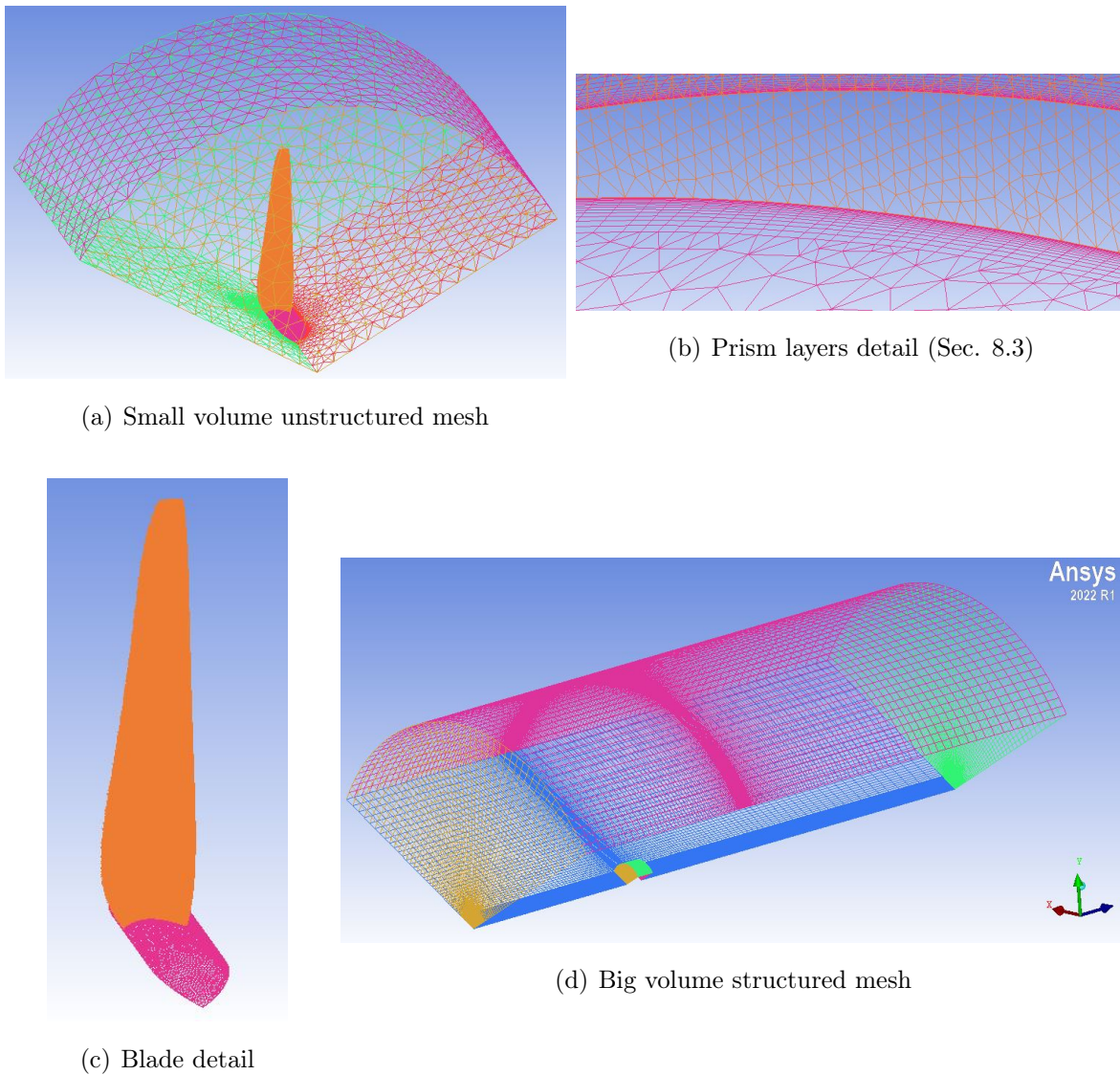


Figure 7.8: Control volume meshes⁶

Control volume mesh To obtain the mesh for the small volume, a simple unstructured mesh was generated in Ansys ICEM CFD. The dimensions of the tetrahedra were selected based on the requirement that only the region close to the blade required small components, whereas the fluid region away from the blade did not. Therefore, a standard dimension was established, but different and more thicker scales were used for the blade and hub surfaces.

⁶In the zone of the mesh corresponding to the pocket, the density of the mesh is higher compared to the remaining part of it; the reason is to have a better accuracy in a zone where the flow becomes more unsteady without increasing too much the overall density of the mesh and thus the computational requirements.

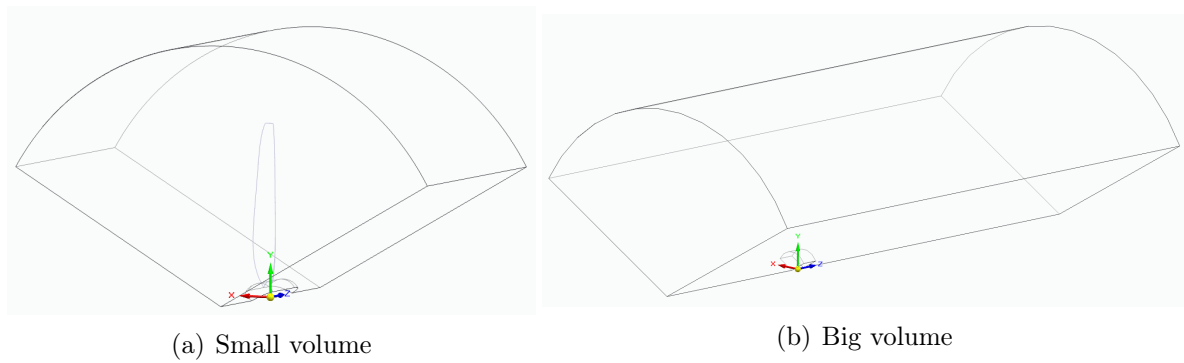


Figure 7.9: Control volumes

For the large volume mesh, a different approach was used. As it was a structured mesh, a block was created to encompass the entire volume. Afterwards, each vertex and line was associated with the corresponding point and curve in the geometry model. As depicted before, the zone close to the pocket has higher density to perform a more accurate simulation.

Pocket A pocket has been fashioned within the greater volume to accommodate the smaller volume, with the pocket's dimensions mirroring those of the small volume.

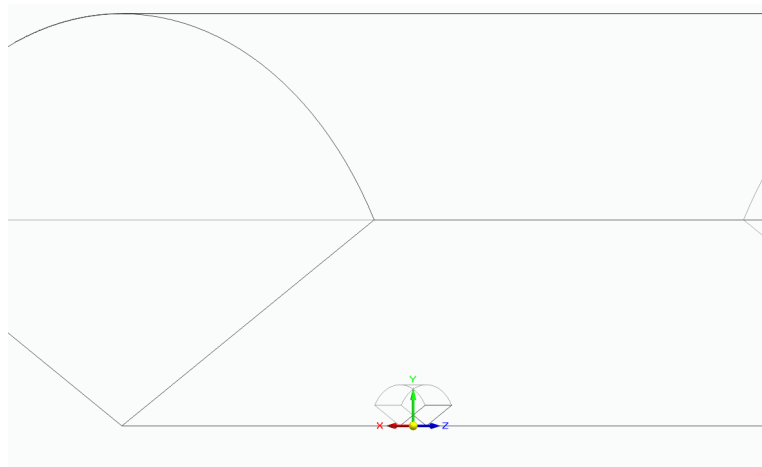


Figure 7.10: Pocket inside the big volume

Frozen rotor The two volumes have been connected inside the CFX solver by using a **frozen rotor** connection; the ANSYS CFX frozen rotor connection technique is employed to model the unchanging flow characteristics of rotating machines. This involves partitioning the fluid domain into stationary and rotating sub-domains, with the interface between them designated as a frozen rotor interface.

To establish a frozen rotor simulation with ANSYS CFX, specific procedures must be followed. The initial step is to divide the fluid domain into stationary and rotating sub-domains using a sliding mesh mechanism. The frozen rotor interface is then declared as the interface between the sub-domains, with the rotor movement being halted and the fluid allowed to flow through it. Identical velocities and angular velocities are assigned to both the rotor and fluid to ensure constant relative velocity.

Next, boundary conditions are imposed on each sub-domain, with blade profiles and inlet/outlet conditions defined for the rotating sub-domain and wall boundary conditions for the stationary sub-domain. The solution process is then repeated until a converged outcome is achieved.

By utilizing the frozen rotor connection approach, it becomes possible to simulate the fluid's actions in a rotating device without requiring a complete simulation of the rotational cylinder. This effectively decreases both the intricacy of the model and the amount of time required for computation.

The observation has been made that the control volumes are fashioned solely with a 120° angle and disregarding the full rotation. This is mainly due to the fact that the wind turbine retains axial symmetry with regards to its axis of rotation, and this design approach considers only 1/3 of the control volume. This aids in reducing the necessary computational requirements, as the diameter is not sufficient enough to accommodate the typical velocity variations of larger wind turbines⁷.

7.1.7 CFX setup

Once the meshed volumes were ready, they've been imported in ANSYS CFX to set up all the parameters and perform the simulation. The **Analysis type** has been set to *Steady state* and here are reported all the main parameters used:

- The inflow surface of the large volume (LV) has been modeled with **Inlet** surface, with air velocity normal to the surface. The value of wind speed changes for each simulation⁸;
- Outflow and top surfaces have been modeled with **Opening** surfaces, with option for mass and momentum corresponding to the *Entrainment* with a value of 1

⁷As previously analysed in the paragraph 3.1.4 and highlighted in the Fig. 3.3, if the diameter of the wind turbine is big, the blade are affected by a different wind velocity when they're at the top compared to when they reach the bottom part of their path.

⁸The baseline profile, and subsequently the modified blade, has been tested at many wind velocities, and thus it must change for each simulation.

bar, pressure option selected to *Opening pressure* and *Zero gradient* for what concerning the turbulence;

- Blade and hub surfaces have been modeled with **Wall** surfaces, considering *No slip wall* and *Smooth surface* options;
- Inclined surfaces have been "*virtually connected*" to create a virtual control volume made by 3 blades and a cylindrical control volume⁹;
- The surfaces acting as interface between LV and SV, have been modeled considering a **Domain interface** interface between them;
- The LV fluid domain has been modeled considering *Air at 25°C, 1 bar* as pressure, *Non buoyancy* and *Stationary*;
- The SV fluid domain has been modeled considering *Air at 25°C, 1 bar* as pressure, *Non buoyancy* and *Rotating* with an angular velocity equal to *325 rpm*;
- For what concern the **Fluid models**, the following assumptions have been made:
 - Heat transfer: None;
 - Turbulence: Shear Stress Transport - Gamma Theta Model¹⁰;
 - Combustion: None;
 - Thermal radiation: None;
- **Analysis type** has been set to **Steady state**;
- **Initialization** conditions have been set up in dedicated page; Cartesian components of velocity equal to what described before, static pressure equal to *1 bar* and *medium intensity* for what concern the turbulence;
- The max number of iteration to reach the convergence has been set to 500.

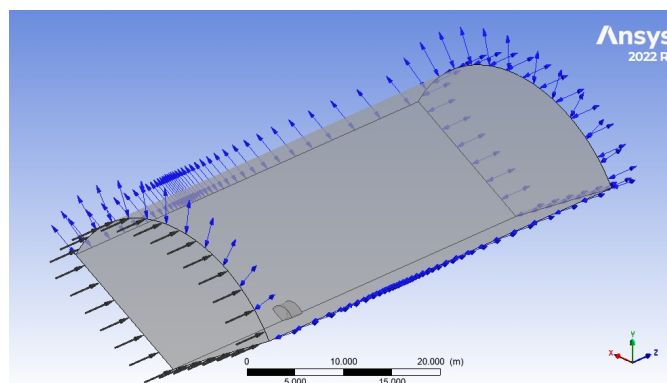


Figure 7.11: CFX-setup

⁹By virtually connect the two surfaces, it is possible to understand the behaviour of 3 blades HAWT simply modelling 1/3 of it; this is what previously mentioned in paragraph 7.1.6.

¹⁰This is the option for what concern the transitional turbulence.

Dimpled section

8.1 Section

To analyse the effect of the dimples on the blade geometry, it's useful to carry out a preliminary analysis using a simplified section of the blade. This analysis has two main aspects: the first one is to find out the best dimple configuration among the possibilities individuated, and the second one is to find out the maximum dimension of the mesh cells that describes in a good way the model.

The baseline geometry has the same airfoil profile of the one of the reference blade (S1210) and a chord length that is an average value of the chord lengths obtained for the sections close to the hub. In particular, a chord length equal to 200 *mm* has been used to create the models.

The thickness of the section considered has been kept fix at 180*mm*, because it was sufficient to carry out the simulations in a way useful to achieve all the goals previously fixed. By keeping constant the thickness of the section and increasing the diameter of the dimples, and thus the spacing between them, the number of dimples in the section is decreasing from case 1) to case 2), but this was done to have a better comparability between the various simulations.

8.2 Dimple choice

8.2.1 Prior investigations

Many studies have been carried out during the years to find the best optimum geometry regarding to the profile under examination; here some have been reported.

D'Alessandro V., et al.

In 2018, D'Alessandro V., et al. [11] suggested to use a NACA profile, in particular the NACA 642-014A with the following dimple geometry (as also shown in Fig. 8.1):

- spherical dimple;
- $\varnothing_{dimple} = 4.7\%$ chord length;
- depth=0.705% chord length;
- position along the chord = 55% chord length;
- 1 row of dimples
- spacing between the dimples: around 1 diameter.

The chord length of the wing was 0.45 m and the span was 1.4 m respectively.

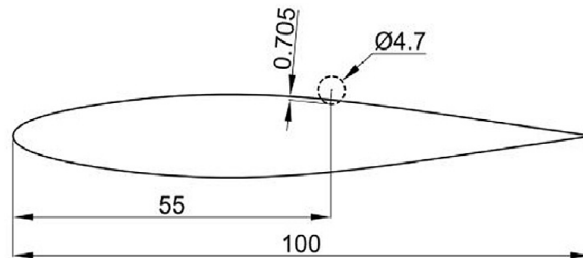


Figure 8.1: Dimples geometric configuration [11]

Results In this paper, dimples effect on NACA 642-014A airfoil was investigated. In particular, the dimples impact on the reduction of the laminar separation bubble extension and on the boundary layer development was faced. LES computations based on a low-dissipative solution algorithm were carried out and, for the sake of their validation, experimental measurements were also conducted. It has been shown that dimples application produces a reduction of the laminar separation bubble extension if the dimples are placed before or inside the LSB. On the other hand, if the dimples are positioned after the bubble, they affect the development of the reattached turbulent boundary layer. In all the considered cases we have observed a reduction of the $c_{d,p}$ (drag coefficient due to pressure field) with a consequent increase of the $c_{d,v}$ (drag coefficient due to viscous stresses) and we have justified this evidence through a boundary layer analysis. However the first effect prevails on the second one producing an overall c_d (drag coefficient) increase for two of three cases considered in this work. On the other hand lift coefficient obtains contrasting beneficial from the dimpling technique. Therefore the application of the dimples, on the airfoil treated in this work, can be considered critical since its effect is strongly related to the angle of attack [11].

Sedinghi H., Akbarzadeh P. and Salavatipour A.

Another simulation was carried out by Sedinghi H., Akbarzadeh P. and Salavatipour A. in 2019 [31]: in this study, the effect of dimpled surface blade on the performance of V47-660 kW horizontal axis wind turbine was numerically investigated. For this purpose, they opted for the following dimples geometry (also shown in Fig. 8.2) positioned on the suction side of the airfoil:

- $\varnothing_{dimple} = 30, 50, 100, 140 \text{ mm}$;
- depth = half of the radius;
- spacing between the dimples: 150, 200, 300, 400 mm;
- 3 rows of dimples: one positioned at 20% of the chord, one at 40% and the last one at 60%;
- dimples located between the radius $R_1 = 4508.45 \text{ mm}$ and $R_2 = 1450.43 \text{ mm}$, that considering the overall radius of the blade equal to 23.5 m states that the dimples are located between the 19.1% and the 61.7% of the blade radius.

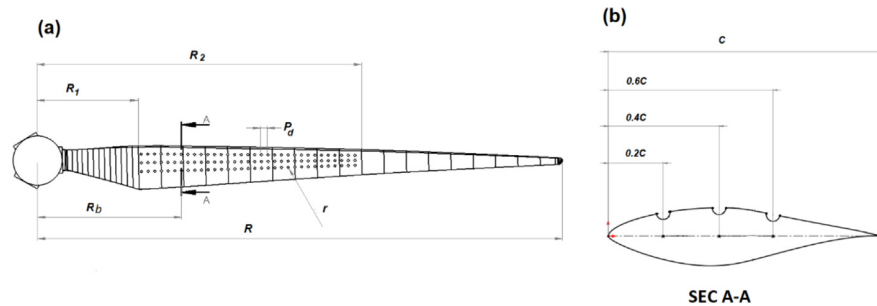


Figure 8.2: (a) Two-dimensional view of a dimpled blade; (b) Sketch of dimpled airfoil (cross-section A-A) [31]

Before starting the discussion about the results they achieved on the performance of the wind turbine, must be mentioned that they evaluated the behaviour of the dimpled surface on a two dimensional airfoil, the NREL's S809, which was almost similar to the airfoil of the V47-660 kW wind turbine and in particular the lift coefficient C_l . The results they found show that the dimples could delay the separation phenomena (or increase the stall angle) and also could increase the lift coefficient at high angle of attacks (i.e. greater than 15 degrees).

Results The results show that by decreasing the dimple radius, the generated torque increases remarkably. It means that when the dimple radius is 70 mm or 50 mm, the torque is less than the original blades (no-dimple blades) while when the radius is

selected as 25 *mm* or 15 *mm*, the generated torque can be greater than the original wind turbine. For example, for the case of $r = 25 \text{ mm}$ and $P_d = 200 \text{ mm}$ (which is the best condition for the rated wind speed), the torque obtained by the simulation is around 255.13 *kNm* while the torque obtained by the simulation for the original blades (no-dimple blades) is around 247.2 *kNm* [31].

Fikade et al.

As previously mentioned in the section 2.3.1, Fikade et al. [14] aimed to investigate the impact of different dimple geometries, particularly focusing on inward and outward positioning. The results that must be emphasized were:

- As the attack angle increased from 0° to 12° , flow separation occur at plain surface model.
- As the attack angle increased from 12° to 14° clear flow separation appeared on the upper surface.
- At angle of attack 12° flow remain attached with the upper surface in case of dimpled surface.
- At 16° angle of attack the flow is separated from the upper surface in case of dimpled surface.
- Both inward and outward dimpled airfoils generate more lift than a plain airfoil configuration at corresponding angles of attack.
- Both inward and outward dimpled models exhibit a uniform increase in lift across all angles of attack considered in the study.
- Both inward and outward dimpled airfoils show a decrease in drag compared to the plain airfoil model.
- The outward configuration exhibits the least amount of drag.
- The angle of stall also increased in the case of the dimpled airfoil.

8.2.2 Present study

In this study some geometries want to be analysed; in particular, among all the possible solutions constituted by variation of diameter, variation of depth, variations of spacing between the dimples and the position along the chord, this study wants to focus on the diameter variation and position along the chord.

An aspect that must be emphasized is that the spacing between 2 consecutive dimples is referred to the diameter of the dimples, so varying the diameter it varies also the spacing in absolute terms, but the relative position is the same.

All the configurations have been tested in 4° , 8° , 12° and 16° angle of attack (AoA) to understand the behaviour of the different configurations varying the relative angle of wind incidence.

In Table 8.1 are listed all the configurations tested, with the specifications for each case and the 3D models used are reported in the following figures (Fig. 8.3):

DIMPLE SPECIFICATIONS				
	Diameter	Depth	Space between 2 dimples	Position along the chord
1)	$5.0\% \cdot c$	$0.9\% \cdot c$	$1.8 \cdot D$	$20\% \cdot c$
2)	$5.8\% \cdot c$			$30\% \cdot c$
3)	$5.0\% \cdot c$			$45\% \cdot c$
4)				$60\% \cdot c$
5)				

Table 8.1: Dimple specifications. c is the chord length, D is the diameter of the dimple

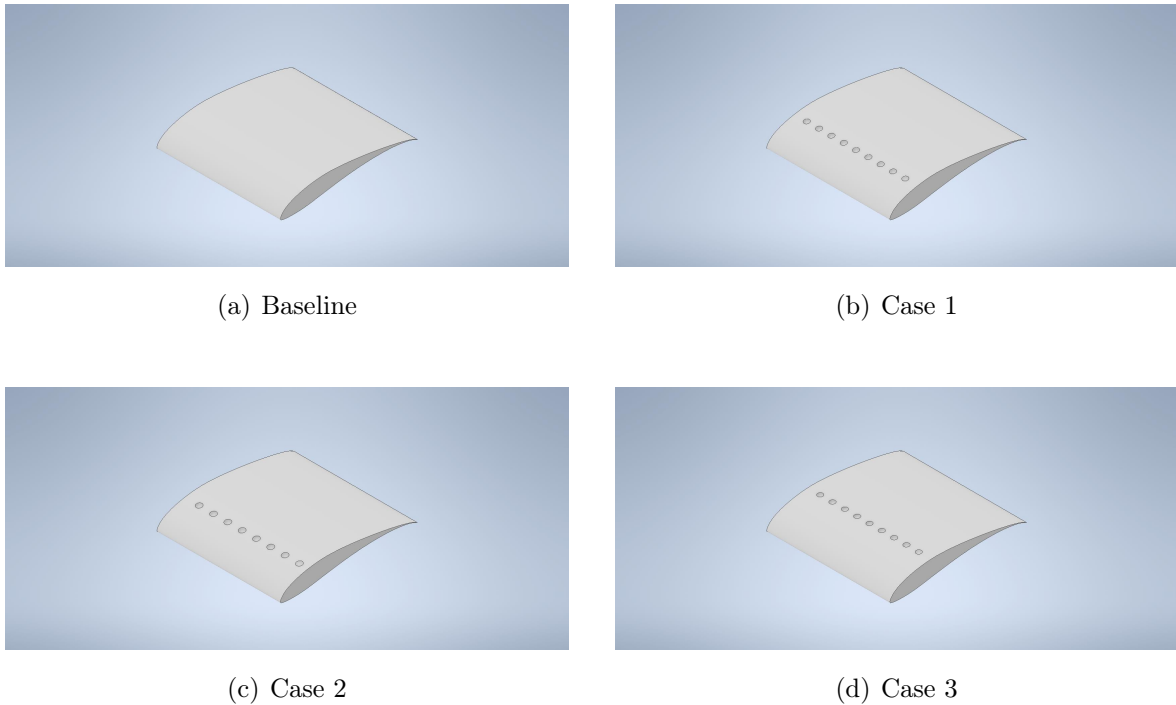


Figure 8.3: Dimple specification sections obtained with Autodesk Inventor



Figure 8.3: Dimple specification sections obtained with Autodesk Inventor (continued)

8.3 Ansys mesh

In order to discretize the dimpled section's behavior, it is necessary to establish a defined control volume. To conduct an Ansys CFX simulation, a fluid volume encompassing the airfoil section is required. This control volume has been generated in SolidEdge, resulting in a solid object with specified dimensions (Fig. 8.4):

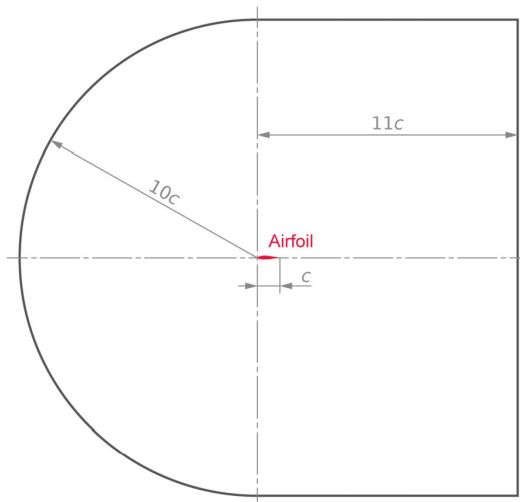


Figure 8.4: Control volume dimensions

The depth of the control volume has been fixed at a value of **180 mm** equal to the thickness of the sections obtained with Autodesk Inventor. This has been done considering that no tip effects must be considered when this sections are analysed because they're not close to the tip of the blade.

Since the simulations have been carried out at different angle of attack, the control volume have been rotated along z-axis with the corrspeing angle of attack.

Mesh The mesh generated is an **unstructured mesh**, which is formed by tetrahedra displaced in a casual way, with no geometrical disposition. The main advantages of the unstructured mesh are:

- Flexibility: greater flexibility in modeling complex geometries and shapes, including free-form surfaces, curved edges, and varying shapes;
- Reduced computational time and resources: they can adapt to changes in geometry or local refinement requirements, reducing the number of mesh elements needed;
- Better accuracy: unstructured meshing can provide better accuracy in simulations due to its ability to adapt to local requirements;
- Easy to generate: is easier to generate compared to structured meshing.

The dimensions of the tetrahedra have been selected to be enough small to well describe the geometry of the dimples. In the following pictures, a detail of dimples and airfoil mesh are presented.

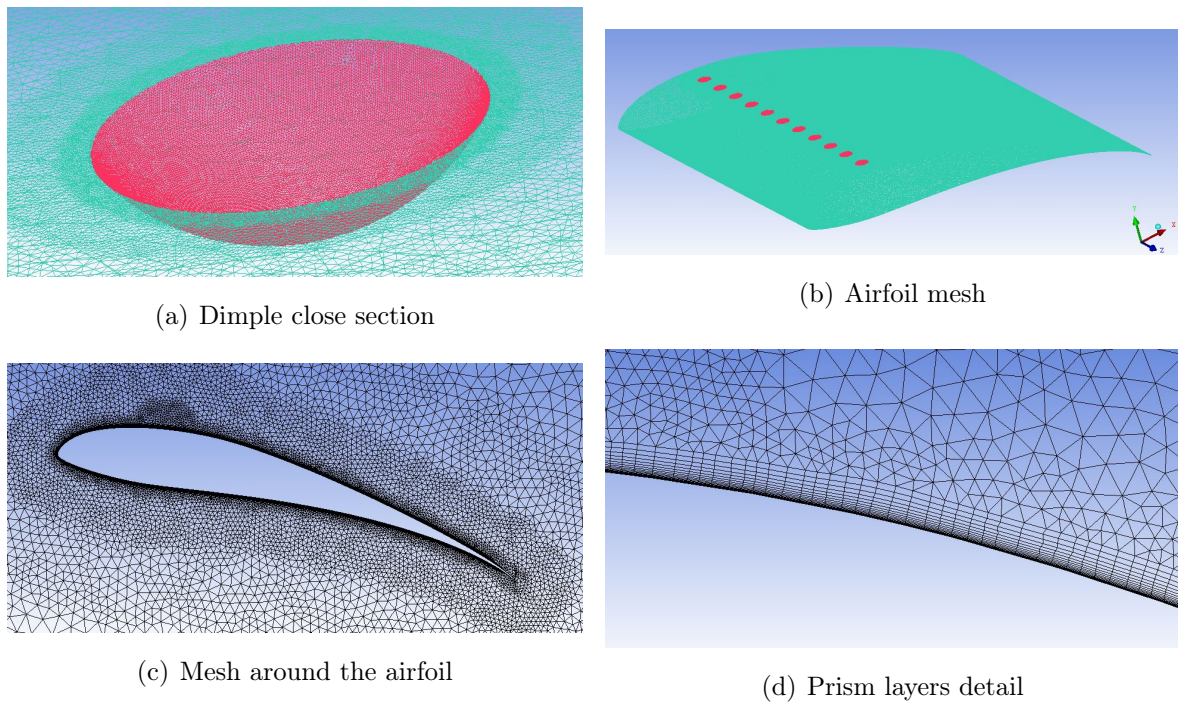
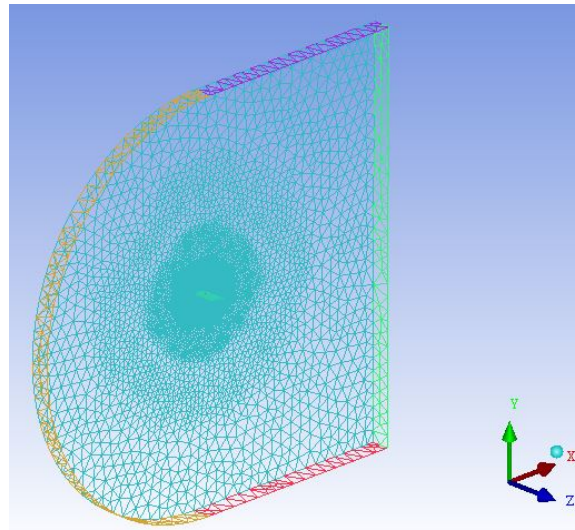


Figure 8.5: Mesh details



(e) Control volume mesh

Figure 8.5: Mesh details (continued)

Prism layers¹ Close to the airfoil surface, a different kind of mesh has been discretized: in this section, **prism layers** have been created to improve the accuracy and the stability of the solution. Prism layers, also known as boundary layer meshes, are a type of mesh element commonly used in CFD simulations to capture the boundary layer near solid surfaces.

Prism layers are typically composed of a series of wedge-shaped elements that conform to the shape of the solid surface. These elements are typically smaller near the surface and increase in height as they move away from the surface. The prism layer mesh is typically generated using a special algorithm that ensures that the elements conform to the surface geometry and that the prism layer thickness is consistent throughout the mesh.

Considering the Fig. 1.2 is evident that the gradient of the velocity is normal to the wall; the gradient along the surface of the airfoil $\frac{\partial v}{\partial x}$ is much smaller than the gradient in the normal direction $\frac{\partial v}{\partial y}$; thus to resolve with a good accuracy these gradients, the cells need to be smaller normal to the wall than along the wall (Fig. 8.6).

¹Prism layers have been used also in the baseline and modified blade models

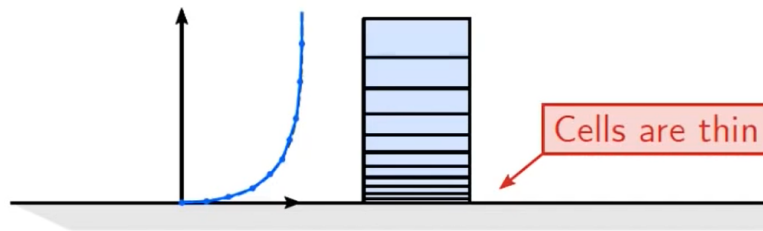


Figure 8.6: Prism layers [1]

Usually the combination of unstructured mesh and prism layers are good both to guarantee the needed precision and the computational simplicity (Fig. 8.7).

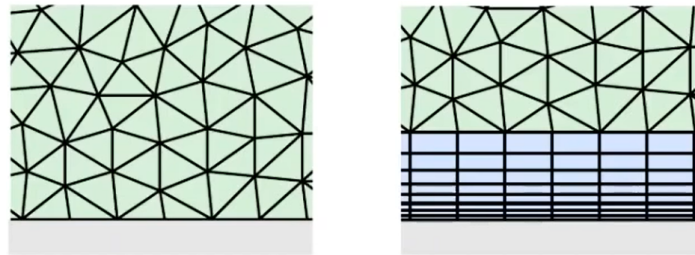


Figure 8.7: Unstructured mesh and prism layers [1]

Even if the software generates automatically the prism layers, some parameters needs to be specified:

- Height of first layer y_H ;
- Number of layers N ;
- Geometric growth ratio G .

The **height of first layer** is set to reach a certain value of y^+ : y^+ , also known as **yplus**, is a non-dimensional parameter expressed by Eq. 8.1 that identifies if the mesh generated is able to describe correctly the velocity of the fluid in the laminar sublayer. The accuracy of simulations in computational fluid dynamics (CFD) heavily relies on the significance of the y^+ parameter. This parameter quantifies the ratio between the distance from the first cell center to the wall and the thickness of the viscous sublayer. For precise predictions of skin friction and wall shear stress, it is generally preferred to maintain a y^+ value of approximately 1. Achieving this requires careful mesh refinement near the wall, particularly in areas characterized by high curvature or flow separation. Guaranteeing an appropriate y^+ value within the mesh is indispensable for obtaining reliable and accurate outcomes in CFD simulations.

$$y^+ = \frac{\rho y v_t}{\nu} \quad (8.1)$$

Where ρ is the density of the fluid in $[kg/m^3]$, y is the distance from the wall in $[m]$, v_t is the velocity based on the shear stress at the wall and evaluated with $v_t = \sqrt{\tau_\omega/\rho}$ and ν is the kinematic viscosity of the fluid.

This parameter is generally evaluated in the post process part of the simulation, thus a primarily iteration is carried out and then the results of the y^+ value have been evaluated in CFX-post. If the y^+ value is lower than 1, it means that the boundary layer is well described by the prism layers.

The **number of layers** and **growth ratio** can be evaluated considering the following assumptions; the number of layers could be seen as a geometric series of N-1 layers, and since the goal is to discretize the boundary layer correctly and not require an un-necessary computational stress, the height of the boundary layer is kept equal to the total height of the boundary layer. From various forms on the web, a first guess can be made:

- $N > 10$, if $y^+ \sim 30$
- $N > 25$, if $y^+ \sim 1$

Usually **G** is kept in the interval $1.05 \sim 1.3$ to have a gradual increase in the dimensions of the prism layers.

Once this assumptions have been made, a first simulation can be carried out; once the results are available a check on the y^+ must be made and then the parameters could be eventually changed to achieve a better result.

8.4 CFX setup

The mesh have been then uploaded in CFX; the CFX block allows to simulate different fluid phenomena such as turbulence, thermal convection, mixing, and combustion, providing detailed information on the flow behavior and their effects on the performance of a particular application.

- The inflow and bottom surfaces have been modeled with **Inlet** surfaces that has Cartesian components of velocity equal to $(11;0;0)$ m/s ; The reason why also the bottom surface has been included, is the fact that parametrizing the geometry varying the angle of attack, once the AoA increases the bottom surface becomes an inlet surface..
- Top and outflow surfaces have been modeled with **Opening** surfaces, with a option for mass and momentum corresponding to the *Entrainment* with a value of 1 bar, *pressure option* selected to *Opening pressure* and *Zero gradient* for what concerning the turbulence;

- Airfoil and dimples surfaces have been modeled with **Wall** surface, considering *No slip wall* and *Smooth surface* options;
- Left and right surfaces have been connected creating a "*virtual connection*" to avoid the presence of board effects that usually are present close to the side edges of airfoils;
- The fluid domain has been modeled considering *Air at 25°C*, *1 bar* as pressure, *Non buoyancy* and *Stationary*;
- For what concern the **Fluid models**, the following assumptions have been made:
 - Heat transfer: None;
 - Turbulence: Detached Eddy Simulations - *DES*;
 - Combustion: None;
 - Thermal radiation: None;
- **Analysis type** has been set to *Transient*, with 80 time-steps as maximum value and 0.00001 s as *Time steps* to have a small *Courant number*²; 5 iterations for each timestep have been fixed to reach the convergence.
- **Initialization** conditions have been set up in the dedicated page: Cartesian components of velocity equal to the ones reported before, static pressure equal to *1 bar* and *medium intensity* for what concern the turbulence.

²The Courant number (CFL) is a parameter used in CFD to determine the numerical stability of a solution method used to solve the flow equations. The Courant number is important because it determines how much information can propagate through the grid within a single time step. If the CFL value is too large, information may propagate through more cells than desired, causing numerical instability in the solution. On the other hand, if the CFL value is too small, very small time steps may be required to achieve an accurate solution, making the computation computationally expensive.

Results of simulations

9.1 Dimpled sections

In the post process of the simulations, many aspects have been considered to identify the best solution. Firstly, the lift, drag and moment have been calculated through the section *Expression* present in the part ANSYS CFD-POST; here, the lift has been evaluated by estimating the force on the $y - axis$ on airfoil and dimple section; the same has been done for the calculation of the drag, but in this time $x - axis$ has been considered of course. The force values have been parametrized using the kinetic energy contained in the wind (Eq. 9.1); in this way the characteristic coefficients of the airfoil have been obtained.

$$C_L = \frac{Lift}{\frac{1}{2} \cdot c \cdot B \cdot \rho \cdot v^2} \quad C_D = \frac{Drag}{\frac{1}{2} \cdot c \cdot B \cdot \rho \cdot v^2} \quad (9.1)$$

Where: *Lift* and *Drag* are the forces in $[N]$ evaluated by the software, c is the chord length in $[m]$, B is the airfoil width in $[m]$, ρ is the density of the air in $[kg/m^3]$ and v is the air velocity in $[m/s]$. The results obtained have been reported in the following table (Tab. 9.1) and figures (Fig. 9.1, Fig. 9.2, Fig. 9.3).

AoA	Case	C_L	C_D	$\frac{C_L}{C_D}$
4°	case 1)	1.433	0.024	59.687
	case 2)	1.451	0.024	61.578
	case 3)	1.479	0.023	65.146
	case 4)	1.505	0.021	73.147
	case 5)	1.498	0.022	69.552
8°	case 1)	1.793	0.028	64.169
	case 2)	1.802	0.028	65.440
	case 3)	1.833	0.025	72.934
	case 4)	1.807	0.027	67.803
	case 5)	1.796	0.029	62.571
12°	case 1)	1.888	0.049	38.639
	case 2)	1.897	0.048	39.380
	case 3)	1.894	0.049	38.762
	case 4)	1.852	0.052	35.564
	case 5)	1.818	0.056	32.619
16°	case 1)	1.859	0.097	19.150
	case 2)	1.871	0.097	19.307
	case 3)	1.850	0.099	18.625
	case 4)	1.820	0.110	16.471
	case 5)	1.794	0.133	13.454

Table 9.1: Characteristic coefficients of airfoil in all the cases

	AoA	C_L	C_D	$\frac{C_L}{C_D}$
Baseline	4°	1.490	0.022	69.404
	8°	1.825	0.026	71.551
	12°	1.890	0.049	38.969
	16°	1.863	0.097	19.147

Table 9.2: Characteristic coefficients of baseline airfoil

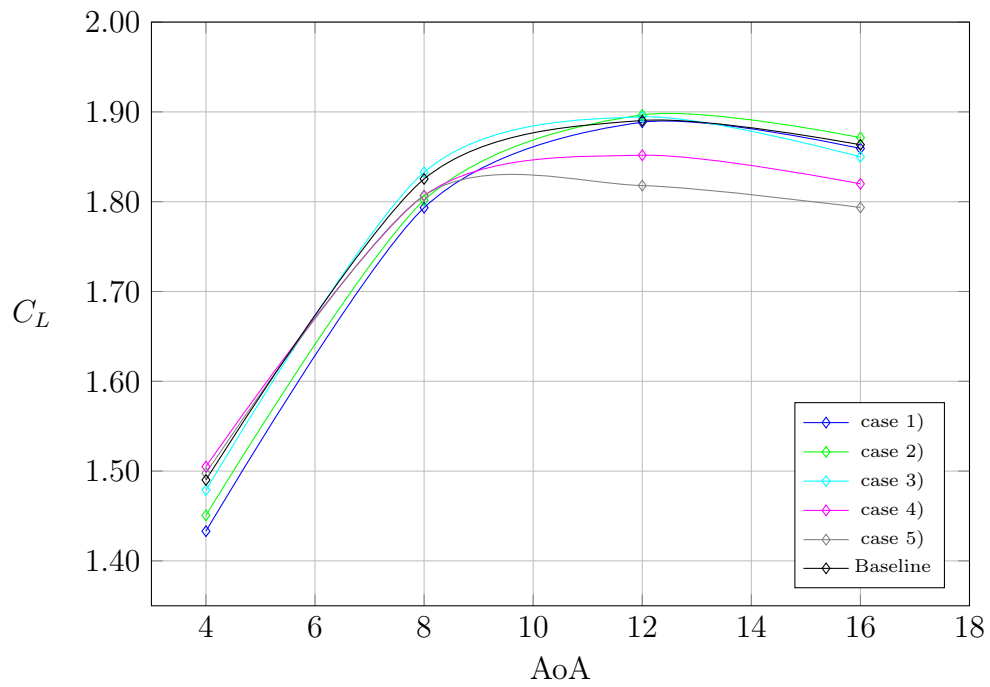


Figure 9.1: Lift coefficient vs AoA

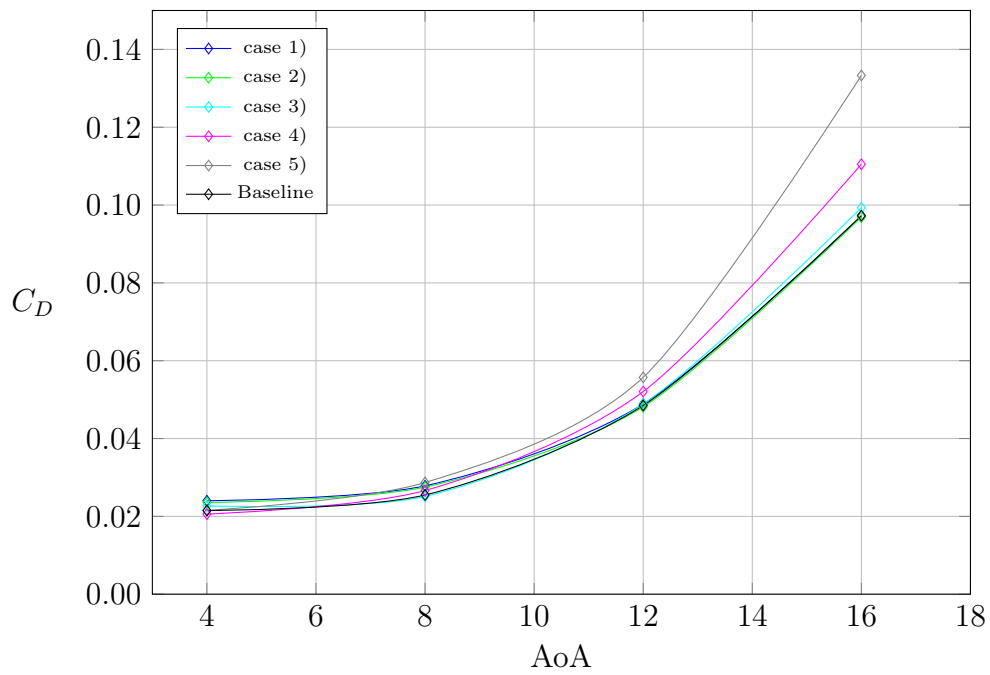


Figure 9.2: Drag coefficient vs AoA

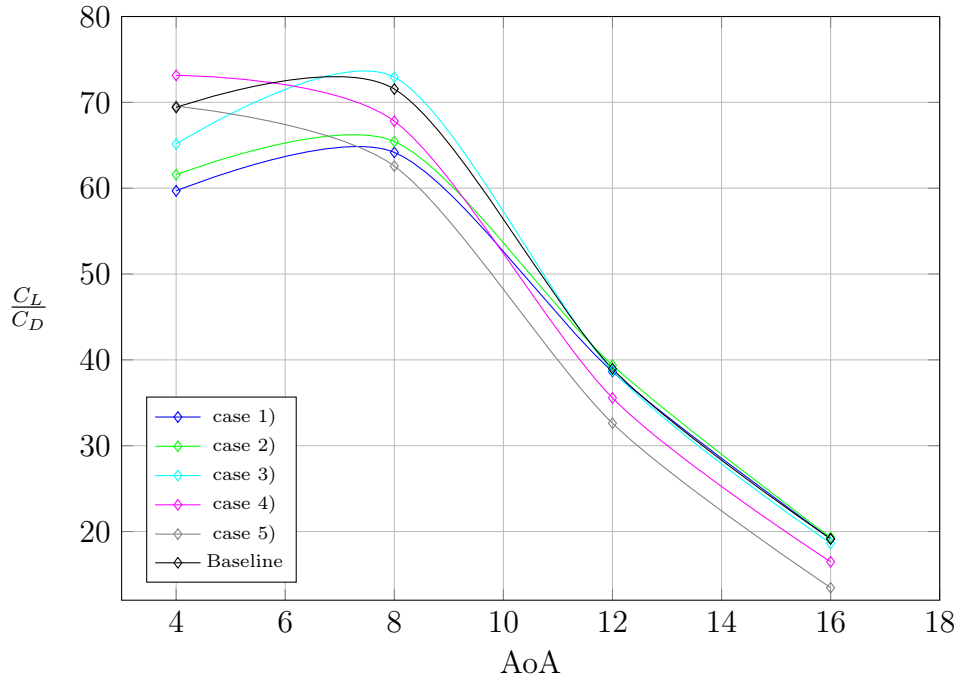


Figure 9.3: Lift/Drag coefficient vs AoA

9.2 Considerations

According to the data presented in Fig. 9.1, Fig. 9.2, Fig. 9.3, the obtained results align with the expectations and findings of previous research conducted by D'Alessandro [11]. These findings indicate that the most favorable outcomes are achieved when the dimples are positioned directly ahead of the boundary separation bubble. This placement effectively energizes the boundary layer, delaying its detachment. By conducting a brief simulation using the *XFOIL* software, it was observed that the boundary layer separation occurs at positions corresponding to 54.5%, 41.6%, 18.8% and 11.2% (percentages referred to chord length c) for angles of attack (AoA) of 4°, 8°, 12°, and 16°, respectively.

Consequently, the most optimal configurations are as follows: **Case 4)** exhibits superior performance at an AoA of approximately 4°, while **Case 3)** proves to be the optimal choice within the range of 6° to 12°. On the other hand, **Case 1)** and **Case 2)** appear to be the preferable options when the AoA exceeds 12°.

Furthermore, when comparing the performance influenced solely by the diameter of the dimples, it is evident that larger diameters yield more favorable effects in terms of lift coefficient and lift-to-drag ratio.

The plots depicting turbulence kinetic energy (Fig. 9.4) clearly demonstrate that the presence of dimples on the surface of the airfoil effectively amplifies the energy within the boundary layer, thereby postponing its detachment.

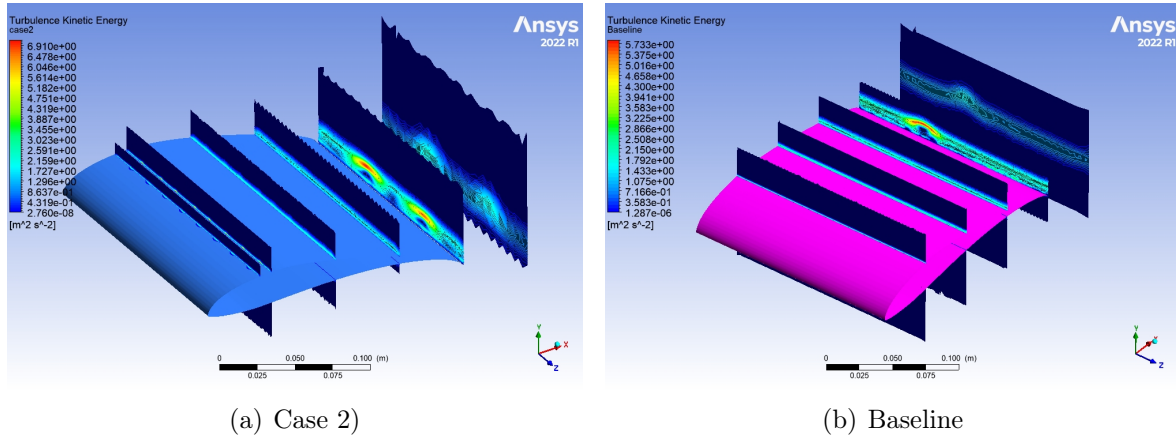


Figure 9.4: Turbulence kinetic energy plots

The recirculation of air in the baseline profile can be observed in Fig. 9.5a, whereas the presence of a dimple influences the stream of air, as depicted in Fig. 9.5b. In Fig. 9.5c a close detail of the recirculation in the dimple could be observed.

Considering that the root section of the wind turbine blade should operate with AoA within the range of 4° - 12° , the best solution appears to be the **Case 3**); the motivations are:

1. In the region of AoA enclosed within 6° and 12° , this solution is the one with higher lift to drag ratio;
2. Even the efficiency for Case 4 is higher in the region with lower AoA, then the lift coefficient drops down in a significant way;
3. The simulations were carried out considering a chord length of 200 mm , which is an average dimension for the sections in the root section; some sections have a chord length slightly greater and thus a relative Reynolds number which has an higher value. As previously mentioned, if the Re number is higher, the boundary layer separation is delayed due to the higher energy contained in the BL.
4. When the wind turbine blade operates at wind speeds near the cut-out velocity, approximately between 13.5 and 14.0 m/s , boundary separation tends to happen before reaching the dimple. However, taking into account the likelihood of encountering wind speeds within this range (which is lower compared to the probability of experiencing lower wind speeds), it becomes evident that positioning

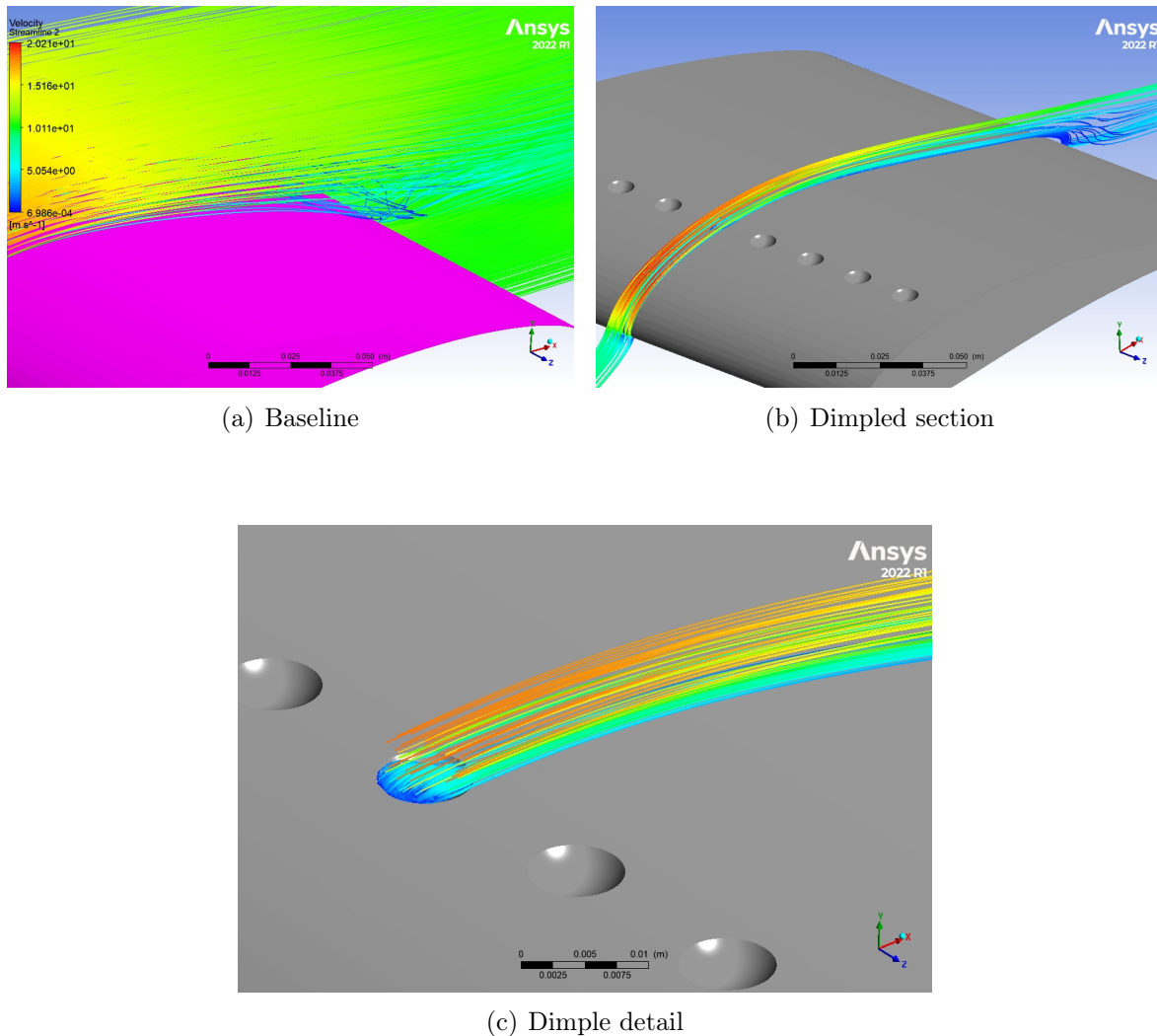


Figure 9.5: Flow streamlines

the dimples slightly further along the chord is more advantageous for optimizing performance at wind speeds around 10 m/s .

5. If the dimples were placed to optimize performance at wind speeds close to the cutoff velocity, the resulting increase in drag when the wind speed is in the range of 4-8 m/s would outweigh the potential benefits that this geometry could offer as the speed increases.

In Fig. 9.6, the y^+ values are visible on the surface of the dimpled airfoil. The obtained values indicate a well-discretized linear velocity gradient path near the wall. In fact, the higher values of Y_{plus} are located on the leading edge, where the velocity close to the surface increases. These values are comparable to those described earlier in Section 8.3, with most of the airfoil surface having values lower than or close to 1. This plot highlights the fact that the mesh, and the prism layers in particular, is well

made.

The utility of prism layers described in the Section 8.3 has clear evidence in this plot (Fig. 9.7). In fact, the velocity profile close to the wall is well described due to the presence of layers close to the surface of airfoil.

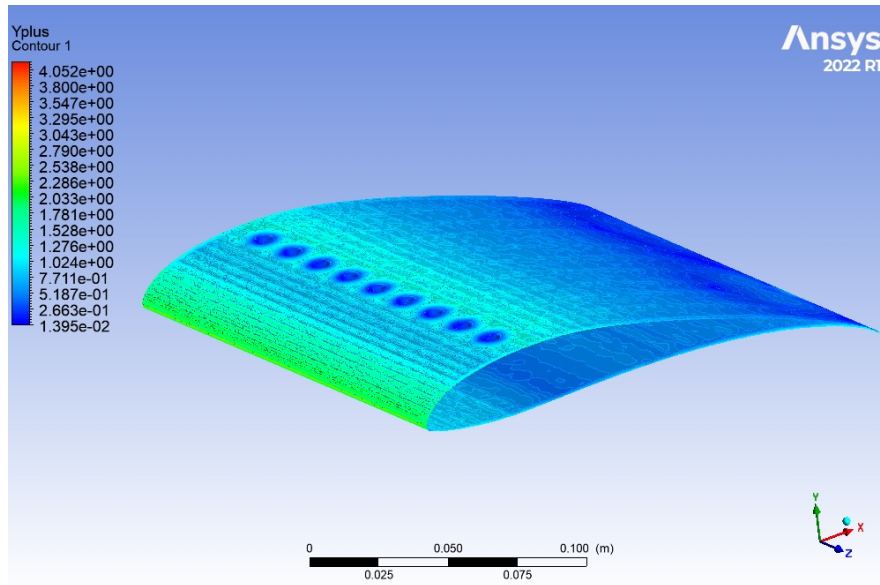


Figure 9.6: y^+ plot

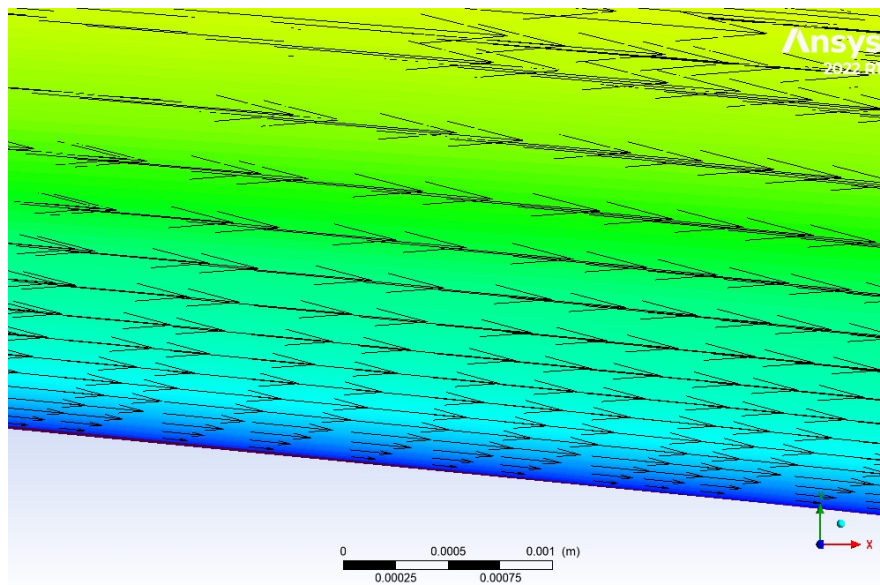


Figure 9.7: Vector plot of velocity near the wall

9.3 Spanwise

Considering scientific papers that have analyzed the behavior of dimpled surfaces or vortex generators applied to blades, an important observation can be made. In all the simulations and studies, these aerodynamic devices were not applied along the entire span of the blade, but rather concentrated in the root section.

This choice is based on the fact that, as mentioned in the section 6.1, this area of the blade is more structurally optimized rather than aerodynamically optimized. Consequently, stall conditions tend to occur first in this region as the angle of attack increases, before propagating to the rest of the blade.

The studies reviewed report the following findings regarding the spanwise positioning of the devices:

- According to Sedighi et al. [31], the series of dimples were positioned within the range of 19.02% to 61.7% of the total blade radius;
- Zhao et al. [40] found that the best location for vortex generators (VG) was between 20% and 70% of the blade radius;
- Jiang et al. [19] observed that the main energy capture occurred when the aerodynamic devices were positioned between 20% and 50% of the blade radius;
- Manolesos et al. [22] positioned vortex generators from 15% to 40% of the blade radius.

If the aerodynamic devices are positioned near the tip of the blade, their contribution to energizing the laminar boundary layer and inducing turbulence is not significant. However, they do introduce a noticeable amount of drag, which negatively affects the airfoil's efficiency.

On the other hand, if the devices are positioned too close to the hub, they are affected by the wall effects present in that region, which can hinder their effectiveness.

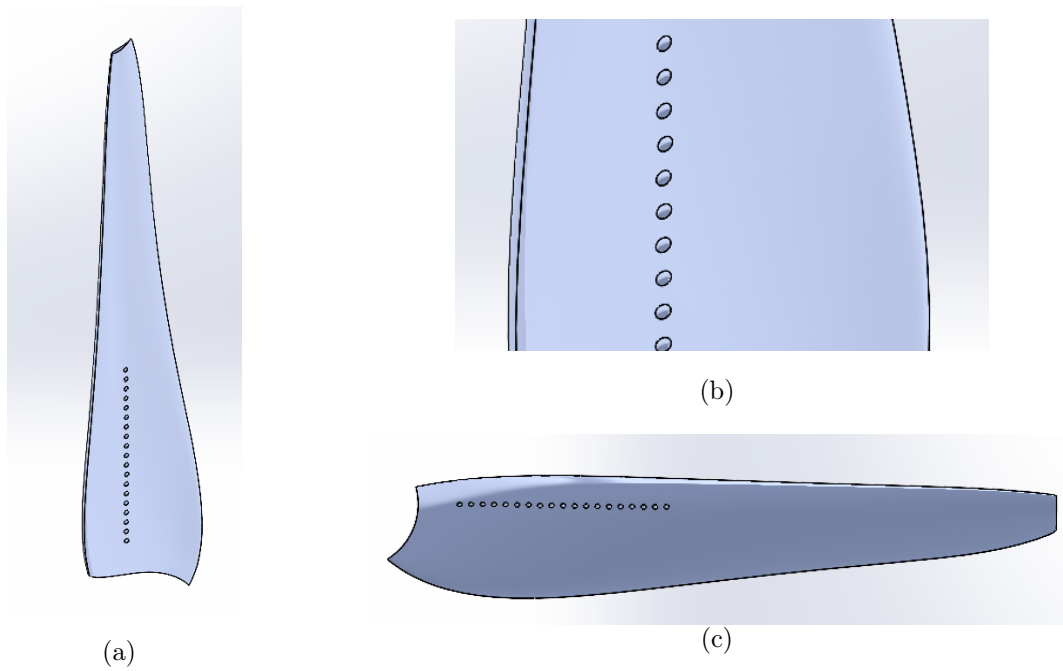
Present study In this study, the aerodynamic devices have been strategically placed between 15% and 45% of the blade radius, corresponding to a linear distance ranging from 165 *mm* to 490 *mm*. This specific positioning was chosen because the dimple geometries were tested under specific conditions: a chord length of 200 *mm* and a Reynolds number close to 150,000. Placing the aerodynamic devices closer to the tip or hub of the wind turbine would render the analysis of the dimple geometries unreliable and unsatisfactory.

Dimpled blade model

10.1 Design

The design of the dimpled blade model obviously started from the baseline model. It has been modified using the *SOLIDWORKS* software; the changes made are of course related to the implementation of dimples in the ways described in the previous sections, Sec. 9.2 and Sec. 9.3; in particular the dimples created on the surface of the blade have a diameter of $5.0\% \cdot c$, a spacing between themselves of $1.8 \cdot D$, and a spanwise along the blade from to 15% up to 45% (or from 165 mm up to 495 mm).

As previously mentioned, the selection of this particular dimple geometry was made with the intention of optimizing its performance in conditions where there is a wind speed around 10 m/s . Therefore, it is more advantageous to utilize the configuration at its maximum efficiency in this range. For what concern the spanwise, as mentioned before, the dimples have been positioned considering the validity of the tests carried out, thus the chord length should be around 200 mm and Re number should be around $150000 - 200000$.



10.1.1 Small volume domain

After that, the small volume domain has been recreated, considering the same size of the one described in Sec. 7.1.6, but using the new blade model. The schematic draw of the volume is reported in the Fig. 10.1

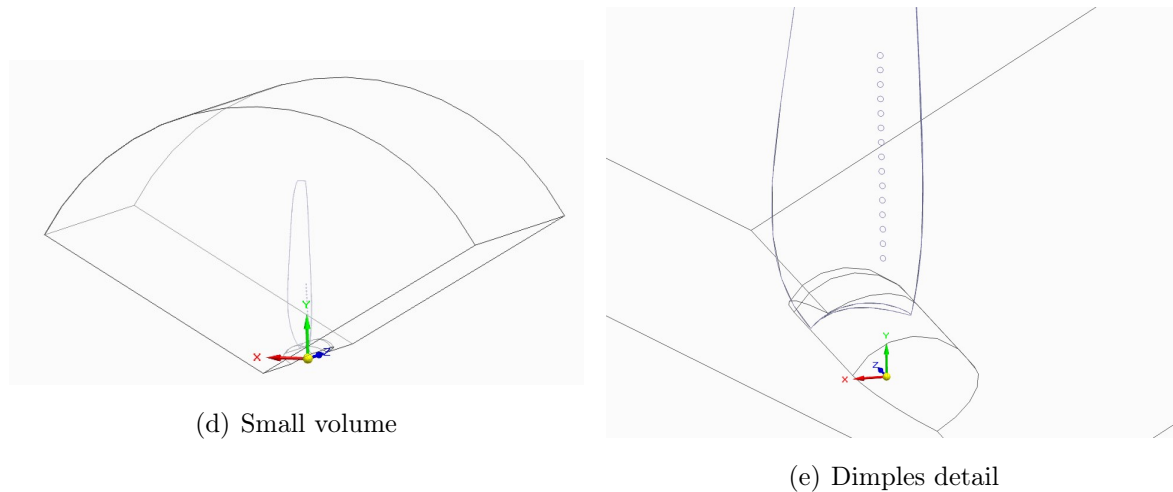


Figure 10.1: Small volume domain with dimpled blade

10.1.2 Control volume mesh

In order to generate the mesh for the small volume, a straightforward unstructured mesh was created using Ansys ICEM CFD. The size of the tetrahedra was determined

with the specific objective of having smaller elements solely in the vicinity of the blade, while the fluid region farther from the blade did not necessitate such fine components. As a result, a standard dimension was set, but varying and thicker scales were employed for the surfaces of the blade, hub and dimples.

The mesh related to the small volume domain is reported in Fig. 10.2.

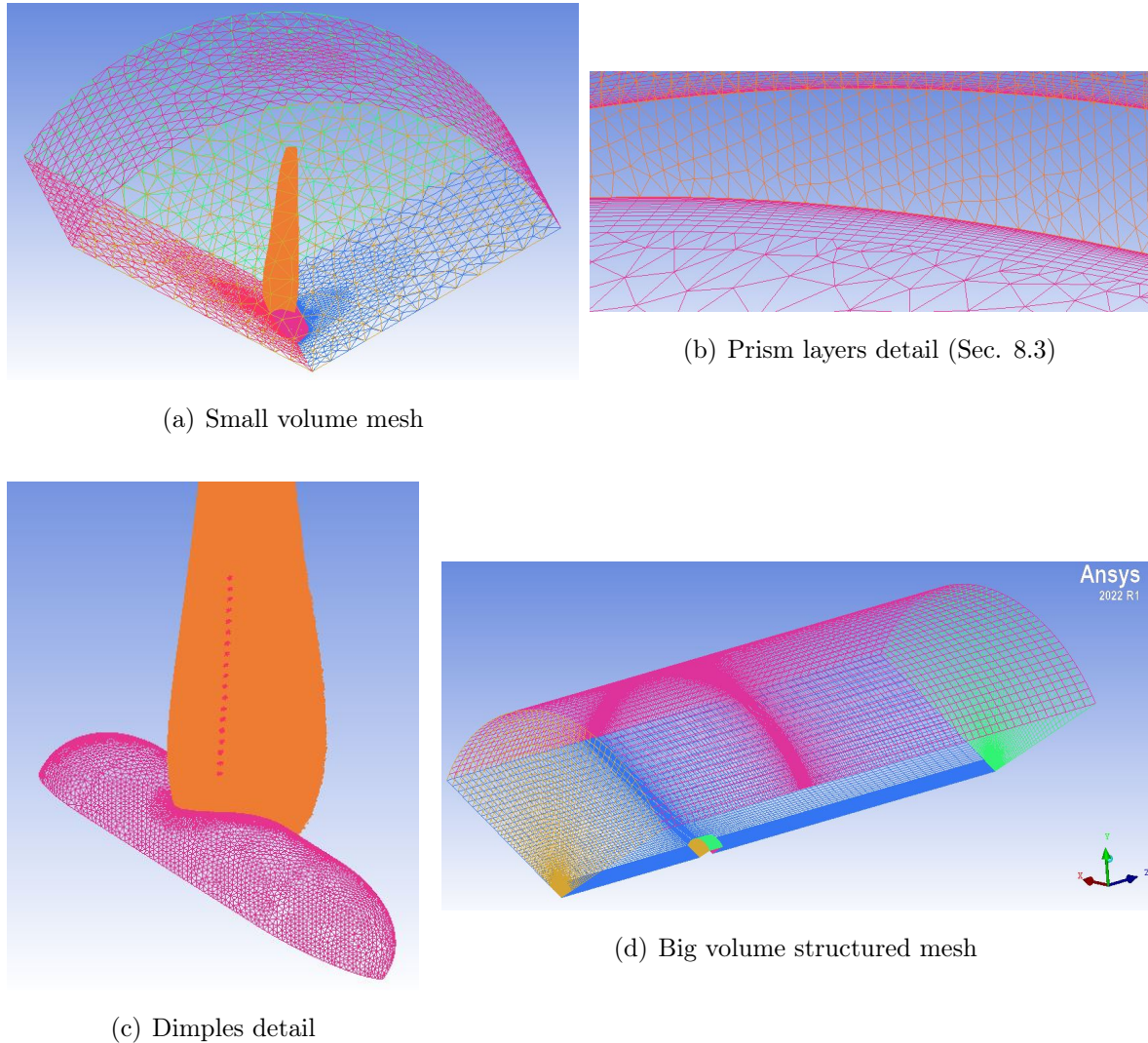


Figure 10.2: Control volume meshes

10.2 CFX setup

After the completion of the meshed volumes, they were imported into ANSYS CFX to establish various parameters and conduct the simulation. For this purpose, the **Analysis type** was configured as *Steady state*. The following are the key parameters utilized in this process:

- The inflow surface of the large volume (LV) has been modeled with **Inlet** surface,

with air velocity normal to the surface. The value of wind speed changes for each simulation;

- Outflow and top surfaces have been modeled with **Opening** surfaces, with option for mass and momentum corresponding to the *Entrainment* with a value of 1 *bar*, *pressure option* selected to *Opening pressure* and *Zero gradient* for what concerning the turbulence;
- Blade, hub and dimple surfaces have been modeled with **Wall** surfaces, considering *No slip wall* and *Smooth surface* options;
- Inclined surfaces have been "*virtually connected*" to create a virtual control volume made by 3 blades and a cylindrical control volume¹;
- The surfaces acting as interface between LV and SV, have been modeled considering a **Domain interface** interface between them;
- The LV fluid domain has been modeled considering *Air at 25°C, 1 bar* as pressure, *Non buoyancy* and *Stationary*;
- The SV fluid domain has been modeled considering *Air at 25°C, 1 bar* as pressure, *Non buoyancy* and *Rotating* with an angular velocity equal to 325 *rpm*;
- For what concern the **Fluid models**, the following assumptions have been made:
 - Heat transfer: None;
 - Turbulence: Shear Stress Transport - Gamma Theta Model²;
 - Combustion: None;
 - Thermal radiation: None;
- **Analysis type** has been set to **Steady state**;
- **Initialization** conditions have been set up in dedicated page; Cartesian components of velocity equal to what described before, static pressure equal to 1 *bar* and *medium intensity* for what concern the turbulence;
- The max number of iteration to reach the convergence has been set to 500.

The graphical vision of the CFX-setup is reported in Fig. 7.11

¹By virtually connect the two surfaces, it is possible to understand the behaviour of 3 blades HAWT simply modelling 1/3 of it; this is what previously mentioned in paragraph 7.1.6.

²This is the option for what concern the transitional turbulence.

Results

Baseline The baseline blade model has been tested at 4, 6, 8, 10, 11, 12, 13 and 14 m/s and the values of torque generated have been collected. Then the values of torque have been multiplied by the rotational speed to obtain the values of power generated by the wind turbine for each speed. Once the torque and power values have been available, torque and power coefficients could be estimated as:

$$C_T = \frac{Torque}{\frac{1}{2}\rho\pi D^3 v^2} \quad C_p = \frac{Power}{\frac{1}{2}\rho\pi D^2 v^3} \quad (10.1)$$

The values mentioned have been reported in Tab. 10.1:

SIMULATION RESULTS							
Rpm	Velocity	Torque	Power	λ	ω	C_T	C_p
[<i>rev/min</i>]	[<i>m/s</i>]	[<i>Nm</i>]	[<i>kW</i>]	[$-$]	[<i>rad/s</i>]	[$-$]	[$-$]
325	4	0.223	0.008	9.34	34.03	0.002	0.051
	6	6.040	0.206	6.24		0.022	0.409
	8	15.669	0.533	4.68		0.032	0.447
	10	28.750	0.979	3.74		0.037	0.420
	11	36.025	1.226	3.40		0.039	0.396
	12	41.750	1.421	3.12		0.038	0.353
	13	43.943	1.496	2.88		0.034	0.292
	14	44.160	1.503	2.67		0.0293	0.235

Table 10.1: Results of baseline blade simulations

The results are summarized in the following graphs:

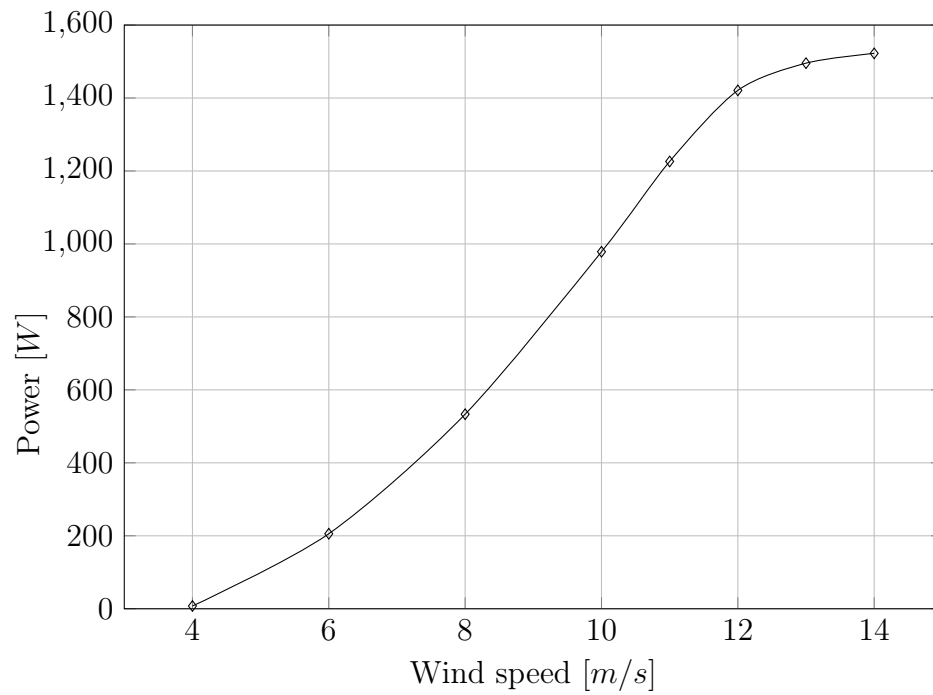


Figure 10.3: Power generated vs wind speed

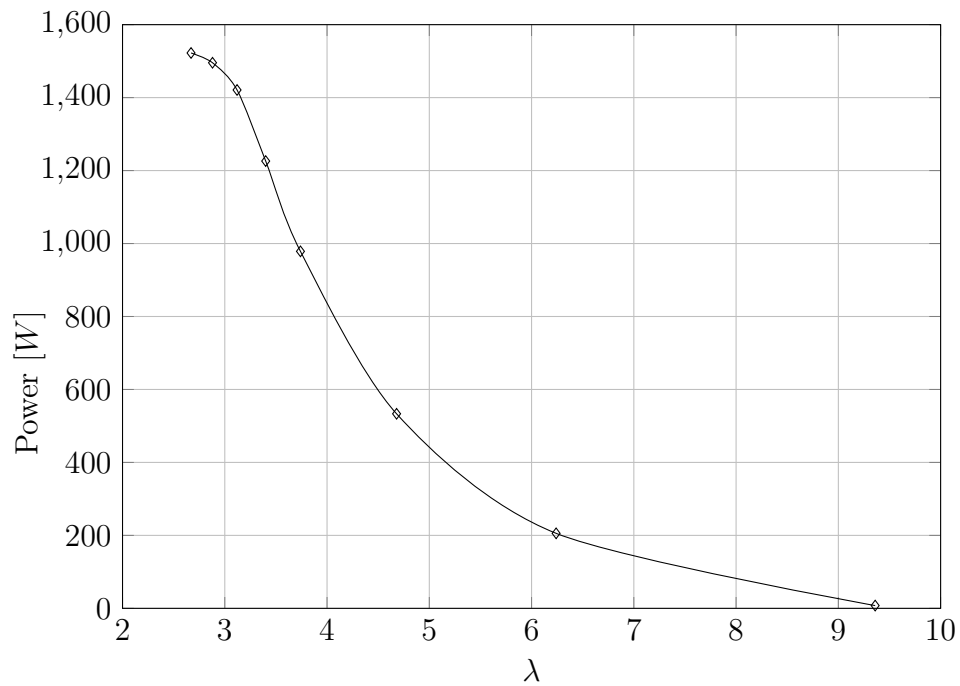


Figure 10.4: Power generated vs λ

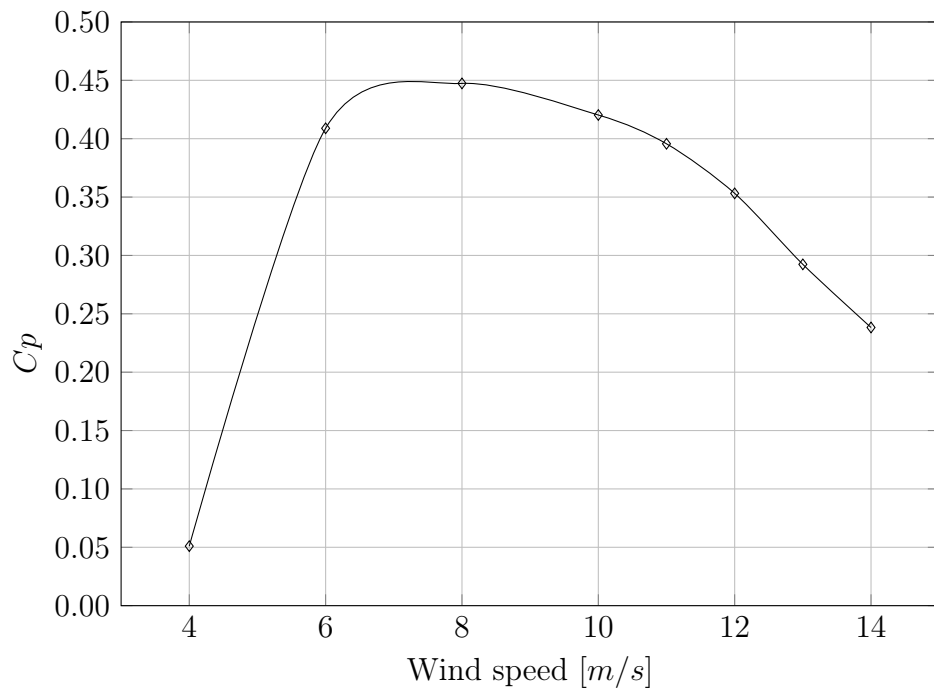
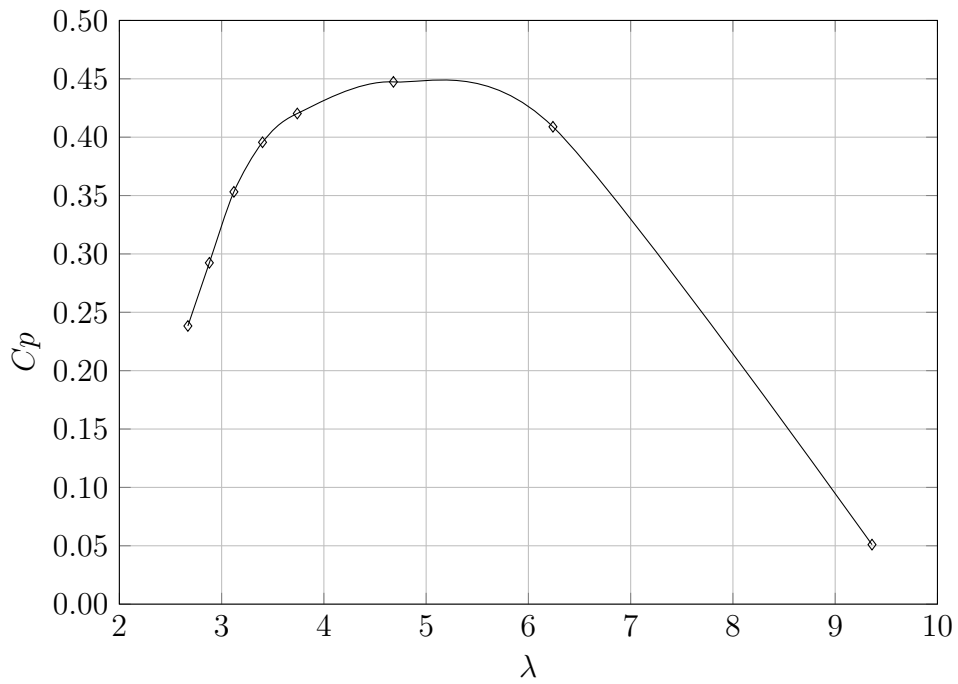


Figure 10.5: Power coefficient vs wind speed

Figure 10.6: Power coefficient vs λ

Dimpled The modified blade geometry has been tested at the same wind speeds of the baseline one, in particular 4, 6, 8, 10, 11, 12, 13 and 14 m/s and the values of torque generated have been collected. Then the values of torque have been multiplied by the rotational speed to obtain the values of power generated by the wind turbine for each speed.

The values mentioned have been reported in Tab. 10.2:

SIMULATION RESULTS							
Rpm	Velocity	Torque	Power	λ	ω	C_T	C_p
$[rev/min]$	$[m/s]$	$[Nm]$	$[kW]$	$[-]$	$[rad/s]$	$[-]$	$[-]$
325	4	0.314	0.011	9.34	34.03	0.003	0.072
	6	6.468	0.220	6.24		0.023	0.438
	8	16.435	0.559	4.68		0.033	0.469
	10	29.567	1.006	3.74		0.038	0.432
	11	37.221	1.267	3.40		0.040	0.409
	12	43.156	1.469	3.12		0.039	0.365
	13	45.963	1.564	2.88		0.035	0.306
	14	47.280	1.609	2.67		0.031	0.252

Table 10.2: Results of baseline blade simulations

The results are summarized in the following graphs:

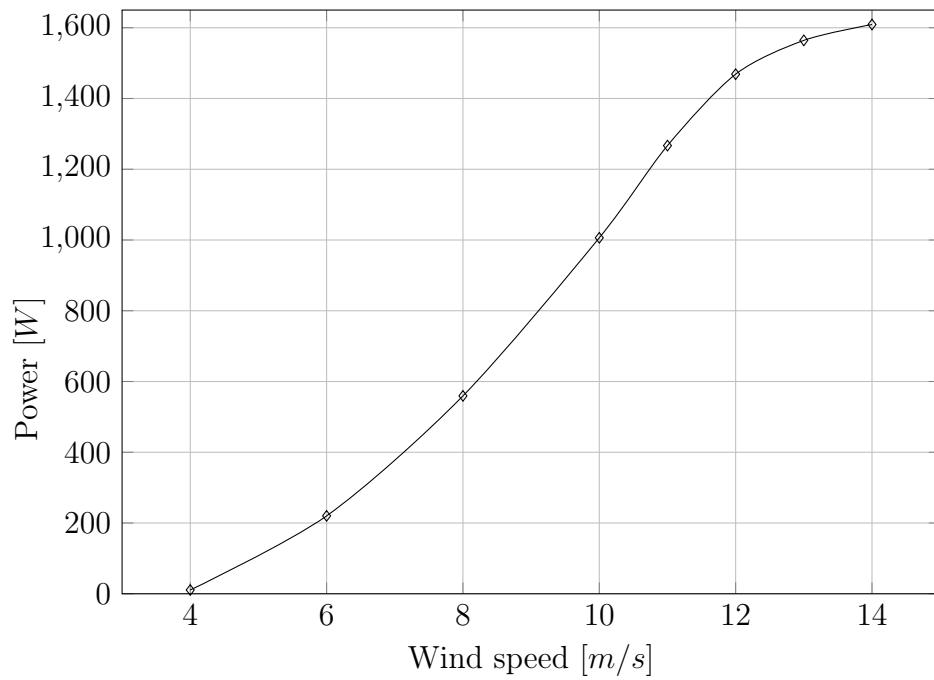


Figure 10.7: Power generated vs wind speed

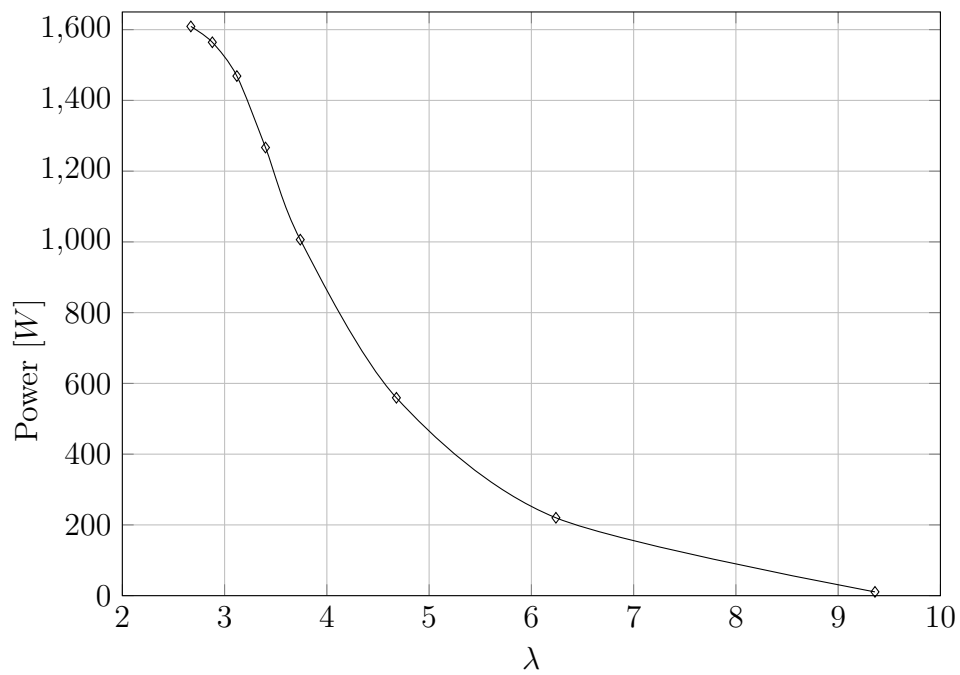


Figure 10.8: Power generated vs λ

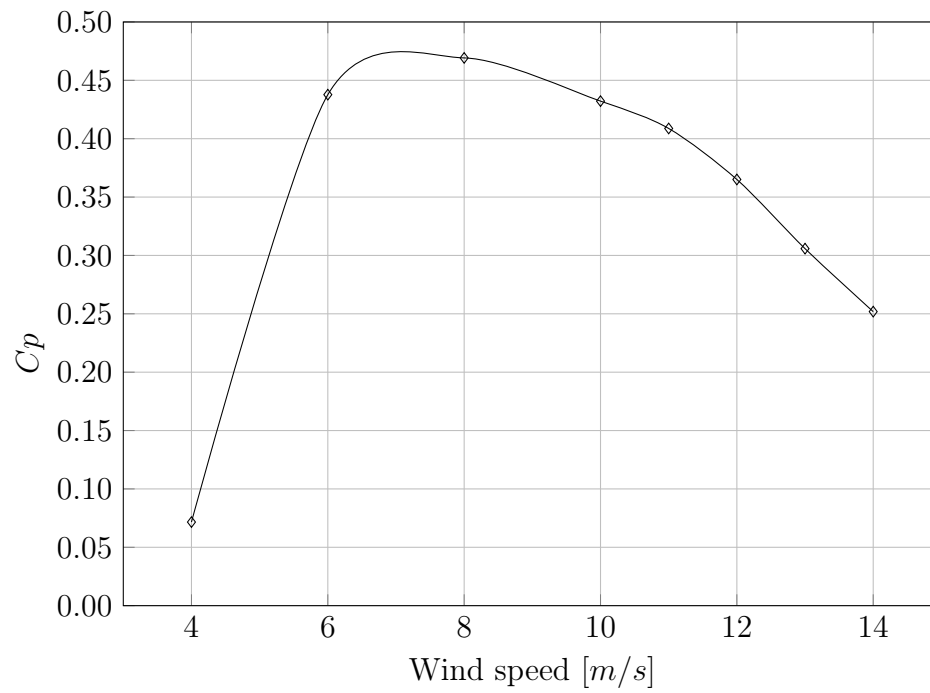
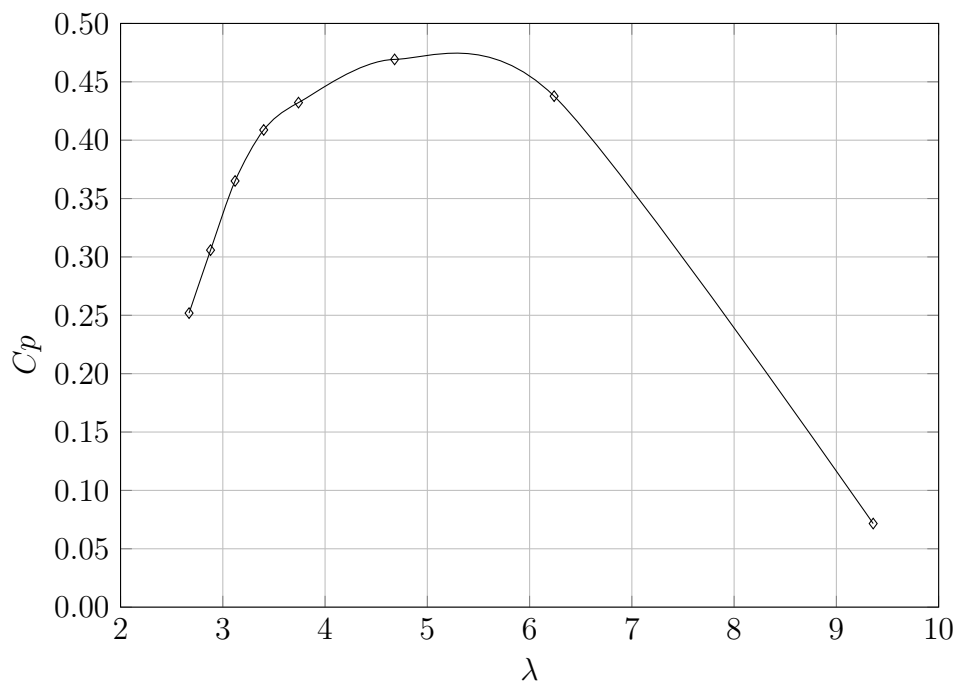


Figure 10.9: Power coefficient vs wind speed

Figure 10.10: Power coefficient vs λ

Results comparison

The torque, power, and relative torque and power coefficients for both the baseline and modified cases were collected and presented in tables (Tab. 10.3 and Tab. 10.4). These values were compared to each other and depicted in the graphs (Fig. 10.11 and Fig. 10.12).

Next, the energy captured by the wind turbine was calculated using the procedure described in Sec. 4.1. The calculated values were then listed in the table (Tab. 10.5). Lastly, the capacity factor values were determined following the procedure outlined in Sec. 4.1.1 and were reported in Tab. 10.6.

POWER COMPARISON					
Velocity	λ	$P_{baseline}$	$P_{dimpled}$	$C_{p_{baseline}}$	$C_{p_{dimpled}}$
[m/s]	[-]	[kW]	[kW]	[-]	[-]
4	9.36	0.008	0.011	0.051	0.072
6	6.24	0.206	0.220	0.409	0.438
8	4.68	0.533	0.559	0.447	0.469
10	3.74	0.979	1.006	0.420	0.432
11	3.40	1.226	1.267	0.396	0.409
12	3.12	1.421	1.469	0.353	0.365
13	2.88	1.496	1.564	0.292	0.306
14	2.67	1.503	1.609	0.235	0.252

Table 10.3: Power comparison

TORQUE COMPARISON					
Velocity	λ	$T_{baseline}$	$T_{dimpled}$	$C_{T_{baseline}}$	$C_{T_{dimpled}}$
[m/s]	[-]	[Nm]	[Nm]	[-]	[-]
4	9.36	0.223	0.314	0.002	0.003
6	6.24	6.042	6.468	0.022	0.023
8	4.68	15.669	16.435	0.032	0.033
10	3.74	28.753	29.567	0.037	0.038
11	3.40	36.025	37.221	0.039	0.040
12	3.12	41.750	43.156	0.038	0.039
13	2.88	43.943	45.963	0.034	0.035
14	2.67	44.164	47.280	0.029	0.031

Table 10.4: Torque comparison

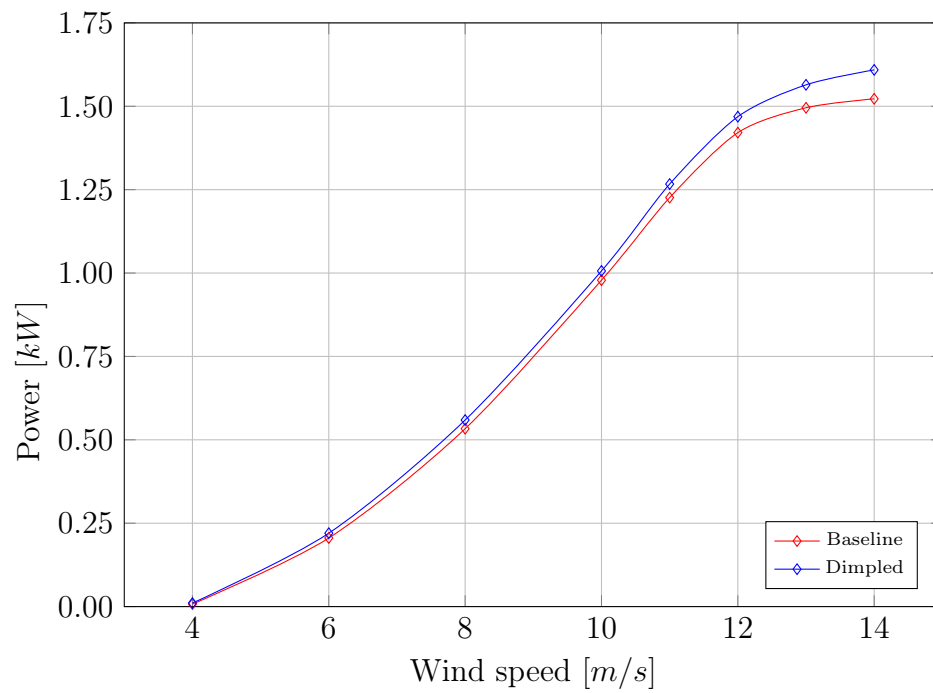


Figure 10.11: Power comparison vs wind speed

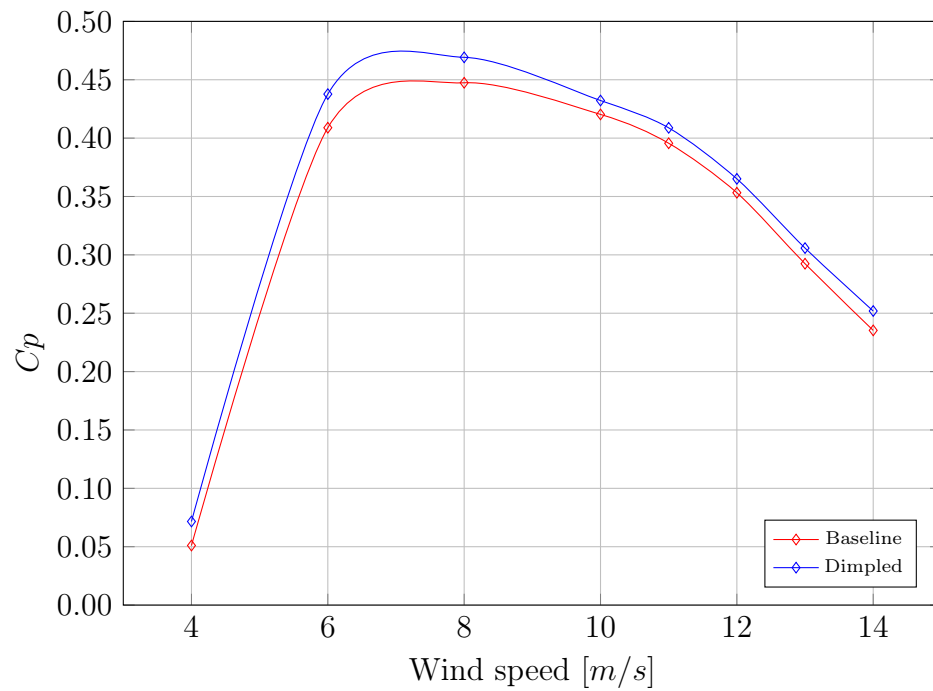


Figure 10.12: Power coefficient comparison vs wind speed

ENERGY COMPARISON										
Vel.	λ	Power			D	DP		Energy		
$\frac{m}{s}$	-	kW			$\frac{m}{s}$	$\frac{kW}{\frac{m}{s}}$		$\frac{kWh}{y}$		-
		Base	Dimp.	Dif		Base	Dimp.	Base	Dimp.	Dif
4	9.34	0.008	0.011	28.8%	0.118	0.001	0.001	2811	2939	4.36%
6	6.24	0.206	0.220	6.58%	0.099	0.020	0.022			
8	4.68	0.533	0.559	4.66%	0.070	0.037	0.039			
10	3.74	0.979	1.006	2.75%	0.043	0.042	0.044			
11	3.40	1.226	1.267	3.21%	0.033	0.040	0.042			
12	3.12	1.421	1.469	3.26%	0.024	0.034	0.035			
13	2.88	1.496	1.564	4.40%	0.017	0.026	0.027			
14	2.67	1.503	1.609	6.59%	0.012	0.018	0.020			

Table 10.5: Energy produced comparison

The two capacity factors relative to baseline and modified blades are reported in Tab. 10.6.

	Baseline	Dimpled
C_F	0.2139	0.2237
	1874 h/y	1959 h/y

Table 10.6: Capacity factor C_F

The CFD simulations confirmed the anticipated outcomes based on theoretical expectations. Specifically, by employing vortex generators to augment the energy within the boundary layer, the onset of stall conditions was delayed. Moreover, even when stall conditions did occur, the baseline blade profile was able to generate a higher torque and consequently more power.

With the implementation of dimple vortex generators, the stall angle has been pushed further compared to the nominal case and the power generated for wind velocities close to the cut-out one has increased significantly; moreover also the performance at smaller AoA increased a little bit due to the strength of the BL to deal with adverse pressure gradient. Even though the dimples position has been optimized for a wind speed in the range of 10 m/s, the benefits of them could be appreciable at higher wind speed also.

Through the implementation of dimpled blades, it becomes feasible to extract over

4% additional energy compared to the standard case, without necessitating any alterations to the blade geometry or the site itself. While the absolute gain may not appear substantial, it is crucial to consider the context of a micro wind turbine with a nominal power of 1.5 *kW*. This underscores the significance of adopting such an aerodynamic solution, as it has the potential to yield considerable energy benefits when applied across numerous scenarios, while still adhering to environmental and structural constraints.

It must be considered that the percentage increment isn't so relevant as could be with other blade geometries characterized by different airfoil section, because the S1210 is a airfoil that presents really good lift performance even in deep stall conditions; thus the torque generated when the AoA is slightly above the critical one for baseline configuration and slightly below the critical one for the dimpled geometry, are not really different because the power generated with the baseline blade configuration doesn't fall down abruptly.

3D model

In the Fig. 10.13 the 3D model of the HAWT has been reported. The tower and the basement have been only built to have a better comprehension of the global size of the WT but in the case of a real application they must be sized based on the ISO standards that define their structures; these components play a fundamental role in the structure of the WT and they must be designed considering safety first.

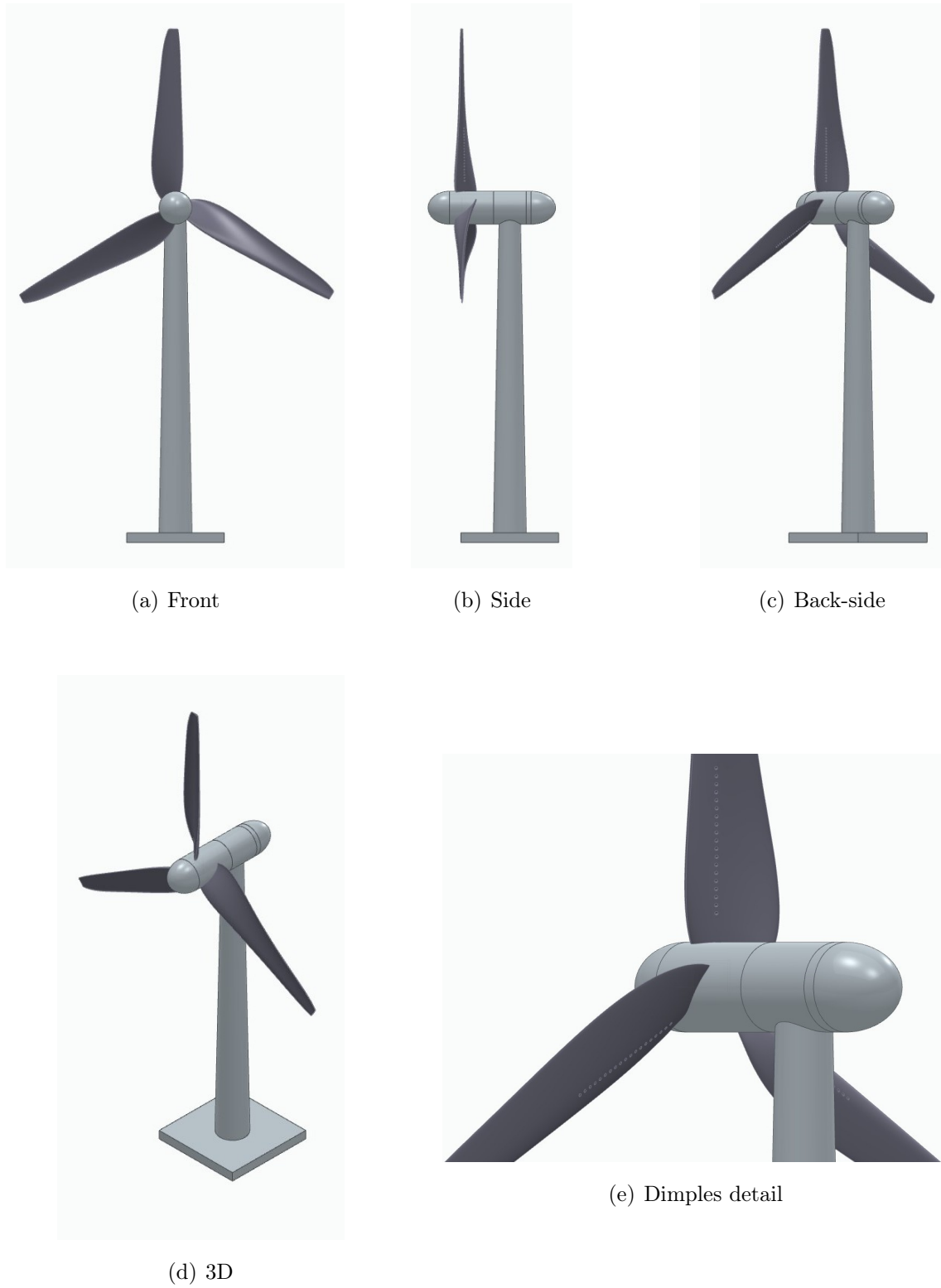


Figure 10.13: HAWT 3D model

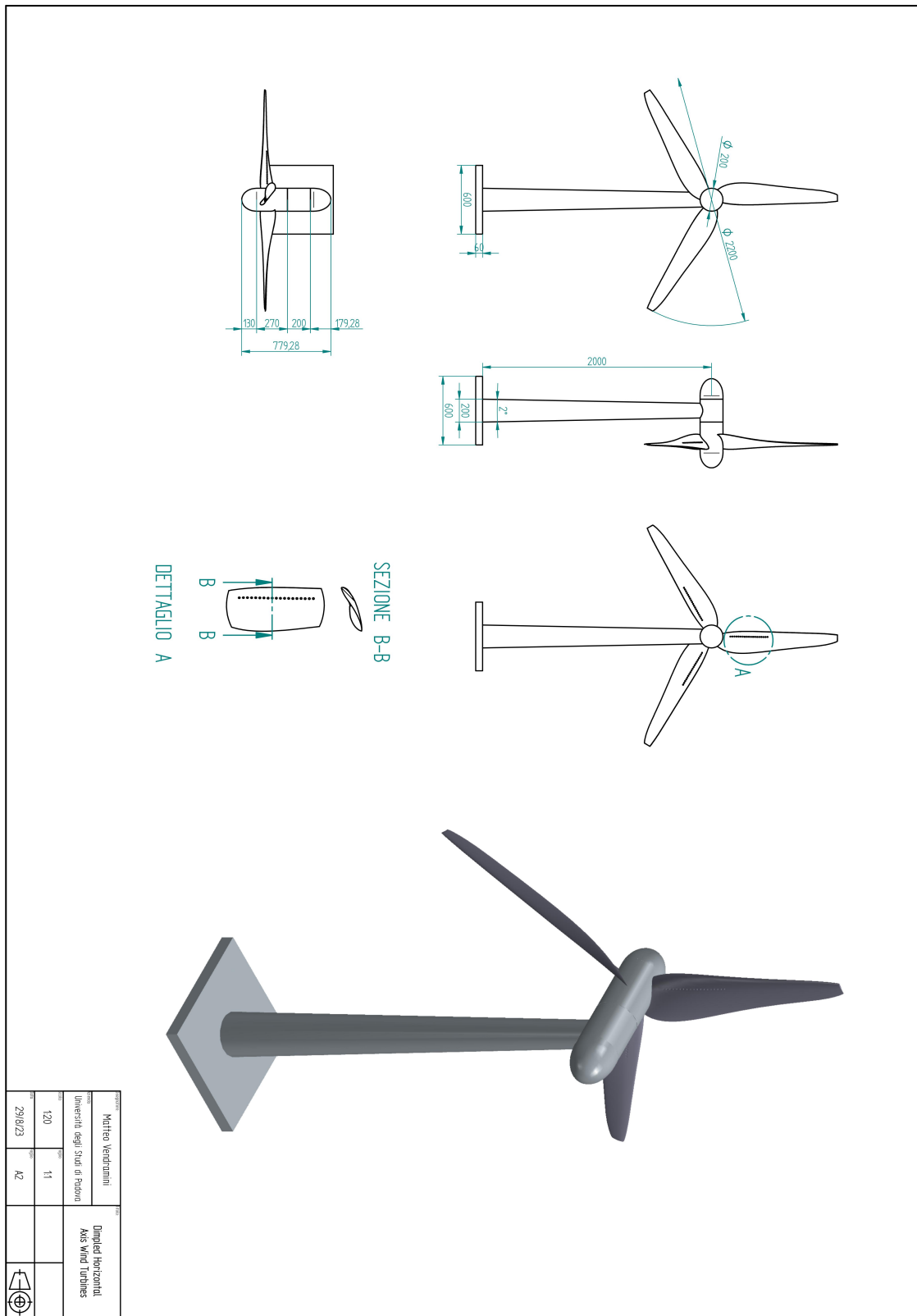


Figure 10.14: Technical drawing of the 3D model of HAWT

Conclusions

The objective of this study was to discover a novel approach for enhancing the efficiency and energy output of domestic wind turbines by addressing the challenge of boundary layer separation. This type of study is more important in the case of domestic installations, as the contribution in terms of relative power generation and extracted energy is higher compared to when referring to large-scale power plants. Previous real-world applications have employed methods like triangular vortex generators or turbulators. However, these methods overlook the three-dimensional rotational effect induced by the turbine rotation, leading to suboptimal vortex configurations.

To tackle this problem, the study proposed the implementation of axial-symmetric dimples. By incorporating these dimples, the issue associated with non-optimized vortex formations could be rectified.

Given that each wind turbine is equipped with a distinct airfoil configuration and has varying fundamental attributes such as rotational speed, tip and hub diameters, it becomes clear that a universal configuration for these dimples does not exist. Consequently, a specific and tailored analysis must be conducted for each individual case study.

The first crucial step in this analysis is to prioritize the selection of the installation site for the horizontal axis wind turbine. This choice is fundamental as it directly influences the determination of the baseline blade profile and other blade profile characteristics.

After establishing the initial configuration, the next step would involve optimizing the dimple geometry to determine the most effective design. Ideally, a comprehensive approach would involve creating various airfoil profiles with different dimple geometries and conducting wind tunnel tests to evaluate their performance in real-world applications. However, wind tunnel tests can be prohibitively expensive. As a result, preliminary investigations utilizing computational fluid dynamics (CFD) software have become the preferred solution in recent times.

While CFD simulations rely on calculations involving residual terms rather than

analytical solutions, the disparity between simulated behavior and real-world execution is minimal thanks to the advanced capabilities of modern CFD software and the computational power at our disposal. Although there may be slight discrepancies, the use of CFD allows for cost-effective exploration of different dimple geometries and provides valuable insights into their potential effectiveness.

This study involved conducting numerous Computational Fluid Dynamics (CFD) simulations to determine the optimal geometry and placement of dimples. To isolate the effects of the dimples, all other variables were held constant throughout the simulations. Initially, a few simulations did not converge due to suboptimal problem discretization during the preliminary stages. However, after addressing these errors, they reached the convergence of solution.

Once the best dimple geometry has been found, the creation of the dimpled blade geometry started, using a CAD software. Then, the baseline and the dimpled models have been tested under the same conditions to evaluate the differences between the two configurations.

The results obtained highlighted the validity of the study conducted, reflecting the expectations; the findings indicate that the optimal position occurs when the dimples are located at 30% of the chord length, spanning radially between 15% and 45%. The conducted simulations provide evidence that incorporating the dimpled design, in comparison to the nominal profile, results in a 4.36% increase in the energy generated. This translates to a rise from 2811 *kWh/y* to 2939 *kWh/y*, consequently elevating the capacity factor from 21.39% to 22.37%.

One of the limits of this study is in principle the fact that this configuration is valid only for this particular case and it's not extendible to all the possible solutions; moreover the economic aspects have not been considered here, while the additional costs and relative remuneration should be considered to verify the feasibility of the solution.

Some potential avenues for further research and development that align with the concept of this study want to be highlighted here, aiming to enhance the efficiency of domestic wind turbines.

One possible approach involves modifying the geometry of the leading edge by implementing a sinusoidal profile. This alteration would create controlled turbulence, prolonging the boundary layer attachment to the blade surface beyond what the standard blade configuration can achieve. Alternatively, another solution could involve

modifying the trailing edge with zig-zag or sinusoidal profiles to achieve similar outcomes.

Taking it a step further, a promising direction would be to combine these leading and trailing edge modifications with vortex generators, such as dimples or triangular VGs. The synergistic effect of these combined modifications could potentially yield more significant improvements compared to implementing a single solution in isolation.

Naturally, implementing these solutions would require time and resources, and reducing these requirements would be crucial to enhance the feasibility of these approaches. As these solutions become more widely adopted, advancements in technology and streamlined processes would likely lead to faster computational requirements and reduced implementation time.

Overall, exploring these possibilities and striving for increased efficiency in wind turbine technology necessitates ongoing research and development efforts to make these solutions more viable and practical.

Bibliography

- [1] Fluid Mechanics 101. *[CFD] Inflation Layers / Prism Layers in CFD*. Youtube. 2021. URL: <https://www.youtube.com/watch?v=1gSHN99I7L4>.
- [2] *Airfoil Tools*. Accessed on March 29, 2023. 2023. URL: <http://airfoiltools.com/airfoil/details?airfoil=s1210-il>.
- [3] *Altair AcuSolve*. Accessed on March 21, 2023. 2021. URL: https://2021.help.altair.com/2021/hwsolvers/acusolve/topics/acusolve/training_manual/turbulence_modeling_r.htm.
- [4] *Alxion*. Accessed on March 21, 2023. 2011. URL: <http://www.alxion.com/wp-content/uploads/2011/10/89.pdf>.
- [5] B. Baldwin and T. Barth. “A one-equation turbulence transport model for high Reynolds number wall-bounded flows”. In: *29th Aerospace Sciences Meeting*.
- [6] L. Battisti. *Gli Impianti Motori Eolici*. Città studi Edizioni, 2021, pp. 164–165.
- [7] A. Bjørk. *Coordinates and calculations for the FFA-W1-xxx, FFA-W2-xxx and FFA-W3-xxx series of airfoils for horizontal axis wind turbines*. Tech. rep. 1990.
- [8] Kim Bolth. *GRAS Sound and Vibration*. Accessed on March 21, 2023. 2022. URL: <https://www.grasacoustics.com/blog/aerodynamic-measurements-components-of-the-boundary-layer>.
- [9] Nor Azwadi Che Sidik et al. “A Short Review on RANS Turbulence Models”. In: *CFD Letters* 12 (Nov. 2020), pp. 83–96.
- [10] Olivier Cleynen. *Weather Guard Lightning Tech*. Accessed on March 21, 2023. 2020. URL: <https://weatherguardwind.com/wind-turbine-vortex-generator/>.
- [11] Valerio D’Alessandro et al. “Assessment of the dimples as passive boundary layer control technique for laminar airfoils operating at wind turbine blades root region typical Reynolds numbers”. In: *Energy* 170 (2019), pp. 102–111.
- [12] Kristian S Dahl and Peter Fuglsang. “Design of the wind turbine airfoil family RISØ-A-XX”. In: (1998).

- [13] Naveed Durrani. “Modelled and Resolved Turbulent Stresses around a circular cylinder using URANS, DES and DDES”. In: *CESAT, Islamabad, Pakistan* (2015).
- [14] Gedyon Fikadea et al. “Effects of dimples on aerodynamic performance of horizontal axis wind turbine blades”. In: *International Research Journal of Engineering and Technology (IRJET)* 7.1 (2020), pp. 525–529.
- [15] Peter Fuglsang and Christian Bak. “Status of the Risø wind turbine airfoils”. In: *2003 European Wind Energy Conference and Exhibition*. European Wind Energy Association (EWEA). 2003.
- [16] Gilles Godard and Michel Stanislas. “Control of a decelerating boundary layer. Part 1: Optimization of passive vortex generators”. In: *Aerospace Science and Technology* 10.3 (2006), pp. 181–191.
- [17] *Hardware upgrade*. Accessed on May 20th, 2023. URL: https://www.hwupgrade.it/news/scienza-tecnologia/eolico-turbine-ad-asse-verticale-piu-efficienti-quando-installate-le-une-vicino-alle-altre_97458.html.
- [18] *IdealSimulations*. Accessed on March 21, 2023. 2020. URL: <https://www.idealsimulations.com/resources/turbulence-models-in-cfd/>.
- [19] Ruifang Jiang et al. “Effect of vortex generator orientation on wind turbines considering the three-dimensional rotational effect”. In: *Ocean Engineering* 267 (2023), p. 113307. ISSN: 0029-8018.
- [20] Efe Kinaci. “Numerical and Experimental Investigation of The Rotor Blades of An HAWT With A Profile HKAS Inspired by a Maple Seed”. In: (Sept. 2015).
- [21] Vyshnavi Krishnamoorthy et al. “Numerical Analysis of Dimple Effect on Airfoils for varied AoA”. In: *International Research Journal on Advanced Science Hub 2* (2020), pp. 86–94.
- [22] Marinos Manolesos et al. “Using vortex generators for flow separation control on tidal turbine profiles and blades”. In: *Renewable Energy* 205 (2023), pp. 1025–1039.
- [23] Stan J Miley. *Catalog of low-Reynolds-number airfoil data for wind-turbine applications*. Tech. rep. Rockwell International Corp., Golden, CO (USA). Rocky Flats Plant; Texas A . . . , 1982.
- [24] Mostafa Momen. *Lecture 24, Part 1: Introduction to Computational Fluid Dynamics, DNS, LES, and RANS Techniques*. Youtube. 2021. URL: <https://www.youtube.com/watch?v=nE1NGk7UsPI>.

- [25] Arvind Mukundan. “Analysis of an Airfoil by Changing the Size, Shape and Location of the Dimple”. In: ().
- [26] Rubiat Mustak, Md Uddin, and Muhammad Mashud. “Effect of Different Shaped Dimples on Airfoils”. In: Mar. 2018.
- [27] *Nextville*. Accessed on May 20th, 2023. URL: https://www.nextville.it/Funzionamento_e_prestazioni/522/Il_generatore_eolico.
- [28] “Numerical study on the influence of vortex generators on wind turbine aerodynamic performance considering rotational effect”. In: *Renewable Energy* 186 (2022), pp. 730–741.
- [29] Safanah Raafat and Rajaa Hussein. “Power Maximization and Control of Variable-Speed Wind Turbine System Using Extremum Seeking”. In: *Journal of Power and Energy Engineering* 06 (Jan. 2018), pp. 51–69. DOI: 10.4236/jpee.2018.61005.
- [30] Ruud van Rooij and Nando Timmer. “Design of airfoils for wind turbine blades”. In: *Delft University of Technology, The Netherlands* 8 (2004).
- [31] Hamed Sedighi, Pooria Akbarzadeh, and Ali Salavatipour. “Aerodynamic performance enhancement of horizontal axis wind turbines by dimples on blades: Numerical investigation”. In: *Energy* 195 (2020), p. 117056.
- [32] P. Spalart and S. Allmaras. “A one-equation turbulence model for aerodynamic flows”. In: *30th Aerospace Sciences Meeting and Exhibit*.
- [33] Jenna Elizabeth Stolzman and Sanjivan Manoharan. “The Effectiveness of Dimples on a NACA Airfoil: A Numerical Investigation Conducted via an Independent Study”. In: *2021 ASEE Virtual Annual Conference Content Access*. 2021.
- [34] M. Suresh and N. Sitaram. “Gurney flap applications for aerodynamic flow control”. In: 2011.
- [35] J.L. Tanger and D.M. Somers. *Advanced airfoils for HAWTs*. Tech. rep. 1985.
- [36] J.L. Tanger and D.M. Somers. *Status of the Special Purpose Airfoil Families SERI/TP-217-3264*. Tech. rep. 1987.
- [37] Jonna Tiainen et al. “Flow Control Methods and Their Applicability in Low-Reynolds-Number Centrifugal Compressors—A Review”. In: *International Journal of Turbomachinery, Propulsion and Power* 3 (Dec. 2017), p. 2.
- [38] *Wikipedia*. Accessed on March 28, 2023. 2022. URL: https://en.wikipedia.org/wiki/Detached_eddy_simulation.
- [39] David C Wilcox et al. *Turbulence modeling for CFD*. Vol. 2. DCW industries La Canada, CA, 1998.

- [40] Zhenzhou Zhao et al. “Researches on vortex generators applied to wind turbines: A review”. In: *Ocean Engineering* 253 (2022), p. 111266.
- [41] CY Zhu, MF Li, and Y Liu. “Aerodynamic modelling of wind turbines concerning rotational augmentation and dynamic stall”. In: *Proceedings of the CSEE*. 2021, pp. 1–12.

